Study of the Charge-Transfer Dynamics at the Interface of Two-Dimensional Materials

Dissertation

zur Erlangung des Doktorgrades der Naturwissenschaften (Dr. rer. nat.)

dem

Fachbereich Physik

der Philipps-Universität Marburg
vorgelegt von

Master of Science

Jonas E. Zimmermann

aus Peine

Universitätsstadt Marburg, 2021

FÜR

MEINE FAMILIE

Zusammenfassung

Im Rahmen dieser Arbeit wurde die Ladungsträgerdynamik und insbesondere der Landungstransfer an Grenzflächen zweidimensionaler Übergangsmetall-Dichalkogeniden untersucht. Um dieses Ziel zu erreichen, wurde ein optimierter experimenteller Aufbau entwickelt, der funktional in erster Linie ein Mikroskop ist, aber zugleich die Analyse eines frequenzverdoppelten Signals einer nur μm-großen Probe erlaubt. Hierdurch erlangen wir Zugriff auf die Kristallorientierung der Proben, und können zudem zeitaufgelöste Messungen mit einer Zeitauflösung von bis zu $10\,\text{fs}$ durchführen. Nach dem Entwurf und dem Aufbau des Experiments wurde dieses zunächst verwendet, um die Lebensdauer von Exzitonen in Mono- und Multilagen von MoS_2 zu untersuchen.

Die Ergebnisse für die Lebensdauer der pumpinduzierten Signale bei diesem "proof-of-principle"-Experiment zeigten für die Monolagen $\tau_1 = 1{,}9 \pm 0{,}7\,\text{ps}$ und $\tau_2 = 48{,}5 \pm 2{,}1\,\text{ps}$ sowie $\tau_1 = 3{,}2 \pm 0{,}9\,\text{ps}$ für die Multilagen - in guter Übereinstimmung mit Werten aus der Literatur. Des Weiteren konnte gefolgert werden, dass der pumpinduzierte Abfall der nichtlinearen Suszeptibilität mit der Erzeugung von Exzitonen im Zusammenhang steht, wodurch sich deren Lebensdauer direkt vermessen lässt.

Nachdem so die Viabilität des Experiments für die weitere Untersuchung der Ladungsträgerdynamik in Heterostrukturen bestätigt wurde, haben wir unseren Fokus auf die Studie einer $MoSe_2$/WSe_2-Heterostruktur-Probe gesetzt. Die Heterostruktur wurde unter einem Fehlwinkel von 32,3° präpariert. Dabei nutzten wir aus, dass sich die Signale der einzelnen Monolagen in der Heterostruktur mit unserem Aufbau selektiv und zeitaufgelöst vermessen lassen. Dies wird ermöglicht durch polarisationsaufgelöste Messungen, bei denen man das Signal einer Monolage durch Feineinstellung der Polarisation des Sondierungsimpules unterdrückt, während die andere Monolage vermessen wird. Dieses Alleinstellungsmerkmal des Aufbaus in Kombination mit energieabhängigen Messungen enthüllte einen zuvor noch unbekannten bidirektionalen Ladungstransfer zwischen den Monolagen. Auf die resonante Anregung einer Monolage folgt verzögert eine Verringerung des generierten frequenzverdoppelten Signals, die nur zu verzeichnen ist, während der Sondierungsstrahl sensitiv auf die andere Monolage ist. Das verzögert generierte Signal ist dagegen nicht sichtbar, wenn das Experiment auf die direkt angeregte Schicht eingestellt wird. Dieses Verhalten bekräftigt zusammen mit dem verzögerten Charakter des Abfalls die Interpretation der Ergebnisse als Ladungstransfer-Prozesses zwischen den Lagen, bei dem Interlayer-

Exzitonen gebildet werden. Die bei dem so identifizierten Lochtransfer gefundenen Transferzeiten betragen $\tau_{\text{MoSe}_2 \to \text{WSe}_2} = 210 \pm 60\,\text{fs}$ vom MoSe_2 ins WSe_2 nach Anregung mit 1,80 eV sowie $\tau_{\text{WSe}_2 \to \text{MoSe}_2} = 610 \pm 150\,\text{fs}$ nach Anregung mit 2,09 eV.

Der nächste Schritt auf dem Weg zum tieferen Verständnis des Ladungstransfer-Prozesses bestand in systematische Messungen an Proben zusammengesetzt aus MoS_2- und WSe_2-Monolagen unter verschiedenen Stapelwinkeln. Durch Anwendung der durch die vorangegangenen Studien gewonnen Erkenntnisse gelang es, einen Elektronentransfer aus dem WSe_2 ins MoS_2 zu identifizieren, nachdem das WSe_2 selektiv angeregt wurde. Insgesamt wurden drei Stapelwinkel untersucht, wobei eindeutige Unterschiede aufgedeckt werden konnten. Die gefundenen Transferzeiten variieren hierbei stark für die unterschiedlichen Stapelwinkel zwischen $12 \pm 4\,\text{fs}$ und $85 \pm 9\,\text{fs}$. Diese klare Diskrepanz zwischen den Proben wurde einem erhöhten räumlichen Überlapp der Wellenfunktionen zwischen Zuständen in der Grenzflächenebene zugeschrieben. Des Weiteren konnte die zentrale Rolle von hybridisierten Zuständen bei der Rekombination der angeregten Exzitonen gezeigt werden. Hierfür wurde die Pumpenergie auf 1,85 eV erhöht. Die gesteigerte Anregungsenergie öffnet zuvor nicht aktive Rekombinationskanäle über Zustände am Γ-Punkt, wodurch sich die Lebensdauer in allen Proben auf $\approx 200\,\text{ps}$ angleicht.

Schlussendlich wurden noch Sondierungsmessungen an Proben von chiralen Metall-Halogenide durchgeführt. Die Ergebnisse festigen das Interesse an dieser einzigartigen Materialklasse und scheinen vielversprechend für zukünftige Anwendungen in komplexeren Van der Waals (VdW) Heterostrukturen.

Abstract

In this thesis the charge-transfer dynamics in two-dimensional transition metal dichalcogenide (TMD) heterostructures (HS) were studied. In order to enable efficient study of TMD heterostructures a re-imagined experimental technique was employed: optical second-harmonic (SH) imaging microscopy. The newly developed setup allows for the study of μm small samples, giving access to the crystal orientation as well as enabling time-resolved measurements with a time-resolution of about 10 fs. After designing und building the experiment it was deployed to measure and determine the lifetimes of excitons in mono- and multilayers of MoS_2. This proof-of-principle experiment found lifetimes for the monolayer of $\tau_1 = 1.9 \pm 0.7$ ps and $\tau_2 = 48.5 \pm 2.1$ ps as well as $\tau_1 = 3.2 \pm 0.9$ ps for the multilayer, well in accordance with current literature. Furthermore it allowed for association of the pump-induced decrease in the nonlinear susceptibility with the generation of intralayer excitons, giving direct access to their lifetimes.

After validation of the viability of the experiment for the further study of heterostructure charge-carrier dynamics we used the setup to measure a $MoSe_2/WSe_2$ heterostructure, which was misaligned under a stacking angle of 32.3°. We discovered that it was possible to measure selectively the time-resolved changes of the individual monolayers inside the heterostructure via probe polarization dependent measurements. This was achieved by carefully tuning the probe polarization to suppress either of the monolayers and extract the lifetime from other. This unique characteristic of the setup in tandem with energy dependent measurements revealed a bi-directional charge transfer. Following the resonant excitation of one layer a delayed decrease in the optical second-harmonic signal becomes visible when sensitive to the other layer of the heterostructure. This delayed filling is absent when the probe polarization is tuned to the pumped material further corroborating the identification as a charge-transfer process in which interlayer excitons are formed. The hole transfer times found were $\tau_{MoSe_2 \rightarrow WSe_2} = 210 \pm 60$ fs from $MoSe_2$ into WSe_2 following excitation at 1.80 eV, as well as $\tau_{WSe_2 \rightarrow MoSe_2} = 610 \pm 150$ fs following excitation at 2.09 eV.

The next step to deepen our understanding of the charge-transfer was a systematic study of samples consisting of MoS_2 and WSe_2 with different stacking angles. By applying the insight gained from the previous study we identified an electron transfer from WSe_2 into MoS_2 after selectively exciting the WSe_2. Overall three stacking configuration were measured and clear differences were identified. The transfer times

were found to vary significantly for different stacking angles in a range from $12 \pm 4\,\mathrm{fs}$ up to $85 \pm 9\,\mathrm{fs}$. These disparities were accredited to an enhanced spatial wavefunction overlap between states in the interfacial plane. Furthermore, the importance of hybridized states for the charge-recombination dynamics was illustrated. Therefore the pump-photon energy was tuned to $1.85\,\mathrm{eV}$. The larger excitation energy opened previously non-active radiative recombination channels via states around the Γ-point, which led to an equalization of the decay times for all samples to $\approx 200\,\mathrm{ps}$.

Lastly in an exploratory study the aptitude of a new material class in the form of chiral metal halides for application in more complex heterostructures was investigated. The results consolidated the interest in the material showing promise for future applications in more complex Van der Waals coupled heterostructures.

List of Publications

This cumulative dissertation is based on the **articles I** through **IV**. **Article III** has been accepted for publication in ACS Nano. The personal contribution of the author is stated in the following.

I **Second-Harmonic Imaging Microscopy for Time-Resolved Investigations of Transition Metal Dichalcogenides**
J.E. Zimmermann, B. Li, J.C. Hone, U. Höfer, and G. Mette;
Journal of Physics: Condensed Matter **32**, 485901 (2020).
In **article I** the newly developed method of time-resolved optical second-harmonic imaging microscopy is introduced by presenting exemplary data for mono- and multilayers of CVD grown MoS_2. GM and UH conceived the study. JEZ designed and built the setup as well as executed the experiments and deciphered the results with help of GM and UH. The samples were prepared by BL and JCH. JEZ prepared the figures for the manuscript. The manuscript was written by GM.

II **Directional Ultrafast Charge Transfer in a WSe_2/$MoSe_2$ Heterostructure Selectively Probed by Time-Resolved SHG Imaging Microscopy**
J.E. Zimmermann, Y.D. Kim, J.C. Hone, U. Höfer, and G. Mette;
Nanoscale Horizons **5**, 1603 (2020).
In **article II** a $MoSe_2$/WSe_2 heterostructure sample with a misaligned stacking angle is studied. Because of the unique strengths of our setup it was possible to extract the charge-transfer times after the individual resonant excitation of each of the materials. This allowed the identification of a bi-directional charge-transfer. GM conceived the study. JEZ executed the experiments and anlayzed the data together with GM and UH. JEZ devised the first version of the manuscript, which was then revised by GM with contributions of all co-authors. The samples were prepared by YDK and JCH.

III Ultrafast Charge-Transfer Dynamics in Twisted MoS_2/WSe_2 Heterostructures

J.E. Zimmermann, M. Axt, F. Mooshammer, P. Nagler, C. Schüller, T. Korn, U. Höfer, and G. Mette;

In **article III** the charge-carrier dynamics in dependence of the heterostructure stacking angle are systematically investigated. Pump-photon energy dependent measurements revealed clear differences in the electron transfer times. It was shown that the stacking influences the transfer time as well as the recombination rate of generated interlayer excitons. GM conceived the study. MA built the setup for the experiments. JEZ performed the experiments and interpreted the results with GM and UH. The sample preparation and characterisation was done by FM, PN, CS und TK. JEZ devised the first version of the manuscript, which was revised by GM with contributions of all co-authors.

IV Band Gap-Tunable, Chiral Hybrid Metal Halides Displaying Second-Harmonic Generation

N. Dehnhardt, M. Axt, J.E. Zimmermann, M. Yang, G. Mette and J. Heine;

In **article IV** the new material class of chiral hybrid metal halides, as a candidate for new two dimensional structures, was introduced. Different base material combinations were characterized by UV-vis absorption spectroscopy, X-ray crystallography as well as SHG. JH and GM conceived the study. JEZ did exploratory SHG measurements on the individual materials to determine material stability and wrote the programmes used for the simulation of the SH rotational anisotropy measurements. MA performed the SH anisotropy and fluence dependent measurements and interpreted the results together with JEZ and GM. ND and MY synthesized the materials and characterised them. Furthermore they measured the UV-Vis spectra and performed and evaluated X-ray crystallography measurements. The manuscript development was split. ND, MY and JH wrote the discussion for synthesis, crystal structures and basic chemical analysis while MA and GM wrote the second-harmonic section.

Further publications by the author which do not contribute to this work:

A. Lerch, J.E. Zimmermann, A. Namgalies, K. Stallberg and U. Höfer;
Two-photon photoemission spectroscopy of unoccupied electronic states
at CuPc/PTCDA/Ag(1 1 1) interfaces
J. Phys.: Condens. Matter **30**, 494001 (2018).

G. Mette, J.E. Zimmermann, A. Lerch, K. Brixius, J. Güdde, A. Beyer, M. Dürr,
K. Volz, W. Stolz, and U. Höfer;
Femtosecond time-resolved nonlinear optical spectroscopy of charge transfer at
the buried GaP/Si(001) interface
Appl. Phys. Lett. **117**, 081602 (2020).

Contents

Chapter 1

Introduction

Miniaturisation is one of the key aspects in modern technologies. Ever since the development of the microprocessor in 1971 [1] in the form of the Intel 4004 chip, the size of the processors has been shrinking further and further, with the smallest sizes going down to 2 nm in May of 2021 [2]. It is therefore self-explanatory that, while the volume to surface ratio shifts in favor of the surface more and more, the importance of interfaces increases manifold for the development of new technologies. This underlines the necessity and relevance of a detailed understanding of the interface in and by itself, which is why the interest in exploration of interface phenomena on a fundamental level has increased steadily over the years [3].

One of the central aspects for semiconductor based devices are charge-transfer processes between different materials. The efficiency of the charge-transfer heavily influences the performance for all sorts of devices, *e.g.* photovoltaics [4] or transistors [5] to name but a few. Therefore it is of utmost importance to understand the subsequent procedures following photoexcitation of charge-carriers in semiconductor heterointerfaces on a fundamental level. In order to study the underlying mechanisms, an experimental technique which is able to access the ultrashort time regimes on which these processes occur is mandatory. Furthermore, sensitivity to the interface is of course indispensable. Due to the necessity of broken inversion symmetry to efficiently generate a second-harmonic (SH) signal, optical second-harmonic generation (SHG) is inherently surface and interface sensitive in inversion symmetric materials [6–8]. As a result of the implicit symmetry sensitivity of SHG ,the structure of samples can be studied via anisotropy measurements. If applied in a pump-probe scheme, time-resolved second-harmonic measurements can give access to minuscule changes of the second-order nonlinear susceptibility which can be directly associated with charge-carrier processes in the measured samples. Therefore, SHG is naturally the perfect tool for the study of charge-transfer dynamics at buried interfaces.

Ever since the first successful preparation of graphene [9], the research interest in ultra-thin nanosheets and their fascinating properties has surged drastically. This interest was increased even further through the discovery of surprising properties in two-dimensional transition metal dichalcogenides (TMDC). When thinned down to a single monolayer, a direct bandgap at the K-point (of TMDCs) is formed [10, 11].

While this process in itself already offers a plethora of research opportunities, TMDCs come with a larger variety of compelling attributes. Due to the broken inversion symmetry (leading to a considerable SH signal [12, 13]), the energetically degenerate K and K' valleys at the edge of the hexagonal Brillouin zone offer unique possibilities for the study of the valley degree of freedom. This is caused by the strong spin-orbit coupling of the metal d-bands [14] in TMDCs leading to a spin-split valence band, with the separation on a magnitude of several hundred meV [15].

So while the monolayers of TMDC materials alone are already highly interesting research subjects, adding different material combinations to form heterostructures (HS) expands their inherent capabilities and enables further intriguing research opportunities. Following optical excitation, strongly bound intralayer excitons [16] in the individual layers of the heterostructure are formed. Since most TMDC combinations form type-II heterostructures [17], charge-separation occurs due to the type-II band alignment and so called interlayer excitons are established [18–29]. While there have been studies concerning the charge-transfer, where it was shown that the charge-transfer occurs on an ultrafast timescale (fs), the mechanisms involved in the process and the influences on its dynamics remain enigmatic due to insufficient time-resolution of the applied experimental schemes [27, 29–33]. Therefore it is the main goal of this work to further elucidate the charge-carrier dynamics in TMDC heterostructures by contributing systematic measurements performed with the newly developed optical second-harmonic imaging microscopy technique. An experimental setup in the form of a microscope is imperative, since to this day the largest prepared TMDC samples still only range on a size-scale of $(100\,\mu\mathrm{m})^2$.

The presented thesis approaches the study of charge-transfer dynamics in TMDC heterostructures in three steps:

In **article I** the setup utilized in all further research is introduced and its capabilities are presented in form of a proof-of-principle experiment performed on MoS_2 mono- and multilayers.

Article II presents the first successful measurements with our experiment on a misaligned $MoSe_2/WSe_2$ heterostructure. We were able to identify a bi-directional hole-transfer on a femtosecond timescale between the layers following resonant B-exciton generation. This enhanced the overall understanding of the charge-transfer dynamics.

In **article III** we were finally able to employ our technique to systematically study several heterostructures with regard to the influence of the stacking configuration on the charge-carrier dynamics. Systematic pump energy and polarization resolved measurements reveal stark contrasts between the measured stacking configurations for the charge-transfer. Furthermore, it was shown that hybridized states around the Γ-point play a central role for charge-carrier recombination.

And lastly in **article IV** we explored a new material class of chiral hybrid metal halides as a candidate for the vast family of two-dimensional VdW coupled materials.

Chapter 2

Fundamentals

This work is about charge-transfer processes in TMDC heterostructures. In order to enable a fundamental understanding of these charge-carrier dynamics, knowledge about the TMDC building blocks is mandatory. Therefore, the characteristics and the unique features of TMDCs are introduced in the following sections. Furthermore, the band alignment and the spin structure of TMDC heterostructures, which play a central role in the charge-transfer are established.

After that, the fundamentals of the central experimental technique for this work, time-resolved second-harmonic generation in TMDC materials, is shown.

And finally, the experimental setup for second-harmonic imaging microscopy is showcased.

2.1 Transition Metal Dichalcogenides

The central research focus of this dissertation lies on the study of charge-transfer dynamics at interfaces. Here the basic building blocks of the studied interfaces and their characteristics are introduced. In the first part, I focus on TMDC monolayers, and why there has been a surge in studies concerning these materials in the last decade. This general introduction will be followed by an exemplary demonstration of characteristics for TMDC heterostructures consisting of different material combinations.

Monolayers

As the name of the material already indicates, TMDCs consist of transition metal (Mo, W) and chalcogen (S, Se) atoms. In nature they form Van der Waals coupled layered crystals, in a trigonal prismatic crystal structure [34]. While MoS_2 has been in use since the 1970s as a dry lubricant [35], it became the center of attention after the discovery of a direct bandgap forming between the K-points of the Brillouin zone when thinning the material down to a single monolayer [10, 11]. This discovery sparked enormous interest in the study of TMDC materials, since the direct bandgap centered in the visible region makes them attractive candidates for a plethora of
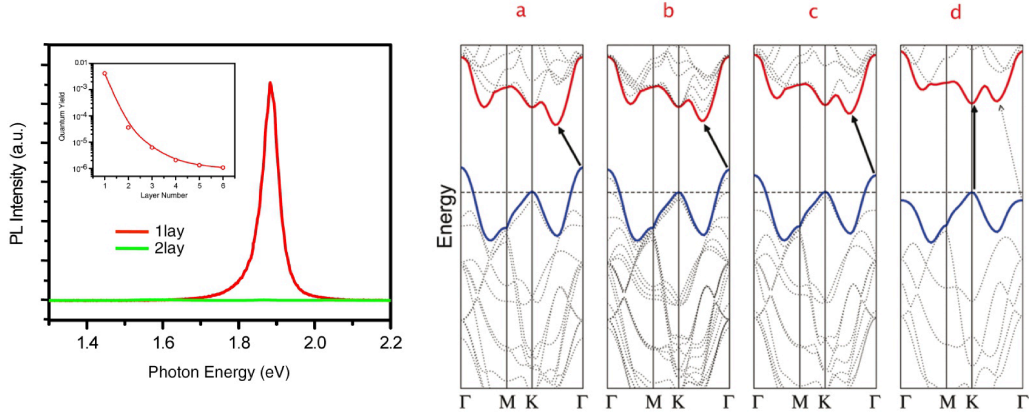
Fig. 2.1: Left: A photoluminescence (PL) measurement comparing a monolayer of MoS_2 (red) with a bi-layer (green) from reference [10]. The dramatic increase of PL intensity indicates the formation of a direct bandgap. **Right:** Bandstructure calculations for decreasing layer thicknesses from left to right (a: bulk, b: quadrilayer, c: bi-layer and d: monolayer) from reference [11]. The downwards (upwards) shift of the bands around the $\Gamma(\Sigma)$-point facilitates the formation of the direct bandgap for the monolayer.
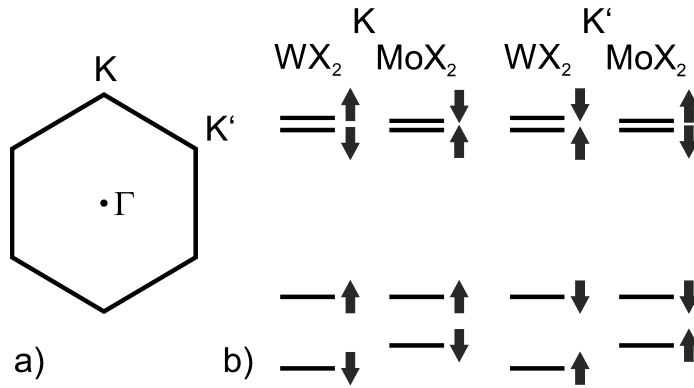

Fig. 2.2: Schematic sketch to illustrate the spin characteristics of TMDC monolayers. a) Brillouin zone of a TMDC material . b) Spin-structure and energy scheme for the K-points in W- and Mo- based TMDC monolayers.

applications [36], for example in photovoltaics [37], field-effect transistors [5, 38] or super-capacitors [39].

Another central aspect further heightening the interest in TMDC materials is due to the broken inversion symmetry in the monolayer, which leads to an inequality of the K-points of the Brillouin zone. Together with the strong spin-orbit coupling present in these materials, due to the transition metals, the valence band as well as the conduction band are spin-split. While the spin splitting for the conduction band is minor in the range of tens of meV, the splitting for the valence band is substantially larger with a maximum splitting of 466 meV for WSe_2 [15]. The spin-structure of the conduction band in Mo based TMDCs is mirrored in comparison to W based TMDCs (see Fig. 2.2). This in turn determines selections rules for potential optical excitation
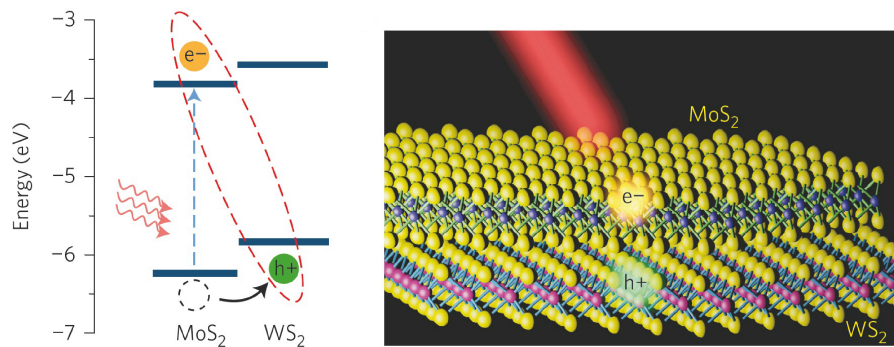
Fig. 2.3: Left: Sketch illustrating the band alignment of a MoS_2/WS_2 heterostructure as well as showing the occuring hole-transfer. **Right:** Ball and stick model of the HS emphasizing the spatial separation of electron and hole subsequent to optical generation of an intralayer exciton. Figure from reference [29].

[40, 41] and recombination. Consequently, the energetically most favoured exciton configuration in W based TMDCs is optically dark since the radiative recombination is spin forbidden [42, 43].

Heterostructures

While TMDC monolayers already have their own allure, the central reach for attractive research become apparent for stacked HS consisting of different TMDC materials. Research possibilities (Moiré excitons [44, 45], diffusion of excitons [46], interlayer hybridization [47] etc.) concerning all TMDC heterostructure combinations are too vast for the extend of this introduction. Therefore I am focussing on aspects of importance for the scope of this thesis, namely the charge-carrier dynamics in TMDC heterostructures in dependence of the stacking angle configuration.

Due to the fact that the majority of heterostructures consisting of TMDC materials form type-II heterojunctions [17], charge-transfer occurs across the interface following optical excitation. Subsequently to the transfer interlayer excitons are formed, where the hole and electron reside in different layers [18–29]. These interlayer excitons took the spotlight of research soon after the discovery of the formation of the direct bandgap. The first experimental evidence showing an interlayer hole-transfer was found by *Hong et al* [29] for a MoS_2/WS_2 heterostructure (Fig. 2.3) in 2014. The transfer time, for the hole jumping across the interface, could only be determined with an upper threshold of 40 fs due to limitations in the experimental time-resolution. Nevertheless, it is astounding to see the charge-transfer in an only Van der Waals-coupled system to occur on such a short timeframe.

Since then there have been a multitude of studies measuring the transfer dynamics [30, 32, 48–52] for various assemblies of different TMDC materials. Recently it was shown that the charge-transfer is associated with a phonon-assisted tunneling pro-

cess [18], which can be deterred by adding buffer layers of hexagonal boron nitride [50]. At first glance it seems obvious that different stacking configurations would lead to a change of the transfer dynamics, since a rotational mismatch in real space leads to a rotational mismatch in k-space. Therefore do the charge-carriers bound in the form of excitons located at the K-points need to overcome a large momentum mismatch for misaligned samples. This would in turn increase the transition time between the layers.

However while there are systematic studies on the influence of the stacking configuration the results are inconclusive. The two central papers I want to mention here are by *Merkl et al* [48] and *Zhu et al* [49], with the former studying WSe_2/WS_2 and the latter MoS_2/WSe_2 heterostructures. WSe_2/WS_2 was studied by NIR pump-MIR spectroscopy. They pumped the WSe_2 resonantly and followed the evolution of the intralayer excitons by measuring the dielectric response of the heterostructure by electro-optic sampling of the MIR probe pulse. The results found were signatures of the generation of the interlayer excitons from which transfer as well as lifetimes could be estimated. The outcome implied that the stacking configuration heavily influences the tunneling rates between the layers, with a nearly aligned sample at 5° mismatch showing a tunneling rate of $\Gamma = (200\,\mathrm{fs}^{-1})$ and a misaligned sample at 27° showing a tunneling rate of $\Gamma = (1.2\,\mathrm{ps}^{-1})$.

In contrast to these conclusions stand now the results by *Zhu*. The time-resolved changes in a multitude of samples were measured by transient reflectivity experiments, where the charge-transfer was associated with a rise in reflectivity. While no clear correlation for the lifetime of the interlayer excitons with the stacking configuration was found, their study shows that the transfer time between the layers is not influenced by the stacking configuration either. Independent on stacking angle a charge-transfer time of less than 40 fs (time-resolution limited) was extracted for angles between 1° and 29°.

In conclusion we can infer, that while there have been studies concerning the charge-transfer, the underlying mechanism remains elusive to this day. Therefore **articles II** and **III** contribute to the progress of the ongoing investigation concerning the charge-transfer.

2.2   Optical Second-Harmonic Generation

In the following section applications and functionality of optical second-harmonic generation as an experimental technique are introduced. For a more detailed description of the process please refer to literature [6, 53]. For a more focussed description adhering to the applied setup the supplemental information of **article I** can be referenced.

The process of second-harmonic generation for an electromagnetical wave can be
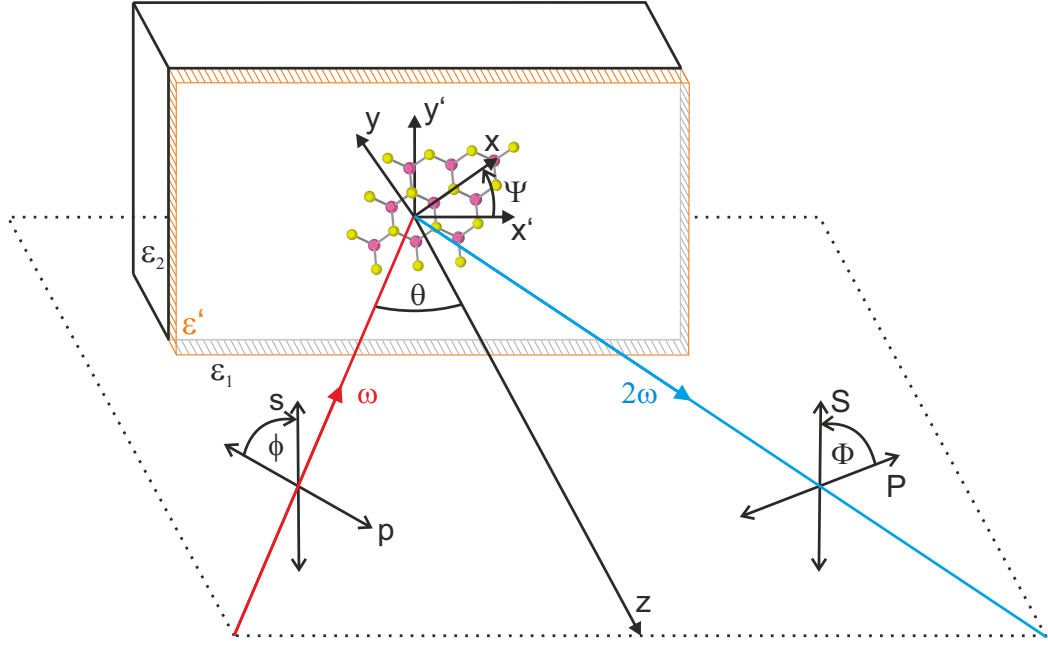
Fig. 2.4: Sketch of the geometry of the experiment. In red the incoming beam of the fundamental (ω) is delineated, in blue the generated second-harmonic (2ω). The dashed rectangle marks the plane of incidence, θ the angle of incidence. ϕ and Φ describe the angle of the polarization for the incoming beam as well as for the second-harmonic in relation to the plane of incidence. x', y' denote the lab coordinates and x,y the crystal coordinates. Ψ depicts the rotation of the crystal coordinates in relation to the lab system. The different ϵ describe the involved dielectric environments.

described by the nonlinear polarization in dipole approxmiation as:

$$\mathbf{P}^{(2)}(2\omega) = \epsilon_0 \chi^{(2)}(2\omega) : \mathbf{E}(\omega)\mathbf{E}(\omega) \tag{2.1}$$

with $\chi^{(2)}$ as the second order nonlinear susceptibility. For the more general case of sum-frequency generation, $\chi^{(2)}$ would be a third-order tensor with 27 elements. However, the amount of independent tensor elements is reduced for the case of second-harmonic generation to a 3×6 matrix:

$$\chi^{(2)} = \begin{pmatrix} \chi^{(2)}_{xxx} & \chi^{(2)}_{xyy} & \chi^{(2)}_{xzz} & \chi^{(2)}_{xzy} & \chi^{(2)}_{xzx} & \chi^{(2)}_{xxy} \\ \chi^{(2)}_{yxx} & \chi^{(2)}_{yyy} & \chi^{(2)}_{yzz} & \chi^{(2)}_{yzy} & \chi^{(2)}_{yzx} & \chi^{(2)}_{yxy} \\ \chi^{(2)}_{zxx} & \chi^{(2)}_{zyy} & \chi^{(2)}_{zzz} & \chi^{(2)}_{zzy} & \chi^{(2)}_{zzx} & \chi^{(2)}_{zxy} \end{pmatrix}. \tag{2.2}$$

Here x, y, and z refer to the crystal coordinates. For the case of TMDC material monolayers, the tensor is further reduced because of their inherent D$_{3h}$ symmetry [6, 53], leaving only four non-zero tensor elements:

$$\chi^{(2)}_{xxx} = -\chi^{(2)}_{yyx} = -\chi^{(2)}_{xyy} = -\chi^{(2)}_{yxy} \tag{2.3}$$
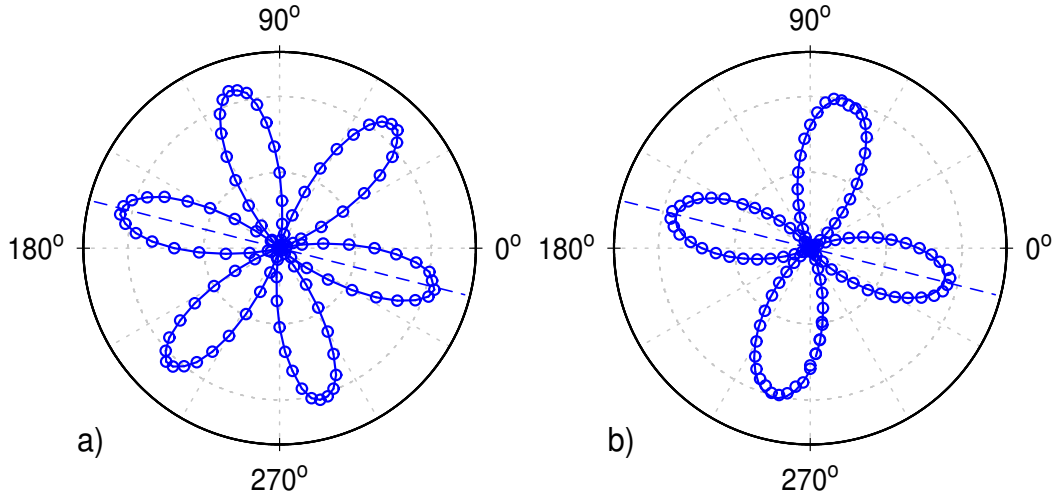
Fig. 2.5: Two examples for the two types of SHG anisotropy measurements. The intensity of the generated second-harmonic is plotted. In a) the crystal is rotated, in b) the polarization of the incoming fundamental. The offset is determined by the initial angle between the x-coordinate of the labsystem and the armchair direction of the crystal (dashed lines). The lines mark fits to the data.

This leads to a fairly simplified nonlinear susceptibility tensor:

$$\chi^{(2)} = \chi^{(2)}_{xxx} \begin{pmatrix} 1 & -1 & 0 & 0 & 0 & 0 \\ 0 & 0 & 0 & 0 & 0 & -1 \\ 0 & 0 & 0 & 0 & 0 & 0 \end{pmatrix}. \tag{2.4}$$

Due to the Van der Waals nature of the exfoliated TMDC flakes, arbitrary angles of the crystal in relation to lab coordinates are possible (see Fig. 2.4). Said rotation then translates to a transformation of the susceptibility leading to a tensor in the form of:

$$\chi^{(2)} = \chi_{xxx} \cdot \begin{pmatrix} \cos(3\Psi) & -\cos(3\Psi) & 0 & 0 & 0 & -\sin(3\Psi) \\ -\sin(3\Psi) & \sin(3\Psi) & 0 & 0 & 0 & -\cos(3\Psi) \\ 0 & 0 & 0 & 0 & 0 & 0 \end{pmatrix}. \tag{2.5}$$

With this final form we can apply the model developed by Heinz [54] in order to directly access the electric field strength of the generated optical second-harmonic:

$$\mathbf{E}(2\omega) = \frac{i2\omega}{c\sqrt{\epsilon_i(2\omega)}} \frac{2\pi}{\cos(\theta)(2\omega)} \mathbf{F}(2\omega)\chi^{(2)}\mathbf{f}(\omega)|\mathbf{E}(\omega)|^2. \tag{2.6}$$

Here $\mathbf{F}(2\omega)$ and $\mathbf{f}(\omega)$ represent the Fresnel factors which describe the interaction of the incoming and outgoing electric fields with the dielectric medium of the sample and the underlying substrate. From this form the measured intensity can be estimated for different scenarios. Firstly, rotation of the sample in relation to the incoming and

outgoing electric field, or secondly rotation of the incoming polarization in relation to the outgoing field and sample. Omitting the Fresnel factors and assuming an angle of incidence perpendicular to the surface, we find a simplified version for E:

$$
\begin{aligned}
\mathbf{E}_{\mathrm{P}}^{2\omega}(\phi) &\propto \cos(2\phi + 3\Psi) \\
\mathbf{E}_{\mathrm{S}}^{2\omega}(\phi) &\propto \sin(2\phi + 3\Psi)
\end{aligned}
\tag{2.7}
$$

depending on the crystal orientation as well as the polarization of the incoming fundamental, for either outgoing S- or P-polarized light. From this equation the relation of the crystal orientation and intensity becomes directly apparent. When the crystal is rotated, we find a six-fold symmetric pattern, offset by the angle between the armchair direction of the crystal and the x-coordinate of the labsystem. When the polarization is rotated, a two-fold symmetrical pattern is measured, which is also offset by the crystal orientation. Both methods therefore give direct access to the relative crystal orientation as can be seen in Fig. 2.5.

2.3 Second-Harmonic Imaging Microscopy

In this section second-harmonic imaging microscopy shall be introduced. The design and build-up for the setup is a central part of this dissertation and the groundwork on which **article I** is based on.

The concept for optical second-harmonic imaging microscopy was born out of necessity since the study of TMDC materials is to this day limited to sample sizes in the $(100\mu\mathrm{m})^2$ range. Therefore, an experimental technique with an enhanced spatial resolution in that size-regime is mandatory. The newly built setup was based on a previously study done in our workgroup [55]. This concept was extended and re-imagined in the form of the setup illustrated in Fig. 2.6.

SH imaging microscopy combines the advantages of time-resolved SHG with an optical microscopy setup. The generated SH of the sample is imaged via a camera lens magnified onto a CCD chip. The imaged area corresponds here to a field of view of $400 \times 400 \, \mu\mathrm{m}^2$ with a spatial resolution better than $4 \, \mu\mathrm{m}$ at a magnification factor M of $\approx 35\text{-}40$.

As explained in Section 2.2, by rotating the polarization of the incoming fundamental the crystal orientation can be extracted as shown in Fig. 2.7. Here the intensity is extracted from rectangular ROIs and plotted against the polarization angle. By applying a fitting routine adjusted to equation 2.6, the crystal orientation is deduced as can be seen for the exemplary evaluation of flakes in Fig. 2.7 c) and d). This concept can be extended to the whole field of view allowing for simultaneous evaluation.

The result can be seen in Fig. 2.8, where in a single experiment, the orientation of all crystal flakes in the field of view can be evaluated without scanning the laserspot.
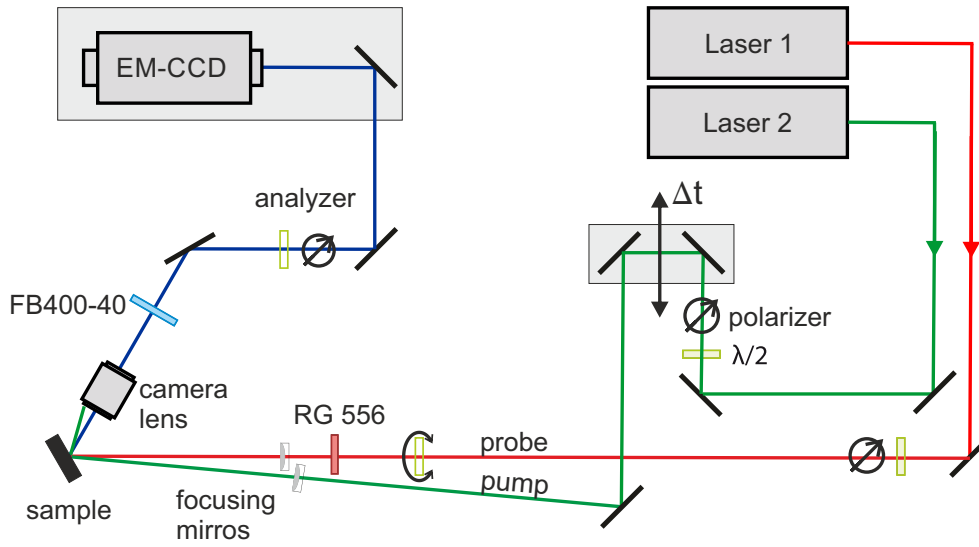
Fig. 2.6: Sketch of the experimental setup for second-harmonic imaging microscopy. The setup is used in two laboratories with the same buildup. The photon energies for the individual setups available are: 1.55 eV (probe) and 2.58 eV-1.65 eV (pump) (Laserlab) and 1.3 eV-1.9 eV for pump and probe (Femtolab). Pulselengths are routinely below 50 fs. For more details consult the individual articles.

This approach is considerably faster than the often applied technique of scanning the strongly focussed laserspot across the sample, measuring the response of individual spots and stitching them together [23, 25, 56, 57]. This allows for a much quicker screening of samples for homogeneity, as well as the identification of crystal impurities like twins.

But the experimental technique is of course not limited to the evaluation of crystal orientation and quality. By applying a pump-probe scheme to the setup time-resolved changes of the second-order nonlinear susceptibility can be monitored and evaluated. These changes can be attributed to the generation of intralayer excitons [58], which allows the study of the formation time as well as the lifetime of intra- and interlayer excitons. Furthermore, it allows the application of polarization and time-resolved measurements for the extraction of charge-carrier dynamics of individual layers inside heterostructures, which will be elaborated further in section 3.2.

Another unique feature of our setup in comparison to more conventional approaches in time-resolved linear spectroscopy [18, 19, 27, 29–32] is that here the amount of dispersion introducing elements in front of the sample was reduced to an absolute minimum. Therefore a superior time-resolution of about 10 fs can be reached, without which the results of **article III** would have been unattainable.
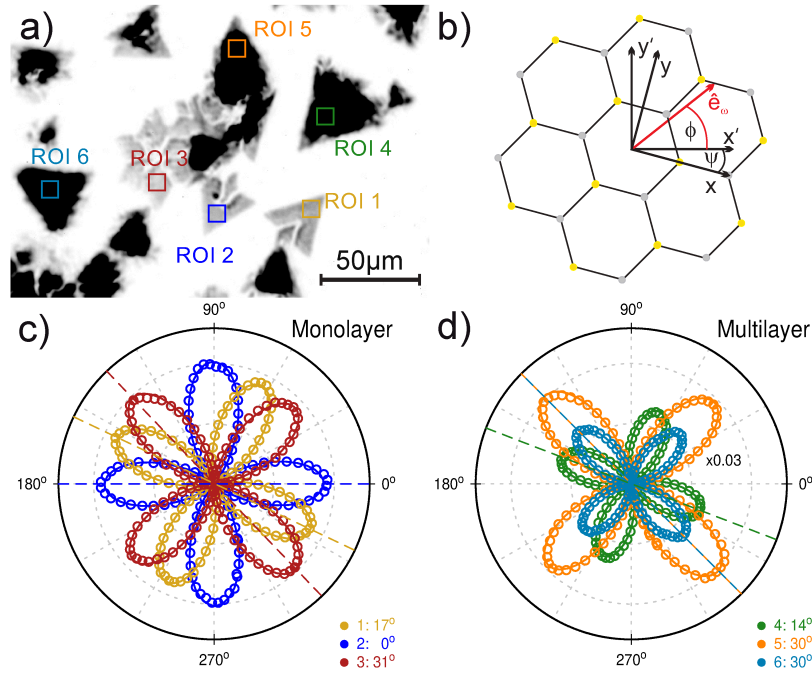
Fig. 2.7: Evaluation of crystal orientation by means of polarization anisotropy measurements for MoS_2 mono- and multilayers. a) shows the zoomed in part of the SH image from Fig. 2.8 and the regions of interest (ROI) from which the intensity was extracted. b) depicts a sketch of the crystal lattice in relation to the lab coordinates and therefore the offset in the polarization anisotropy measurements. c) and d) portray the polarization dependent measurement data extracted from the ROIs as well as the extracted crystal orientation. The dashed lines mark the position of the armchair direction of the measured crystal. Figure from **article I**.
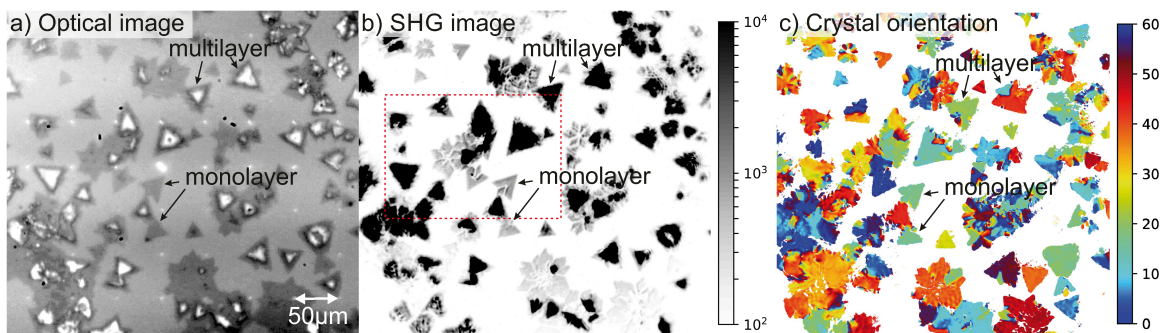

Fig. 2.8: Side-by-side comparison of an optical microscope image (a), a SH imaging microscope image (b) and the large scale evaluation of the crystal orientation (c). The full frame shows an area of $400 \times 400 \, \mu m^2$. c) shows the results of the automated evaluation of the crystal orientation for the individual flakes in a false color plot in modulo of 60°. The dashed rectangle marks the evaluated region of Fig. 2.7. Figure from **article I**.

Chapter 3

Results and Discussion

In order to fully understand the charge-transfer in TMDC heterostructures, all underlying processes and mechanisms need to be explored by systematic studies with carefully controlled parameters. To do so we devised a setup capable of selectively accessing changes of the second order susceptibility for individual layers in HS on a femtosecond timescale (**article I**, Section 3.1).

Building on this first success we were able to identify that charge-transfer occurs bi-directionally across the $MoSe_2/WSe_2$ interface subsequent to resonant excitation of intralayer excitons (**article II**, Section 3.2).

In the following chapter a closer examination of the electron transfer in MoS_2/WSe_2 heterostructures and its dependence on the stacking configuration (**article III**, Section 3.3) is illuminated.

As a possible prospect for future endeavours, first measurements were performed on a new material class, chiral hybrid metal halides (**article IV**, Section 3.4), which might become another important building block in the vast family of two-dimensional materials.

3.1 Mono- and Multilayer Dynamics in MoS_2

The goal of this work was to enable study of charge-carrier dynamics in samples of sizes routinely smaller than $(100\mu m)^2$. In order to reach this objective, the experimental setup for optical second-harmonic imaging microscopy was designed and built. Considering the contemporary nature of our approach **article I** focussed on showcasing the capabilities of the setup as well as establishing first results for systematic time-resolved SH studies for the TMDC material used in the majority of research articles to this day (MoS_2).

The major advantages of our approach have already been shown in Section 2.3. Here the results for the time-resolved measurements are discussed. Fig. 3.1 shows an overview of the results. Subsequent to the optical excitation, a homogeneous decrease becomes visible in the whole field of view. After extracting the intensities from the marked ROIs and plotting the normalized transients against the pump-probe delay, the dynamics can be extracted by fitting an exponential recovery to the data.
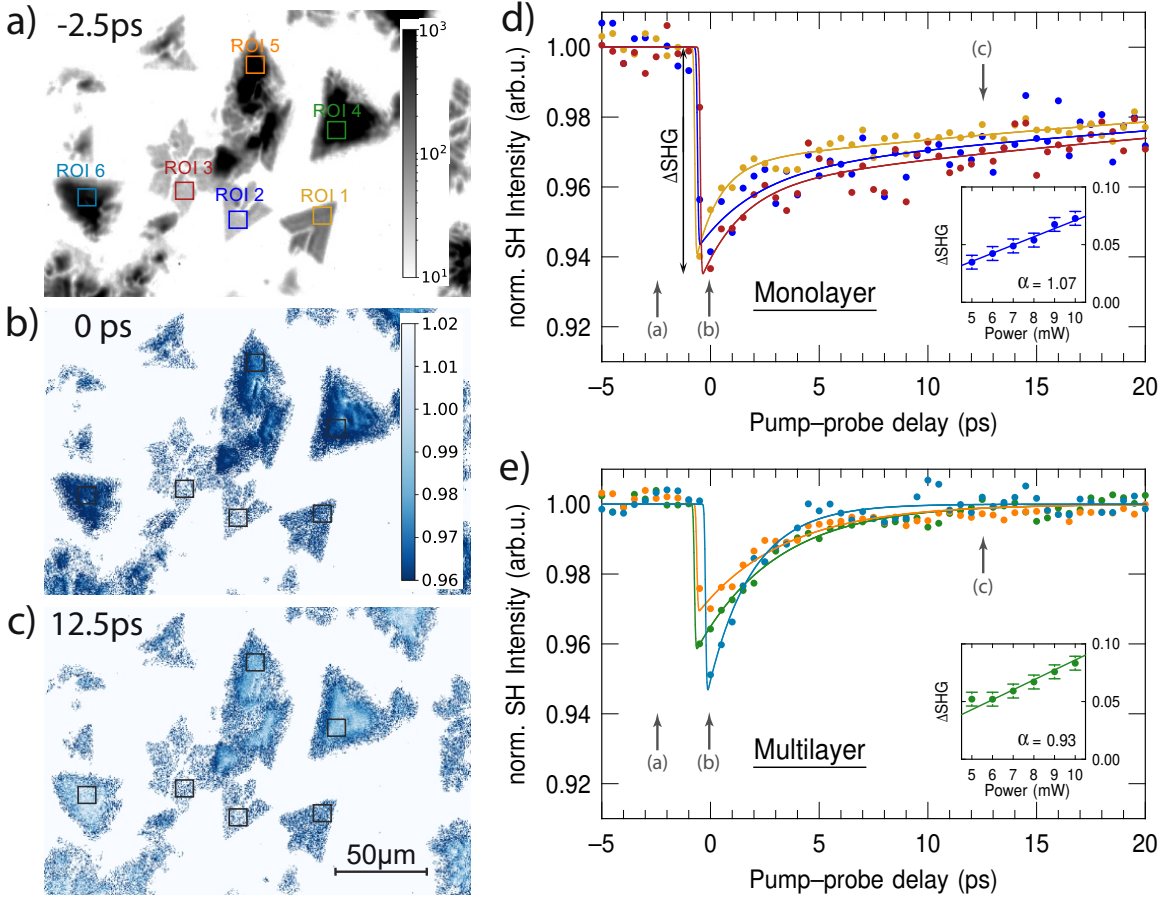
Fig. 3.1: Time-resolved SHG measurements on mono- and multilayer MoS_2 for optical excitation at 2.07 eV. a)-c) Depict the pump-induced changes in the SH images for three different points in time: Before arrival of the pump, at temporal overlap and 12.5 ps after temporal overlap. d) and e) show time-resolved traces for the intensity extracted from the ROIs for mono- and multilayer regions of the sample. The points in time from which the images were taken are delineated by arrows. The inset shows the pump-fluence dependency of the decrease in intensity at temporal overlap. Figure from **article I**.

The nature of the decrease is identified to be the injection of excitons in the material, due to the pump-energy tuned to 2.07 eV slightly above the B-exciton resonance [59, 60] of MoS_2. This interpretation is further corroborated by the linear dependency of the decrease in intensity on the pump-fluence [61]. Therefore, the signal can be correlated to the exciton density in the material and we are able to monitor the excitonic lifetimes.

While the dip in intensity scales linearly with the pump-fluence, the dynamics remain unchanged, allowing us to repudiate other exciton density dependent decay processes like exciton-exciton annihilation [62]. A comparison between transients from different ROIs reveals a very reproducible recovery behavior with significant differences between mono- and multilayer areas. While the monolayer shows a bi-

exponential recovery rate, the multilayer exhibits a single exponential behavior. Averaging over all monolayer samples we find an initial decay rate of $\tau_1 = 1.9 \pm 0.7$ ps, followed by the slower time-constant of $\tau_2 = 48.5 \pm 2.1$ ps. Comparing the found relaxation times with results found by conventional time-resolved linear spectroscopy we find that they match reasonably well [63, 64]. However, further research reveals, that the reported time-constants are rather wide spread. Single- [65–67], bi- [30, 62, 64, 68–70], and tri-exponential [63, 71] behavior has been reported, with a wide range of time-constants extending from 500 fs up to 500 ps.

In contrast to the monolayer, the time-constant found for the multilayers is $\tau_1 = 3.2 \pm 0.9$ ps. Examining the different lifetimes between the mono- and multilayer behavior, it becomes clear that the multilayer recovers on a much faster timescale. In order to elucidate the cause for this behaviour further literature inquiry is mandatory. Unfortunately, the amount of studies directly comparing dynamics of mono- and multilayers are scarce and report contrary results. *Shi et al* found slightly smaller time-constants for few-layered systems without giving an explanation of the physical origin [63]. *Wang et al*, in disagreement to these results, found an increase of time-constant with layer thickness, which was attributed to the increased volume to surface ratio in multilayer samples, since they identified the larger defect density at the surface as their main recombination channel [72].

The obvious discrepancy between their work and our study might be caused by a different stacking configuration (*i. e.* 2H vs 3R) or a difference in defect density/distribution due to a difference in sample preparation (CVD vs. exfoliated). Since the changes for the bandstructure between 2H- and 3R-stacked samples are negligible [11, 73], a higher homogeneity of defects seems plausible for CVD grown samples in contrast to exfoliated samples. In consideration of the indirect bandgap of multilayers of MoS$_2$, one logical conclusion is that after excitation at the K-point, the charge carriers relax to the band mini-/maxima located at Σ- and Γ-point. The states making up these bands are of hybridized nature and therefore delocalized over multiple layers, enabling efficient charge-transfer [74, 75]. Following this reasoning a feasible explanation for the reduced lifetime in our multilayered samples presents itself: faster trapping via defects facilitated by efficient transport through the multilayers.

The results from **article I** presented here clearly illustrate the capabilities of our setup and enabled further successful systematic studies of interlayer charge-transfer excitons in **article II** and **III**.

3.2   Directional Charge-Transfer in MoSe$_2$/WSe$_2$

Following the proof-of-principle experiments presented in section 3.1, the next logical step is obvious: study of a heterostructure sample.

The sample was provided to us by the group of J.C. Hone at the Columbia University and consists of two monolayers of MoSe$_2$ and WSe$_2$, which were sandwiched between thicker layers of hexagonal boron-nitride to ensure longevity of the sample [76–78]. The polarization dependent measurements shown in Fig. 3.2 revealed a stacking angle of 32.3°.
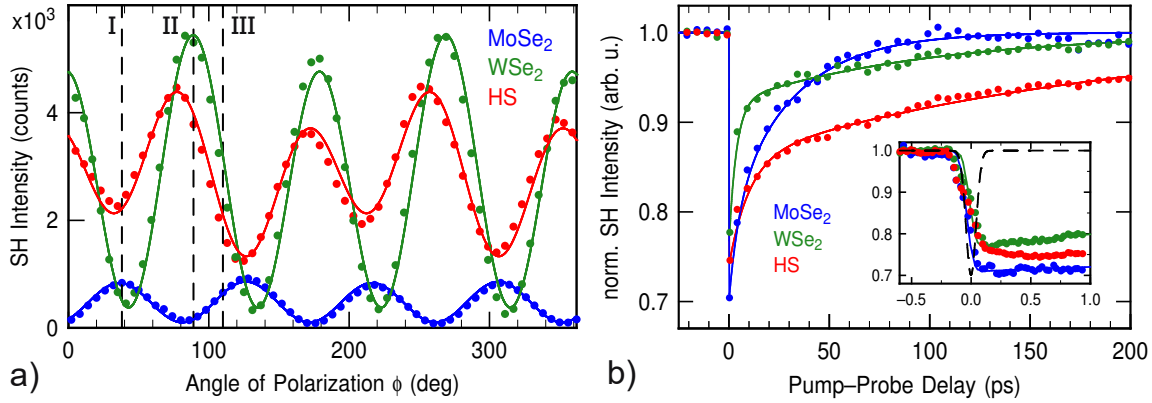

Fig. 3.2: Polarization- and time-resolved SHG measurements performed on a MoSe$_2$/WSe$_2$ heterostructure. a) Polarization dependent SH measurement. Color coded are the signals from the monolayers (blue: MoS$_2$, green: WSe$_2$) and the HS (red). The latin numerals mark the probe polarization utilized in the measurements of this study. Lines are fits to the data. b) Time-resolved SH measurements with the same colorcode. The system is pumped with a photon energy of 2.09 eV resonant with the B-exciton of WSe$_2$. All datasets are normalized to an average signal before arrival of the pump-pulse. The inset shows a zoom-in to the time frame around temporal overlap, where the dashed line represents the cross-correlation. Figure from **article II**.

Probe polarization III was chosen for first time-resolved measurements, since both layers give a considerable signal at this angle. As can be seen in Fig. 3.2 b) the HS behaves fundamentally different in comparison to the monolayers. While there is an initial decrease for all regions, on a longer timescale of up to 200 ps the reduction in SH signal persists while the recovery in the monolayers is comparably faster. This behavior is the first indication, that what is measured in the HS are the sought-for charge-transfer interlayer excitons. As a consequence of their spatially indirect nature, the lifetime for charge-transfer excitons is increased strongly in contrast to their intralayer counterparts [27]. The second piece of evidence that the signal manifesting in the heterostructure is caused be the formation of interlayer excitons, becomes apparent on closer examination of the time frame around temporal overlap. While the decrease of the signal follows the anticipated shape of the cross-correlation of the laserpulses, followed by immediately starting recovery, for the heterostructure it keeps
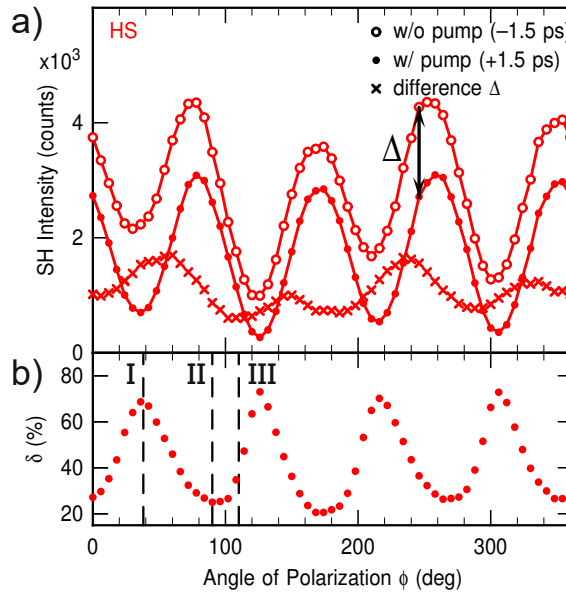
Fig. 3.3: Pumped polarization-dependent measurement of the MoSe$_2$/WSe$_2$ hetero-structure before and after temporal overlap. a) The upper part of the graph shows the polarizational anisotropy measurement for the HS before arrival of the pump beam (open circles) and after arrival of the pump beam (filled circles), as well as the difference between the two (crosses). The lower part shows the difference between the baseline and the pumped signal, but normalized to the base intensity of the unpumped system, therefore revealing the pump induced change of the intensity in percent. Figure from **article II**.

declining even after the pump-pulse has fully subsided. This delayed filling serves as further confirmation that charge-transfer is occurring in the HS.

One of the central advantages of our setup is the intrinsic sensitivity of SHG to the crystal symmetry. This feature can be applied by tuning the probe polarization to enhance the sensitivity to individual layers. In combination with time-resolved measurements the importance of this unique feature of our technique is further underlined. In Fig. 3.3 a pumped polarization anisotropy is depicted. For these measurements polarization anisotropies are recorded while the system is pumped, once before arrival of the pump-pulse and once after. Evaluation by subtraction of the pumped signal from the base signal already reveals a clear anisotropy, which becomes even clearer after normalization of the difference to the basesignal. The normalized signal shows the pump-induced change in % depending on the probe polarization, which shows an enormous deviation of the signal in a range from 25% up to 75%.

At first glance this strong change might come surprising, however on closer examination and by comparing the angle of maximally induced change with the deduced crystal orientation from Fig. 3.2, a self-evident explanation presents itself. The strongest decrease coincides perfectly with the maximum intensity of the MoSe$_2$ monolayer (polarization **I**). Thus, we see an enormous anisotropical decrease of the SH intensity when resonantly pumping the B-exciton of WSe$_2$, while the probe is most
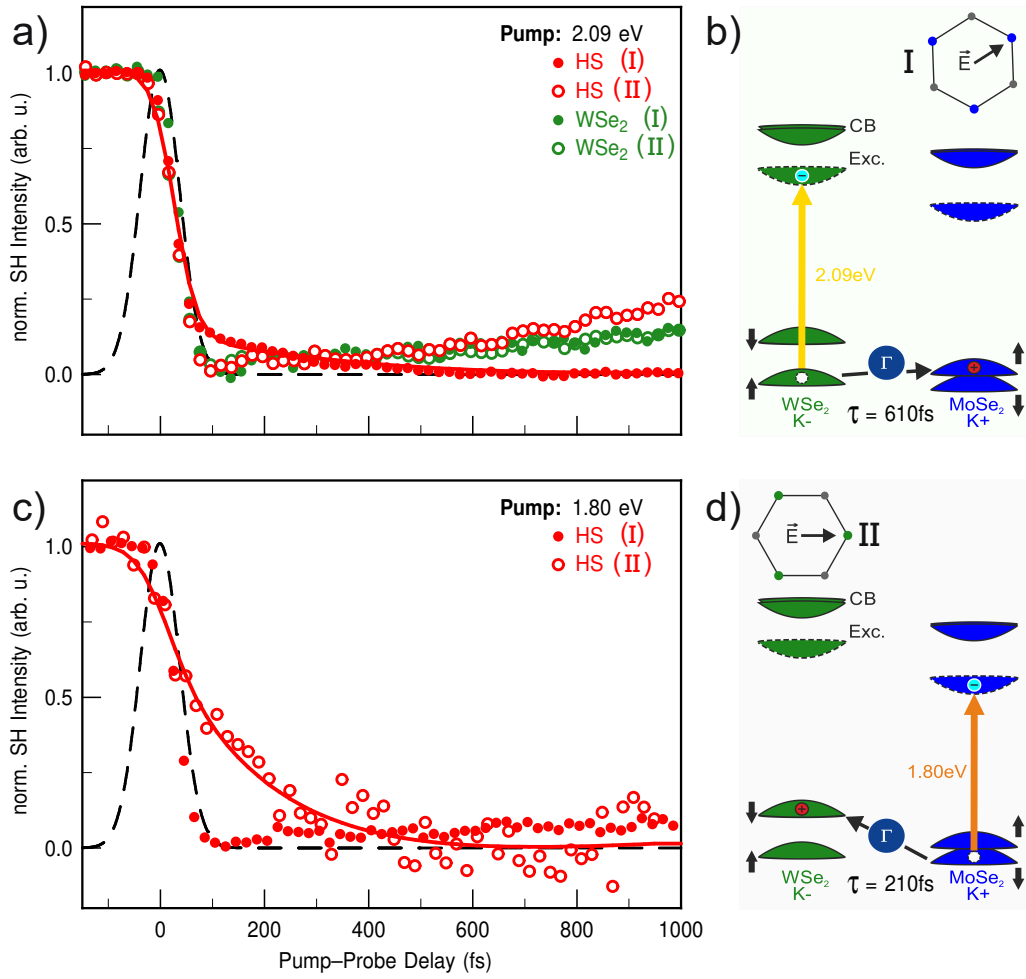
Fig. 3.4: Time-resolved SHG measurements for $MoSe_2/WSe_2$ for two different probe polarizations and two pump-photon energies. The sketches illustrate the occurring charge-transfer and the energy alignment. a) and c) show the normalized pump-induced decrease in SH intensity plotted against the pump-probe delay for 2.09 eV photon-energy and 1.80 eV. b) and d) are sketches depicting the band alignment of the HS and the hole transfer route and transfer times for both energies. Furthermore they show the probe polarizations measured in a/c. Figure from **article II**.

sensitive to the $MoSe_2$ in the HS. This seems contradictory at first glance, however it matches well with our interpretation of the delayed signal being caused by the interlayer charge transfer.

This reasoning is corroborated further by a systematic variation of the probe polarization and the pump energy illustrated in Fig. 3.4. For resonant excitation of WSe_2 at 2.09 eV by switching between polarizations **I** (sensitive to $MoSe_2$) and **II** (sensitive to WSe_2), we can switch the delayed filling on and off. Furthermore, while the delayed filling is not visible does the measured transient heavily resemble the WSe_2 monolayer trace, only with a slightly shorter timeconstant. The conclusion
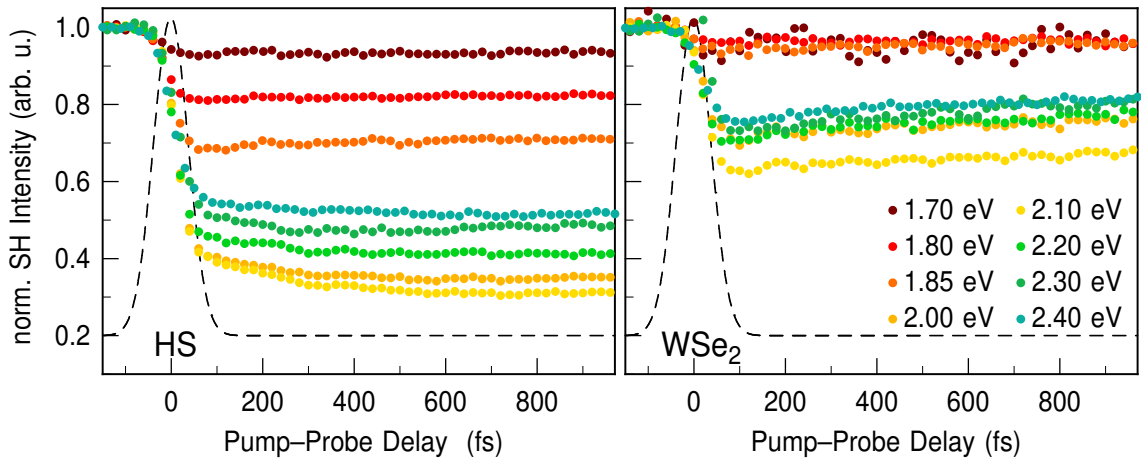
Fig. 3.5: Energy dependent measurements for the HS and WSe$_2$ monolayer. The pump-photon energy is varied between 1.70 eV and 2.40 eV. A clear resonance is visible around the WSe$_2$ B-exciton energy for both the HS and monolayer. Figure from the SI of **article II**.

drawn from this behavior is, that the delayed filling is caused by a hole transfer from the lower lying valence band across the interface into the MoSe$_2$.

From a rate-equation model the associated transfer time can be extracted and is found to be $\tau_{\text{WSe}_2 \to \text{MoSe}_2} = 610 \pm 150$ fs. The process can be reversed by tuning the pump-photon energy to the B-exciton resonance of MoSe$_2$ at 1.80 eV. At this energy a delayed filling still occurs, but now only for polarization **II** signifying the reversal of the transfer and classifying the process as a hole transfer from MoSe$_2$ into WSe$_2$. The discerned transfer time is in this case $\tau_{\text{MoSe}_2 \to \text{WSe}_2} = 210 \pm 60$ fs. The corresponding fits are shown in Fig. 3.4 as solid lines.

As some closing remarks, I want to comment on the influence hybridized, delocalized states at the Γ-point have on the efficiency of the charge-transfer. In the past it has been proposed that intermediate states located at the Γ- and Σ-points of the Brillouin zone play a central role for the charge transfer in momentum-mismatched TMDC heterostructures [25, 56, 57, 74, 79, 80]. Band structure calculations show that conduction band states at the Σ-point shift energetically below the K-point minimum for certain stacking angles [56]. Moreover do these states show strong hybridization of the individual wavefunctions of the monolayers [56, 57, 74], and therefore enable a more efficient interlayer transfer.

Further evidence for this process is given by two-photon photoemission measurements on bulk MoS$_2$, where ultrafast charge transfer to the Σ-point has been observed [81], corroborating further the strong influence these states may have on the charge transfer in heterostructures. This attribution is consolidated further by systematic measurements changing the pump-photon energy successively to explore the charge transfer from WSe$_2$ to MoSe$_2$ in more detail (Fig. 3.5). Here, the pump-induced decrease of the SH intensity shows a clear resonance around the B-exciton

energy of WSe$_2$, (2.09 eV [60, 82]). Furthermore, the delayed filling signifying the ultrafast charge transfer to MoSe$_2$ is only observed for excitation energies equal to or higher than the WSe$_2$ B-exciton resonance. Since it is known from bandstructure calculations that the Γ-point in the heterostructure is energetically located between the valence band maxima of the individual monolayers [56, 57], the activation of this transfer channel for higher excitation energies underlines the importance of the Γ-point for the charge transfer, which will be further explored in **article III**.

Similarly, our measurements also indicate ultrafast hole transfer from the MoSe$_2$ K$_+$ to WSe$_2$ K$_+$ valley after optical excitation of MoSe$_2$ A-excitons (see supplementary of **article II**). However, there is no experimental evidence for electron transfer from WSe$_2$ to MoSe$_2$ after resonant excitation of WSe$_2$ A-excitons. This result suggests, that electron transfer in our heterostructure is either faster than the experimental time-resolution of ≈ 15 fs or not feasible due to the relatively large stacking angle. Of course, the charge transfer could also be so slow or inefficient, that its particular signature is superimposed by the faster monolayer dynamics.

A recent study of a WS$_2$/WSe$_2$ heterostructure has observed electron transfer occurring within 200 fs and 1.2 ps after resonant excitation of WSe$_2$ A-excitons depending on the rotational mismatch [48]. While the order of magnitude compares reasonably well with our extracted transfer times for interlayer hole transfer, the question remains why an electron transfer is not observable for our particular heterostructure. Overall **article II** has successfully established the special advantages of our setup and how we were able to utilize them to the fullest by identifying a bi-directional charge-transfer.

3.3 Twist-Angle Dependency of the Charge-Transfer

After establishing the capabilities of our system to detect interlayer excitons, systematic studies concerning the influence that the stacking configuration has on the dynamics are mandatory. The samples studied in **article III**, consisting of multiple MoS_2/WSe_2 heterostructures with different stacking angles, were provided to us by T. Korn.

In a previously published paper [23] it was established for these samples, that for all stacking configurations photoluminescence arose at a photon energy below the A-exciton energies of the individual materials involved (cf. Fig. 3.6). In their study
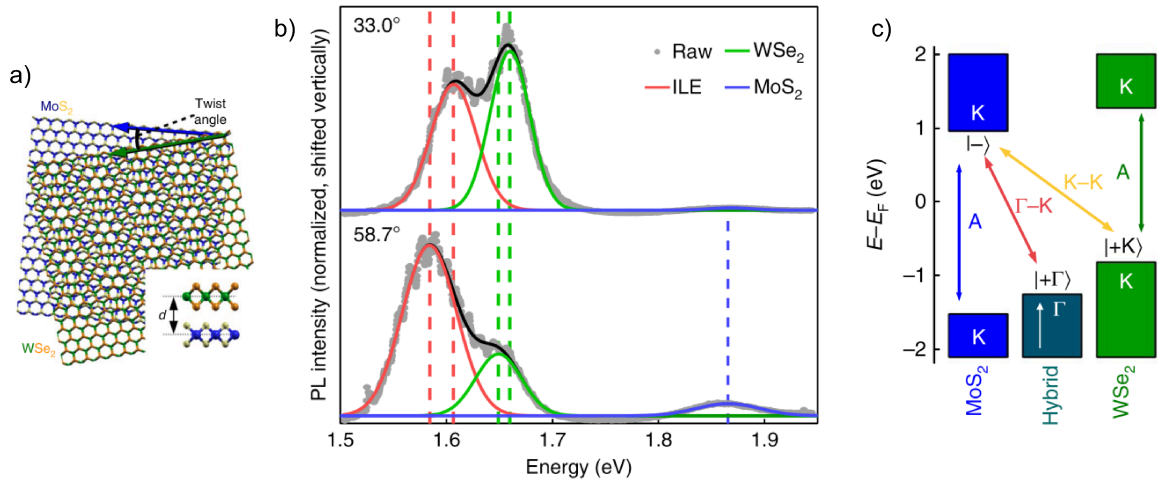

Fig. 3.6: Photoluminescence measurements for different stacking angles of MoS_2/WSe_2 heterostructures. a) Sketch illustrating the involved materials and the stacking angle. b) Photoluminescence measurements for two stacking configurations. For both angles the characteristic heterostructure PL lies energetically below the A-exciton peaks of the individual materials. c) Sketch illustrating the energy alignment for the HS. The arrows mark possible (intra- and interlayer) exciton combinations. Figures from *Kunstmann et al* [23].

they have conclusively shown, that the arising PL (following 2.33 eV excitation) is caused by radiative recombination of interlayer excitons with electrons located at the K-point of MoS_2 and holes located at the Γ-point partially delocalized over both layers. These excitons are therefore doubly indirect in nature, in real space as well as in momentum space. Furthermore, it was shown in a recent study [83] that for well aligned heterostructures of the same material combination, direct interlayer PL occurs at a much smaller photon energy of 1.0 eV. We can therefore assume the presence of interlayer excitons for the studied specimen.

From polarization-resolved measurements we find that the stacking angles for the studied samples are: 9°(referred to quasi-3R), 52°(quasi-2H) and 16°(misaligned). Fig. 3.7 shows results for the time-resolved SH transients of all three samples. In
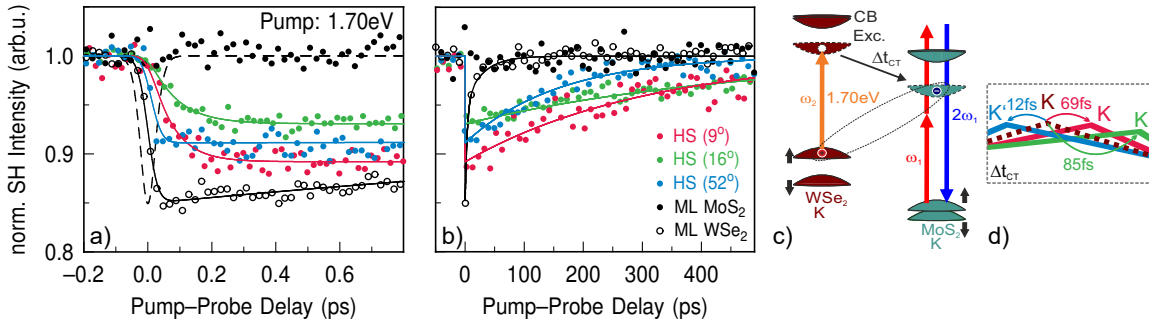
Fig. 3.7: Time-resolved SHG of the MoS_2/WSe_2 heterostructures for three different stacking angles for a pump-photon energy of 1.70 eV. The black datapoints describe monolayer dynamics, the colored points describe the individual heterostructures. a,b) Graphs show the time dependent recovery of the induced reduction of the SH signal measured with a probe polarization sensitive to the MoS_2 layer for the ultrafast and the slow time regimes. The dashed line represents the laser cross-correlation, solid lines correspond to rate-equation fits. c) Sketch of the energy alignment of the heterostructure with the initial excitation and the subsequent relaxation of the electron across the interface. d) Cutout from the Brillouin zone to illustrate the charge-transfer times for the respective samples.

order to isolate the charge-transfer and simplify the interpretation of the results, the combination of pump-photon energy and probe-polarization angle was chosen to be sensitive to MoS_2 whilst generating A-excitons in WSe_2 (1.70 eV) [60, 82]. The plotted curves are again normalized to the signal before arrival of the pump. Comparing the behavior of the monolayers in black with the HS, differences are revealed immediately. As expected, no pump-induced change is visible for the MoS_2 monolayer. Therefore any decrease in the HS signal can only be attributed to electron transfer from the WSe_2 following excitation.

For all samples a rapid decrease of the signal is visible, followed by a slower recovery. Upon closer examination further changes between the HS samples become apparent: While the quasi-2H stacked sample shows an expeditious decrease in intensity, the misaligned and quasi-3R stacked sample, keep decreasing up to 200 fs even after the pump-pulse has fully subsided (dashed line). So while there is clear evidence present for charge transfer in all HS samples, the dynamics differ considerably, with the quasi-2H stacked sample showing the fastest transfer, followed by the quasi-3R stacked sample and the misaligned sample showing the slowest transfer.

We apply a rate-equation model, where an energetically lower lying state is filled indirectly by a higher lying state populated via a gaussian pulse. This approach allows for a quantitative comparison of the results by giving access to the transfer times Δt_{CT} between the states. The extracted transfer times for the quasi-3R and the misaligned sample are comparable with values of 69 ± 10 fs and 85 ± 9 fs, respectively, whereas the transfer time for the quasi-2H stacked sample is more than five times faster (12 ± 4 fs).

At first glance, this large difference in transfer times comes as a surprise. The lattice separation between the layers, which was found to play a central role in the

tunneling probability [50], varies on a negligible level for 3R- and 2H-stacking. Therefore the transfer times should be comparable. However, this direct conclusion would disregard the wave function overlap between the layers, which not only factors in the transfer but also in the subsequent recombination dynamics [84]. Fortunately, there have been calculations of the wavefunctions for the interfacial plane in TMDC heterostructures that have revealed strong variations between 2H- and 3R-stacking [85], which then in turn can influence the transfer dynamics [86]. In conclusion, we deduce that the faster interlayer electron transfer for the quasi-2H stacked sample is caused by the increased lateral wavefunction overlap in the interfacial plane, facilitating a stronger interlayer interaction of the involved monolayer states at the K-points.

Following this reasoning we can further analyze the lifetimes of the interlayer excitons on a timescale of up to $500\,\mathrm{ps}$ subsequent to the excitation (Fig. 3.7b). While for all samples the lifetime is again severely enhanced in comparison to the monolayer of WSe_2 (as expected and seen before in **article II**), the observed lifetimes differ significantly between the three samples. A simple exponential fit allows for extraction of the lifetimes from the SH transients. The misaligned sample shows the longest ($467 \pm 16\,\mathrm{ps}$), the quasi-3R stacked sample an intermediate ($309 \pm 12\,\mathrm{ps}$) and the quasi-2H stacked sample the shortest lifetime ($158 \pm 10\,\mathrm{ps}$). The enhanced lifetime for the misaligned sample could be an indication for the absence of the radiative decay channel as it was reported recently [83]. The difference in lifetime between quasi-2H and quasi-3R can then be explained by the same reasoning as the enhanced transfer. Since the charge transfer via a phonon-assisted tunneling process can be amplified by the spatial overlap of the involved wavefunctions [18, 50], the same should hold for the reversed process of interlayer exciton recombination: A stronger spatial coincidence facilitates the recombination, resulting in a reduced lifetime.

In addition to this conclusive evidence for the influence the stacking configuration exerts on the electron dynamics, we want to shift the focus of attention to the hole transfer and the important role that states around the Γ-point play for charge-transfer and recombination at higher excitation energies. To accomplish this objective, the pump energy was tuned to $1.85\,\mathrm{eV}$-resonant to the A-exciton of MoS_2, while keeping the probe-polarization fixed to MoS_2. The results can be seen in Fig. 3.8. By comparing the dynamics of Figs. 3.7(a) and 3.8(a) striking differences become obvious: First of all, upon 1.85-eV photoexcitation the pump-induced effects now already start to occur precisely at temporal overlap in accordance with a direct excitation in MoS_2. With respect to the delayed filling, the SH transients of the quasi-3R and the misaligned sample stay similar, whereas the behavior of the quasi-2H stacked sample changes drastically. In contrast to the 1.70-eV excitation, where the SH signal of the quasi-2H sample was observed to recover mono-exponentially with a slow recovery rate, the SH response after 1.85-eV excitation begins to recover immediately on a femtosecond timescale. The extracted lifetime ($\tau_{2H} = 215\,\mathrm{fs}$) is only slightly slower than the corresponding monolayer decay times for 1.85-eV excitation
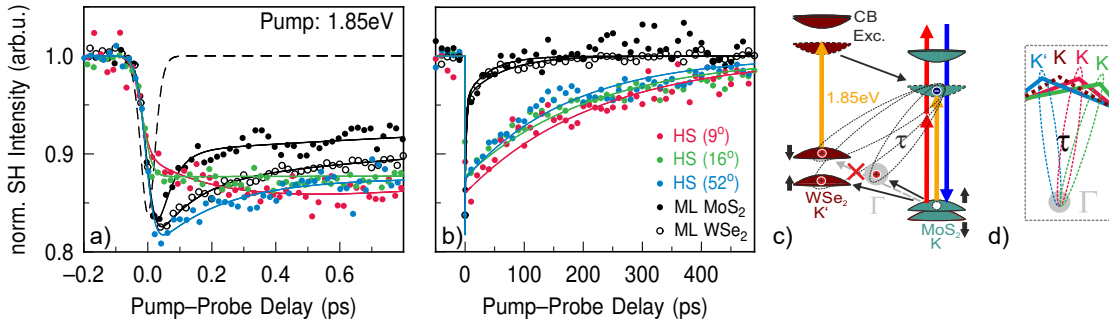
Fig. 3.8: Time-resolved SHG of the MoS_2/WSe_2 heterostructures for three different stacking angles for a pump-photon energy of 1.85 eV. The layout is the same as in Fig. 3.7. a/b) show the transients for the three samples. c) illustrates the induced dynamics in the form of a sketch. The higher excitation energy opens up additional relaxation pathways by ultrafast hole transfer to the hybridized Γ-point or to the K/K'-points of WSe_2. Three different kinds of conceivable interlayer excitons are marked by dashed ellipses. For the quasi-2H stacked sample, hole transfer to K' is spin-forbidden and only two transfer possibilities remain. d) shows the cutout from the Brillouin zone depicting the charge recombination via the Γ-point.

(τ_{MoS_2} = 44 fs, τ_{WSe_2} = 123 fs). This ultrafast decay process is associated with the coherent radiative recombination of intralayer excitons [87, 88].

On the one hand, the slightly slower recovery for the heterostructure signal compared to the monolayer can be explained by the change of the dielectric environment: The enhanced screening for the heterostructure decreases the binding energy of the excitons [89] and therefore increases their Bohr radius and the recombination time. On the other hand, the coherent radiative recombination competes with additional relaxation mechanisms in the heterostructure, such as hole transfer to the hybridized Γ-point or to the WSe_2 layer as illustrated in Fig. 3.8(c). Since at 1.85-eV excitation electron transfer from the WSe_2 into the MoS_2 is feasible as well, the detected SH signal in the MoS_2 is a mixture of various processes and a clear interpretation of our SH transients becomes more challenging.

The competing processes might also explain why we do not observe any clear ultrafast component for the quasi-3R and the misaligned heterostructure sample in our data. Another plausible explanation for the absence of the ultrafast decay in these two heterostructures could also be related to the energy alignment and the spin structure of the involved states. After photoexcitation inside the MoS_2 the generated hole has two obvious relaxation pathways alternative to intralayer recombination: it can either be scattered to the hybridized states around the Γ-point or to the K/K'-point in WSe_2.

In the case of 2H-stacking, transfer to the valence band maximum of WSe_2 at K' is spin forbidden as sketched in Fig. 3.8(c). For the misaligned sample, scattering to K/K' should also be reduced due to the large momentum mismatch. In contrast, hole transfer to the valence band maximum at the K-point should be most efficient in case of 3R-stacking. Assuming the hole transfer to K/K' to be a competing process

to the coherent recombination and taking place on a similar or faster timescale, the decreasing efficiency of the hole transfer to K/K' from quasi-3R, misaligned to quasi-2H could then explain the increasing manifestation of the coherent recombination.

The comparison of the SH transients at large pump-probe delays for both excitation energies in Figs. 3.7(b) and 3.8(b) reveals a surprising change in the dynamics caused by the higher excitation energy. For 1.70-eV excitation the recovery rates of the three heterostructure samples differ considerably as discussed above. In the case of 1.85-eV excitation, however, the lifetimes become very similar for all samples (quasi-2H: 180 ± 9 ps, quasi-3R: 217 ± 8 ps, misaligned: 220 ± 5 ps). For 1.70-eV excitation, the quasi-2H configuration showed the fastest recovery time due to the larger wavefunction overlap between the layers. For 1.85 eV, however, the lack of interaction between the layers for the other two samples is compensated by the additional decay routes of the charge carriers generated in the MoS_2. The central difference between the two excitation energies is that for 1.85-eV excitation the hole states around the Γ-point become energetically available. Photoluminescence from momentum-space indirect Γ-K interlayer excitons has been observed for all examined stacking configurations of MoS_2/WSe_2 [23]. Therefore, we attribute our observed decay dynamics to the radiative recombination of Γ-K interlayer excitons. Due to the fact that the states around the Γ-point consist inherently of orbitals which are delocalized and therefore spread out over both layers, the overlap of the wavefunctions of electron and hole is enhanced and, thus, radiative recombination is facilitated. This overall enhancement of the recombination compensates the reduced overlap for the quasi-3R and misaligned sample, equalizing the lifetimes of the excitation independent of the stacking configuration.

In conclusion, in **article III** we were able to unambiguously show the influence of the stacking angle on the charge-transfer and recombination dynamics in MoS_2/WSe_2 HS. For lower excitation energies the charge transfer is heavily dominated by the stacking configuration decelerating the electron transfer by a factor of seven when going from a quasi-2H stacked sample towards misalignment. These results would have been impossible to obtain without the superior time-resolution of our setup. While the interpretation becomes more difficult for higher excitation energies, the important role of the hybridized states around the Γ-point for charge-recombination was clearly shown. As soon as those decay channels become energetically available they dominate the recombination behavior, matching well with the results of *Kunstmann et al* [23].

3.4   Chiral Hybrid Metal Halides Displaying Second-Harmonic Generation

The already vast zoo of two-dimensional materials is ever expanding. In order to access even more possible applications and new phenomena, discovery and development of new material candidates is vital. Chiral hybrid metal halides are aspiring to join the 2D family, which we began exploring together with the group of J. Heine of the Chemistry Department in Marburg. The backbone of these molecules are the anionic $[E_2X_{10}]^{-4}$ building blocks, where E and X are various combinations of Sb, Bi and Cl, Br and I respectively (Fig. 3.9). The cations in the crystal structure,
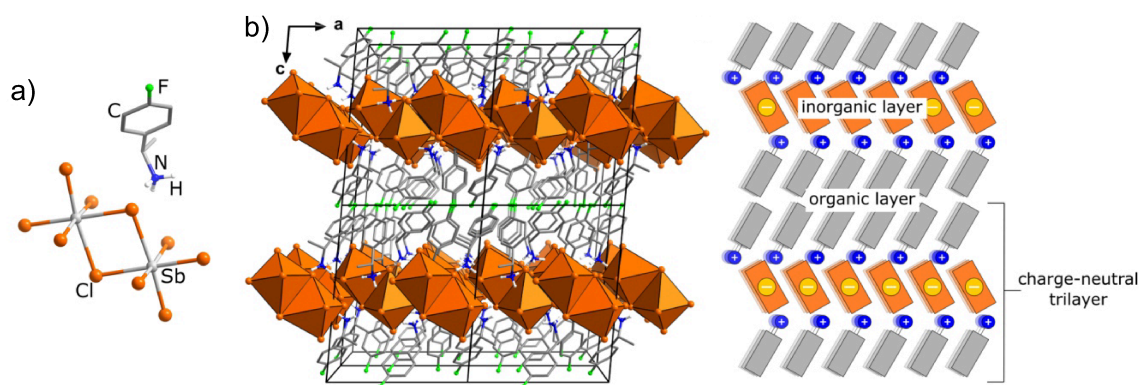

Fig. 3.9: Structure for the material class of chiral hybrid metal halides. a) shows the building blocks of the molecule. b) shows their crystal structure and unit cells. The sketch illustrates the layered structure enabling effective cleaving and therefore the possibility of manufacture for monolayers. Figure from **article IV**.

which stabilize the molecule consist of four [(R)-1-(4-fluoro)-phenylethylammonium]$^{+}$ units surrounding the backbone (see Fig. 3.9). This new material class is of interest due to multiple reasons: Firstly, they are, as the name suggests, inherently chiral which makes them suitable candidates for spintronics [90] or spinfilter applications. Secondly, their crystal structure consists of Van der Waals-coupled neutral trilayers, enabling effective cleavage and therefore facilitating the manufacturing of 2D layers. And lastly, the different combination possibilities for the halogenido pentelates allow tuning of the bandgap and therefore the onset of absorption in an energy range from 2.09 eV up to 3.35 eV (Fig. 3.10).

Since these are novel materials, we contributed in a first step some exploratory SH measurements, where we tested the materials for crystallinity as well as stability in ambient conditions under irradiation by 800 nm-light. Second-harmonic is well suited for the study of these materials, since they belong to the monoclinic space group P2$_1$ (non-centrosymmetric) resulting in a large SH signal. Considering that our second-harmonic imaging microscope allows for large-scale polarization dependent measurements, we were able to measure $400 \times 400 \, \mu m^2$ areas of the samples to
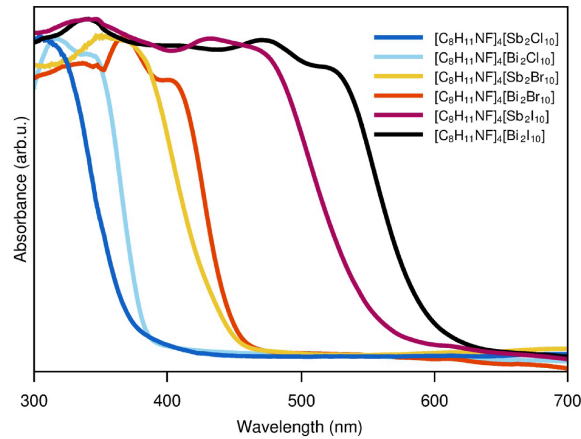
Fig. 3.10: UV-vis spectra of the different compounds. Colors correspond to the respective materials. Figure from **article IV**.
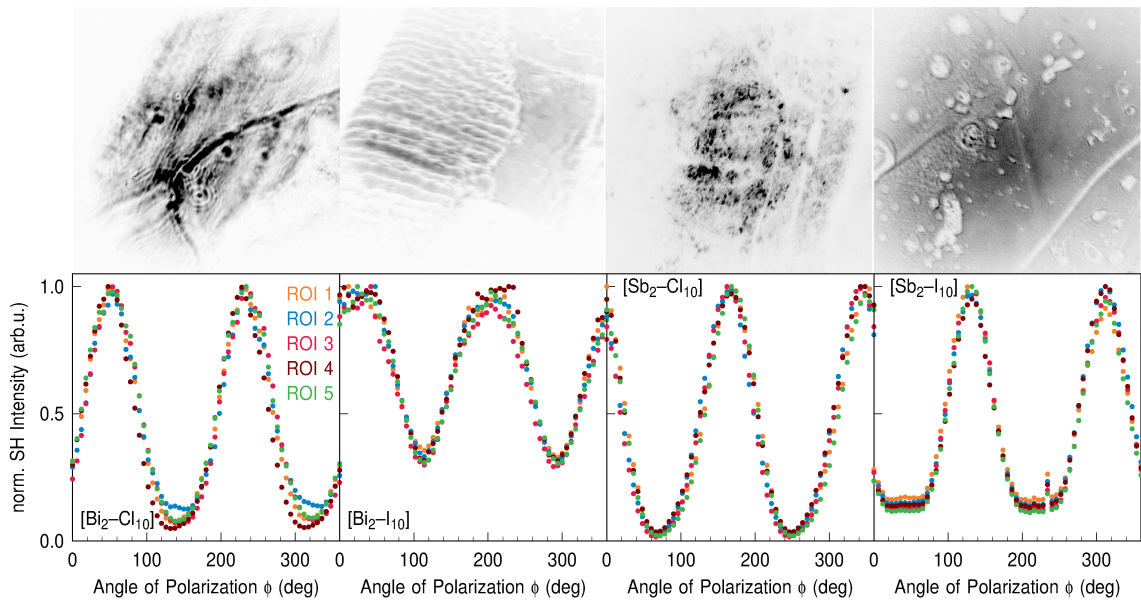

Fig. 3.11: Polarization resolved SHG measurements performed on four compounds. In the upper row are the intensity inverted SH images for the individual samples depicted. In the lower row polarization dependent SH measurements performed on the samples are illustrated. The shown ROIs were arbitrarily chosen to determine homogeneity of the sample.

test for structural changes. Some images from those measurements are shown in the upper row of Fig. 3.11. There is a clear surface roughness visible on the macroscopic scale for all samples. However, on the microscopic scale no large deviation or change in anisotropy was visible for any of the measured samples in the polarization dependent measurements (see Fig. 3.11, lower row). This substantiates the quality of the grown crystals and their large scale crystal homogeneity. All samples showed no signs of degradation under prolonged 800 nm radiation at approximately $120\,\mu J/cm^2$, with the exception being $[Bi_2I_{10}]$. Closer examination of the second-harmonic images
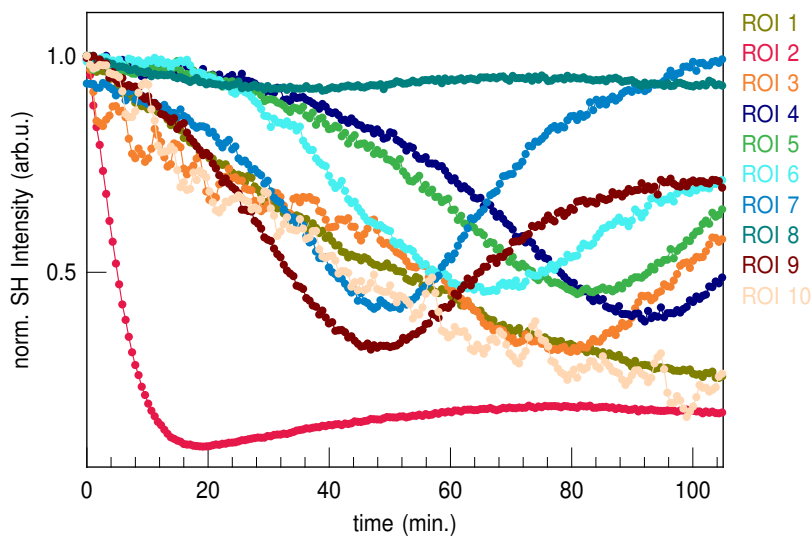
Fig. 3.12: Time-dependent SH intensity measurement to determine irradiation damage in $[Bi_2I_{10}]$. Here the SH intensity generated by $[Bi_2I_{10}]$ is plotted against exposure time. The ROIs were randomly placed over the whole sample area. The whole sample was irradiated with 1.55 eV laserlight with an approximate fluence of $120\,\mu J/cm^2$. There is a clear reduction of the intensity visible for all curves, while some show an oscillatory behaviour.

during tuning revealed ripples running across the surface of the sample. Following this observation we monitored the intensity under irradiation over an extended time period. The result is shown in Fig. 3.12. The traces reveal an oscillation of the second-harmonic intensity, which indicates some surface level damage of the sample, which is possibly caused by a cyclic photo-reaction.

To further quantify the physical properties of the compounds, qualitative measurements were performed to determine the efficiency of the second-harmonic generation as well as verify the $P2_1$ space-group of the samples in a transmission SH setup. All samples show the expected quadratic power dependence of the signal on the applied laser power as seen in Fig. 3.13(a). Rotational anisotropy measurements were performed by revolving the samples around the c-axis of the crystals. The strongest SH response is observed for s-polarized incoming fundamental and parallel s-polarized detection for 0° azimuth angle. Of the six investigated samples four agree well with the expected monoclinic space group, as seen by the fit in 3.13(a). The $[Sb_2I_{10}]$ and $[Bi_2I_{10}]$ compounds, however, deviate considerably from the expected anisotropies. While the cause can not be pinpointed exactly, possible explanations would be inhomogeneity in the case of $[Sb_2I_{10}]$ and the observed instability under 800 nm irradiation of compound $[Bi_2I_{10}]$. Therefore systematic study of the SH response was impossible for said samples.

Fig. 3.13(b) shows not only the quadratic dependence, but also allows for direct comparison of the SH efficiency of the remaining four compounds in relation to a quartz crystal (α-SiO$_2$) reference. In correlation with the measured SHG by the
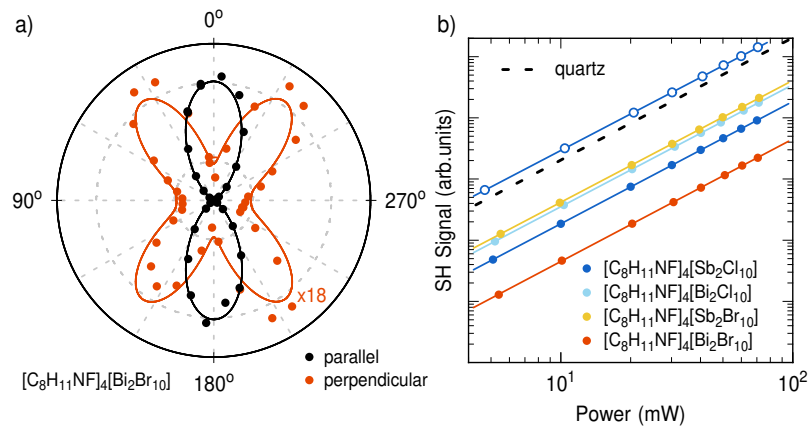
Fig. 3.13: Rotation anisotropy measurement for $[Bi_2Br_{10}]$ and power-dependent measurements for all compounds. a) shows rotational anisotropy measurements for the $[Bi_2Br_{10}]$ sample for two outgoing polarization components. The black (orange) datapoints correspond to a detected polarization parallel (perpendicular) to the incoming s-polarized fundamental. The line is a fit to the data. The graph in b) depicts the dependency of the generated second-harmonic intensity on the applied power. The double logarithmic plot reveals the expected squared behavior of the second-harmonic. The closed circles represent thin samples of the individual materials, the open circles a thicker sample of $[Sb_2Cl_{10}]$. The dashed line shows the response of a quartz crystal for comparison. Figure from **article IV**.

quartz crystal it can be seen, that the efficiency of this new material class is on a comparable level.

Overall **article IV** successfully introduced the new material class of chiral hybrid metal halides. There are still lots of research opportunities present in the form of further quantification and study of the characteristics for chiral hybrid metal halides. However as an intermediate result we find that the nonlinear attributes of these compounds are on a comparable level with quartz, which identifies them as possible candidates for application in nonlinear optics. This in unison with their inherent chirality makes them interesting aspirants as new building blocks in ever-growing family of two-dimensional materials.

Bibliography

[1] B. Lojek, *History of Semiconductor Engineering* (Springer, Berlin, 2006).

[2] IBM Unveils World's First 2 Nanometer Chip Technology, Opening a New Frontier for Semiconductors, https://newsroom.ibm.com/2021-05-06-IBM-Unveils-Worlds-First-2-Nanometer-Chip-Technology,-Opening-a-New-Frontier-for-Semiconductors#assets_all,

[3] J. M. Gottfried and U. Höfer, *Preface: Fresh Perspectives on Internal Interfaces*, Journal of Physics: Condensed Matter **31**, 500301 (Sep 2019).

[4] T. Kirchartz, J. Bisquert, I. Mora-Sero, and G. Garcia-Belmonte, *Classification of Solar Cells According to Mechanisms of Charge Separation and Charge Collection*, Phys. Chem. Chem. Phys. **17**, 4007 (2015).

[5] B. Radisavljevic, A. Radenovic, J. Brivio, V. Giacometti, and A. Kis, *Single-Layer MoS$_2$ Transistors*, Nat. Nanotechnol. **6**, 147 (2011).

[6] Y. R. Shen, *The Principles of Nonlinear Optics* (Wiley, New York, 1984).

[7] G. A. Reider and T. F. Heinz, in *Photonic Probes of Surfaces*, edited by P. Halevi (Elsevier Science B.V., Amsterdam, 1995), pp. 415–70.

[8] M. B. Raschke and Y. R. Shen, *Nonlinear Optical Spectroscopy of Solid Interfaces*, Curr. Opin. Solid St. M. **8**, 343 (2004).

[9] K. S. Novoselov, A. K. Geim, S. V. Morozov, D. Jiang, Y. Zhang, S. V. Dubonos, I. V. Grigorieva, and A. A. Firsov, *Electric Field Effect in Atomically Thin Carbon Films*, Science **306**, 666 (2004).

[10] K. F. Mak, C. Lee, J. Hone, J. Shan, and T. F. Heinz, *Atomically Thin MoS$_2$: A New Direct-Gap Semiconductor*, Phys. Rev. Lett. **105**, 136805 (2010).

[11] A. Splendiani, L. Sun, Y. Zhang, T. Li, J. Kim, C.-Y. Chim, G. Galli, and F. Wang, *Emerging Photoluminescence in Monolayer MoS$_2$*, Nano Lett. **10**, 1271 (2010).

[12] N. Kumar, S. Najmaei, Q. Cui, F. Ceballos, P. M. Ajayan, J. Lou, and H. Zhao, *Second Harmonic Microscopy of Monolayer MoS$_2$*, Phys. Rev. B **87**, 161403 (2013).

[13] L. M. Malard, T. V. Alencar, A. P. M. Barboza, K. F. Mak, and A. M. de Paula, *Observation of Intense Second Harmonic Generation from MoS$_2$ Atomic Crystals*, Phys. Rev. B **87**, 201401 (2013).

[14] L. F. Mattheiss, *Band Structures of Transition-Metal-Dichalcogenide Layer Compounds*, Phys. Rev. B **8**, 3719 (Oct 1973).

[15] G. B. Liu, W. Y. Shan, Y. G. Yao, W. Yao, and D. Xiao, *Three-Band Tight-Binding Model for Monolayers of Group-VIB Transition Metal Dichalcogenides*, Phys. Rev. B **88**, 085433 (2013).

[16] A. Chernikov, T. C. Berkelbach, H. M. Hill, A. Rigosi, Y. Li, O. B. Aslan, D. R. Reichman, M. S. Hybertsen, and T. F. Heinz, *Exciton Binding Energy and Nonhydrogenic Rydberg Series in Monolayer WS$_2$*, Phy. Rev. Lett. **113**, 076802 (2014).

[17] V. O. Özcelik, J. G. Azadani, C. Yang, S. J. Koester, and T. Low, *Band Alignment of Two-Dimensional Semiconductors for Designing Heterostructures with Momentum Space Matching*, Phys. Rev. B **94**, 035125 (2016).

[18] Z. Wang, P. Altmann, C. Gadermaier, Y. Yang, W. Li, L. Ghirardini, C. Trovatello, M. Finazzi, L. Duò, M. Celebrano, R. Long, D. Akinwande, O. V. Prezhdo, G. Cerullo, and C. S. Dal, *Phonon-Mediated Interlayer Charge Separation and Recombination in a MoSe$_2$/WSe$_2$ Heterostructure*, Nano Letters **21**, 2165 (2021).

[19] S.-W. Zheng, H.-Y. Wang, L. Wang, H. Wang, and H.-B. Sun, *Layer-Dependent Electron Transfer and Recombination Processes in MoS$_2$/WSe$_2$ Multilayer Heterostructures*, The Journal of Physical Chemistry Letters **11**, 9649 (2020).

[20] J. E. Zimmermann, Y. D. Kim, J. C. Hone., U. Höfer, and G. Mette, *Directional Dltrafast Charge Transfer in a WSe$_2$/MoSe$_2$ Heterostructure Selectively Probed by Time-Resolved SHG Imaging Microscopy*, Nanoscale Horiz. **5**, 1603 (2020).

[21] E. V. Calman, L. H. Fowler-Gerace, D. J. Choksy, L. V. Butov, D. E. Nikonov, I. A. Young, S. Hu, A. Mishchenko, and A. K. Geim, *Indirect Excitons and Trions in MoSe$_2$/WSe$_2$ Van Der Waals Heterostructures*, Nano Lett. **20**, 1869 (2020).

[22] S. Ovesen, S. Brem, C. Linderalv, M. Kuisma, T. Korn, P. Erhart, M. Selig, and E. Malic, *Interlayer Exciton Dynamics in Van Der Waals Heterostructures*, Commun. Phys. **2**, 23 (2019).

[23] J. Kunstmann, F. Mooshammer, P. Nagler, A. Chaves, F. Stein, N. Paradiso, G. Plechinger, C. Strunk, C. Schüller, G. Seifert, D. R. Reichman, and T. Korn, *Momentum-Space Indirect Interlayer Excitons in Transition-Metal Dichalcogenide Van Der Waals Heterostructures*, Nat. Phys. **14**, 801 (2018).

[24] P. Rivera, H. Yu, K. L. Seyler, N. P. Wilson, W. Yao, and X. Xu, *Interlayer Valley Excitons in Heterobilayers of Transition Metal Dichalcogenides*, Nat. Nanotechnol. **13**, 1004 (2018).

[25] B. Miller, A. Steinhoff, B. Pano, J. Klein, F. Jahnke, A. Holleitner, and U. Wurstbauer, *Long-Lived Direct and Indirect Interlayer Excitons in Van Der Waals Heterostructures*, Nano Lett. **17**, 5229 (2017).

[26] J. R. Schaibley, P. Rivera, H. Y. Yu, K. L. Seyler, J. Q. Yan, D. G. Mandrus, T. Taniguchi, K. Watanabe, W. Yao, and X. D. Xu, *Directional Interlayer Spin-Valley Transfer in Two-Dimensional Heterostructures*, Nat. Commun. **7**, 13747 (2016).

[27] P. Rivera, J. R. Schaibley, A. M. Jones, J. S. Ross, S. F. Wu, G. Aivazian, P. Klement, K. Seyler, G. Clark, N. J. Ghimire, J. Q. Yan, D. G. Mandrus, W. Yao, and X. D. Xu, *Observation of Long-Lived Interlayer Excitons in Monolayer $MoSe_2$-WSe_2 Heterostructures*, Nat. Commun. **6**, 6242 (2015).

[28] H. Fang, C. Battaglia, C. Carraro, S. Nemsak, B. Ozdol, J. S. Kang, H. A. Bechtel, S. B. Desai, F. Kronast, A. A. Unal, G. Conti, C. Conlon, G. K. Palsson, M. C. Martin, A. M. Minor, C. S. Fadley, E. Yablonovitch, R. Maboudian, and A. Javey, *Strong Interlayer Coupling in Van Der Waals Heterostructures Built from Single-Layer Chalcogenides*, P. Natl. Acad. Sci. USA **111**, 6198 (2014).

[29] X. P. Hong, J. Kim, S. F. Shi, Y. Zhang, C. H. Jin, Y. H. Sun, S. Tongay, J. Q. Wu, Y. F. Zhang, and F. Wang, *Ultrafast Charge Transfer in Atomically Thin MoS_2/WS_2 Heterostructures*, Nat. Nanotechnol. **9**, 682 (2014).

[30] F. Ceballos, M. Z. Bellus, H. Y. Chiu, and H. Zhao, *Ultrafast Charge Separation and Indirect Exciton Formation in a MoS_2-$MoSe_2$ Van Der Waals Heterostructure*, ACS Nano **8**, 12717 (2014).

[31] F. Ceballos, M. Z. Bellus, H. Y. Chiu, and H. Zhao, *Probing Charge Transfer Excitons in a $MoSe_2$-WS_2 Van Der Waals Heterostructure*, Nanoscale **7**, 17523 (2015).

[32] B. Peng, G. N. Yu, X. F. Liu, B. Liu, X. Liang, L. Bi, L. J. Deng, T. C. Sum, and K. P. Loh, *Ultrafast Charge Transfer in MoS_2/WSe_2 P-N Heterojunction*, 2D Mater. **3**, 025020 (2016).

[33] M. Baranowski, A. Surrente, L. Klopotowski, J. M. Urban, N. Zhang, D. K. Maude, K. Wiwatowski, S. Mackowski, Y. C. Kung, D. Dumcenco, A. Kis, and P. Plochocka, *Probing the Interlayer Exciton Physics in a $MoS_2/MoSe_2/MoS_2$ Van Der Waals Heterostructure*, Nano Lett. **17**, 6360 (2017).

[34] D. Yang, S. J. Sandoval, W. M. R. Divigalpitiya, J. C. Irwin, and R. F. Frindt, *Structure of Single-Molecular-Layer* MoS_2, Phys. Rev. B **43**, 12053 (1991).

[35] *Solid Lubricants and Self-Lubricating Solids*, edited by F. J. Clauss (Academic Press, Boston, 1972), pp. xi–xii.

[36] W. Choi, N. Choudhary, G. H. Han, J. Park, D. Akinwande, and Y. H. Lee, *Recent Development of Two-Dimensional Transition Metal Dichalcogenides and Their Applications*, Materials Today **20**, 116 (2017).

[37] T. Akama, W. Okita, R. Nagai, C. Li, T. Kaneko, and T. Kato, *Schottky Solar Cell Using Few-Layered Transition Metal Dichalcogenides Toward Large-Scale Fabrication of Semitransparent and Flexible Power Generator*, Sci. Rep. **7**, 11967 (2017).

[38] B. Radisavljevic and A. Kis, *Mobility Engineering and a Metal-Insulator Transition in Monolayer MoS_2*, Nat. Mater. **12**, 815 (2013).

[39] N. Choudhary, M. Patel, Y.-H. Ho, N. B. Dahotre, W. Lee, J. Y. Hwang, and W. Choi, *Directly Deposited MoS_2 Thin Film Electrodes for High Performance Supercapacitors*, J. Mater. Chem. A **3**, 24049 (2015).

[40] T. Woźniak, P. E. Faria Junior, G. Seifert, A. Chaves, and J. Kunstmann, *Exciton g Factors of Van Der Waals Heterostructures from First-Principles Calculations*, Phys. Rev. B **101**, 235408 (Jun 2020).

[41] X. D. Xu, W. Yao, D. Xiao, and T. F. Heinz, *Spin and Pseudospins in Layered Transition Metal Dichalcogenides*, Nat. Phys. **10**, 343 (2014).

[42] E. Malic, M. Selig, M. Feierabend, S. Brem, D. Christiansen, F. Wendler, A. Knorr, and G. Berghäuser, *Dark Excitons in Transition Metal Dichalcogenides*, Phys. Rev. Materials **2**, 014002 (2018).

[43] R. Wallauer, R. Perea-Causin, L. Münster, S. Zajusch, S. Brem, J. Güdde, K. Tanimura, K. Lin, R. Huber, E. Malic, and H. U., *Momentum-Resolved Observation of Exciton Formation Dynamics in Monolayer WS_2*, Nano Letters **XXXX**, XXX (2021).

[44] M. Brotons-Gisbert, H. Baek, A. Molina-Sánchez, A. Campbell, E. Scerri, D. White, K. Watanabe, T. Taniguchi, C. Bonato, and B. D. Gerardot, *Spin–Layer*

Locking of Interlayer Excitons Trapped in Moiré Potentials, Nat. Materials **19**, 630 (2020).

[45] M. R. Rosenberger, H.-J. Chuang, M. Phillips, V. P. Oleshko, K. M. McCreary, S. V. Sivaram, C. S. Hellberg, and B. T. Jonker, *Twist Angle-Dependent Atomic Reconstruction and Moiré Patterns in Transition Metal Dichalcogenide Heterostructures*, ACS Nano **14**, 4550 (2020).

[46] L. Yuan, B. Y. Zheng, J. Kunstmann, T. Brumme, A. B. Kuc, C. Ma, S. B. Deng, D. Blach, A. L. Pan, and L. B. Huang, *Twist-Angle-Dependent Interlayer Exciton Diffusion in WS$_2$-WSe$_2$ Heterobilayers*, Nat. Mater. **19**, 617 (2020).

[47] L. Zhang, Z. Zhang, F. Wu, D. Wang, R. Gogna, S. Hou, K. Watanabe, T. Taniguchi, K. Kulkarni, T. Kuo, S. R. Forrest, and H. Deng, *Twist-Angle Dependence of Moiré Excitons in WS$_2$/MoSe$_2$ Heterobilayers*, ACS Nano **11**, 5888 (2020).

[48] P. Merkl, F. Mooshammer, P. Steinleitner, A. Girnghuber, K. Q. Lin, P. Nagler, J. Holler, C. Schüller, J. M. Lupton, T. Korn, S. Ovesen, S. Brem, E. Malic, and R. Huber, *Ultrafast Transition between Exciton Phases in Van Der Waals Heterostructures*, Nat. Mater. **18**, 691 (2019).

[49] H. M. Zhu, J. Wang, Z. Z. Gong, Y. D. Kim, J. Hone, and X. Y. Zhu, *Interfacial Charge Transfer Circumventing Momentum Mismatch at Two-Dimensional Van Der Waals Heterojunctions*, Nano Lett. **17**, 3591 (2017).

[50] H. Z. Zhou, Y. D. Zhao, W. J. Tao, Y. J. Li, Q. H. Zhou, and H. M. Zhu, *Controlling Exciton and Valley Dynamics in Two-Dimensional Heterostructures with Atomically Precise Interlayer Proximity*, ACS Nano **14**, 4618 (2020).

[51] J. Shi, Y. Z. Li, Z. P. Zhang, W. Q. Feng, Q. Wang, S. L. Ren, J. Zhang, W. N. Du, X. X. Wu, X. Y. Sui, Y. Mi, R. Wang, Y. H. Sun, L. J. Zhang, X. H. Qiu, J. Lu, C. Shen, Y. F. Zhang, Q. Zhang, and X. F. Liu, *Twisted-Angle-Dependent Optical Behaviors of Intralayer Excitons and Trions in WS$_2$/WSe$_2$ Heterostructure*, ACS Photonics **6**, 3082 (2019).

[52] Y. Yu, Z. Y. Wang, J. L. Wei, W. Y. Zhao, X. Lin, Z. M. Jin, W. M. Liu, and G. H. Ma, *Ultrafast Formation and Dynamics of Interlayer Exciton in a Large-Area CVD-Grown WS$_2$/WSe$_2$ Heterostructure*, J. Phys.-Condens. Mat. **30**, 495701 (2018).

[53] R. W. Boyd, *Nonlinear Optics*, 1 ed. (Academic Press, Boston, 1992).

[54] T. F. Heinz, in *Nonlinear Surface Electromagnetic Phenomena*, edited by H.-E. Ponath and G. I. Stegeman (Elsevier Science Publishers B.V., Amsterdam, 1991), pp. 353–416.

[55] K. Klass, G. Mette, J. Güdde, M. Dürr, and U. Höfer, *Second-Harmonic Microscopy for Fluence-Dependent Investigation of Laser-Induced Surface Reactions*, Phys. Rev. B **83**, 125116 (2011).

[56] P. K. Nayak, Y. Horbatenko, S. Ahn, G. Kim, J. U. Lee, K. Y. Ma, A. R. Jang, H. Lim, D. Kim, S. Ryu, H. Cheong, N. Park, and H. S. Shin, *Probing Evolution of Twist-Angle-Dependent Interlayer Excitons in $MoSe_2/WSe_2$ Van Der Waals Heterostructures*, ACS Nano **11**, 4041 (2017).

[57] A. T. Hanbicki, H. J. Chuang, M. R. Rosenberger, C. S. Hellberg, S. V. Sivaram, K. M. McCreary, I. Mazin, and B. T. Jonker, *Double Indirect Interlayer Exciton in a $MoSe_2/WSe_2$ Van Der Waals Heterostructure*, ACS Nano **12**, 4719 (2018).

[58] F. Ceballos, Q. Cui, M. Z. Bellus, and H. Zhao, *Exciton Formation in Monolayer Transition Metal Dichalcogenides*, Nanoscale **8**, 11681 (2016).

[59] A. F. Rigosi, H. M. Hill, Y. Li, A. Chernikov, and T. F. Heinz, *Probing Interlayer Interactions in Transition Metal Dichalcogenide Heterostructures by Optical Spectroscopy: MoS_2/WS_2 and $MoSe_2/WSe_2$*, Nano Lett. **15**, 5033–38 (2015).

[60] D. Kozawa, R. Kumar, A. Carvalho, K. K. Amara, W. J. Zhao, S. F. Wang, M. L. Toh, R. M. Ribeiro, A. H. C. Neto, K. Matsuda, and G. Eda, *Photocarrier Relaxation Pathway in Two-Dimensional Semiconducting Transition Metal Dichalcogenides*, Nat. Commun. **5**, 4543 (2014).

[61] Y. M. You, X. X. Zhang, T. C. Berkelbach, M. S. Hybertsen, D. R. Reichman, and T. F. Heinz, *Observation of Biexcitons in Monolayer WSe_2*, Nat. Phys. **11**, 477 (2015).

[62] D. Z. Sun, Y. Rao, G. A. Reider, G. G. Chen, Y. M. You, L. Brezin, A. R. Harutyunyan, and T. F. Heinz, *Observation of Rapid Exciton-Exciton Annihilation in Monolayer Molybdenum Disulfide*, Nano Lett. **14**, 5625 (2014).

[63] H. Shi, R. Yan, S. Bertolazzi, J. Brivio, B. Gao, A. Kis, D. Jena, H. G. Xing, and L. B. Huang, *Exciton Dynamics in Suspended Monolayer and Few-Layer MoS_2 2D Crystals*, ACS Nano **7**, 1072 (2013).

[64] H. N. Wang, C. J. Zhang, and F. Rana, *Ultrafast Dynamics of Defect-Assisted Electron Hole Recombination in Monolayer MoS_2*, Nano Lett. **15**, 339 (2015).

[65] E. M. Mannebach, K.-A. N. Duerloo, L. A. Pellouchoud, M.-J. Sher, S. Nah, Y.-H. Kuo, Y. Yu, A. F. Marshall, L. Cao, E. J. Reed, and A. M. Lindenberg, *Ultrafast Electronic and Structural Response of Monolayer MoS_2 under Intense Photoexcitation Conditions*, ACS Nano **8**, 10734 (2014).

[66] R. Wang, B. A. Ruzicka, N. Kumar, M. Z. Bellus, H. Y. Chiu, and H. Zhao, *Ultrafast and Spatially Resolved Studies of Charge Carriers in Atomically Thin Molybdenum Disulfide*, Phys. Rev. B **86**, 045406 (2012).

[67] M. Seo, H. Yamaguchi, A. D. Mohite, S. Boubanga-Tombet, J. C. Blancon, S. Najmaei, P. M. Ajayan, J. Lou, A. J. Taylor, and R. P. Prasankumar, *Ultrafast Optical Microscopy of Single Monolayer Molybdenum Disulfide Flakes*, Sci. Rep. **6**, 21601 (2016).

[68] T. Korn, S. Heydrich, M. Hirmer, J. Schmutzler, and C. Schüller, *Low-Temperature Photocarrier Dynamics in Monolayer MoS_2*, Appl. Phys. Lett. **99**, 102109 (2011).

[69] Q. S. Wang, S. F. Ge, X. Li, J. Qiu, Y. X. Ji, J. Feng, and D. Sun, *Valley Carrier Dynamics in Monolayer Molybdenum Disulfide from Helicity-Resolved Ultrafast Pump-Probe Spectroscopy*, ACS Nano **7**, 11087 (2013).

[70] S. Cha, J. H. Sung, S. Sim, J. Park, H. Heo, M. H. Jo, and H. Choi, *1s-Intraexcitonic Dynamics in Monolayer MoS_2 Probed by Ultrafast Mid-Infrared Spectroscopy*, Nat. Commun. **7**, 10768 (2016).

[71] T. Goswami, R. Rani, K. S. Hazra, and H. N. Ghosh, *Ultrafast Carrier Dynamics of the Exciton and Trion in MoS_2 Monolayers Followed by Dissociation Dynamics in $Au@MoS_2$ 2d Heterointerfaces*, J. Phys. Chem. Lett. **10**, 3057 (2019).

[72] H. N. Wang, C. J. Zhang, and F. Rana, *Surface Recombination Limited Lifetimes of Photoexcited Carriers in Few-Layer Transition Metal Dichalcogenide MoS_2*, Nano Lett. **15**, 8204 (2015).

[73] J. G. He, K. Hummer, and C. Franchini, *Stacking Effects on the Electronic and Optical Properties of Bilayer Transition Metal Dichalcogenides MoS_2, $MoSe_2$, WS_2, and WSe_2*, Phys. Rev. B **89**, 075409 (2014).

[74] Y. Wang, Z. Wang, W. Yao, G. B. Liu, and H. Y. Yu, *Interlayer Coupling in Commensurate and Incommensurate Bilayer Structures of Transition-Metal Dichalcogenides*, Phys. Rev. B **95**, 115429 (2017).

[75] Y. Ou, Z. Kang, Q. Liao, S. Gao, Z. Zhang, and Y. Zhang, *Point Defect Induced Intervalley Scattering for the Enhancement of Interlayer Electron Transport in Bilayer MoS_2 Homojunctions*, Nanoscale **12**, 9859 (2020).

[76] J. Gao, B. C. Li, J. W. Tan, P. Chow, T. M. Lu, and N. Koratkar, *Aging of Transition Metal Dichalcogenide Monolayers*, ACS Nano **10**, 2628 (2016).

[77] G. Mirabelli, C. McGeough, M. Schmidt, E. K. McCarthy, S. Monaghan, I. M. Povey, M. McCarthy, F. Gity, R. Nagle, G. Hughes, A. Cafolla, P. K. Hurley, and R. Duffy, *Air Sensitivity of MoS$_2$, MoSe$_2$, MoTe$_2$, HfS$_2$, and HfSe$_2$*, Journal of Applied Physics **120**, 125102 (2016).

[78] G. H. Lee, X. Cui, Y. D. Kim, G. Arefe, X. Zhang, C. H. Lee, F. Ye, K. Watanabe, T. Taniguchi, P. Kim, and J. Hone, *Highly Stable, Dual-Gated MoS$_2$ Transistors Encapsulated by Hexagonal Boron Nitride with Gate-Controllable Contact, Resistance, and Threshold Voltage*, ACS Nano **9**, 7019 (2015).

[79] Q. J. Zheng, W. A. Saidi, Y. Xie, Z. G. Lan, O. V. Prezhdo, H. Petek, and J. Zhao, *Phonon-Assisted Ultrafast Charge Transfer at Van Der Waals Heterostructure Interface*, Nano Lett. **17**, 6435 (2017).

[80] Q. J. Zheng, Y. Xie, Z. G. Lan, O. V. Prezhdo, W. A. Saidi, and J. Zhao, *Phonon-Coupled Ultrafast Interlayer Charge Oscillation at Van Der Waals Heterostructure Interfaces*, Phys. Rev. B **97**, 205417 (2018).

[81] R. Wallauer, P. Marauhn, J. Reimann, S. Zoerb, F. Kraus, J. Güdde, M. Rohlfing, and U. Höfer, *Momentum-Resolved Observation of Ultrafast Interlayer Charge Transfer Between the Topmost Layers of MoS$_2$*, Phys. Rev. B **102**, 125417 (2020).

[82] Y. L. Li, A. Chernikov, X. Zhang, A. Rigosi, H. M. Hill, A. M. van der Zande, D. A. Chenet, E. M. Shih, J. Hone, and T. F. Heinz, *Measurement of the Optical Dielectric Function of Monolayer Transition-Metal Dichalcogenides: MoS$_2$, MoSe$_2$, WS$_2$, and WSe$_2$*, Phys. Rev. B **90**, 205422 (2014).

[83] O. Karni, E. Barré, S. C. Lau, R. Gillen, E. Y. Ma, B. Kim, K. Watanabe, T. Taniguchi, J. Maultzsch, K. Barmak, R. H. Page, and T. F. Heinz, *Infrared Interlayer Exciton Emission in MoS$_2$/WSe$_2$ Heterostructures*, Phys. Rev. Lett. **123**, 247402 (2019).

[84] P. Merkl, F. Mooshammer, S. Brem, A. Girnghuber, K.-Q. Lin, L. Weigl, M. Liebich, C.-K. Yong, R. Gillen, J. Maultzsch, J. M. Lupton, E. Malic, and R. Huber, *Twist-Tailoring Coulomb Correlations in Van Der Waals Homobilayers*, Nat. Commun. **11**, 2167 (2020).

[85] H. Wang, J. Bang, Y. Sun, L. Liang, D. West, V. Meunier, and S. Zhang, *The Role of Collective Motion in the Ultrafast Charge Transfer in Van Der Waals Heterostructures*, Nat. Commun. **7**, 11504 (2016).

[86] H. Zeng, X. Liu, H. Zhang, and X. Cheng, *New Theoretical Insights into the Photoinduced Carrier Transfer Dynamics in WS$_2$/WSe$_2$ Van Der Waals Heterostructures*, Phys. Chem. Chem. Phys. **23**, 694 (2021).

[87] M. Selig, G. Berghäuser, M. Richter, R. Bratschitsch, A. Knorr, and E. Malic, *Dark and Bright Exciton Formation, Thermalization, and Photoluminescence in Monolayer Transition Metal Dichalcogenides*, 2D Mater. **5**, 035017 (2018).

[88] C. Poellmann, P. Steinleitner, U. Leierseder, P. Nagler, G. Plechinger, M. Porer, R. Bratschitsch, C. Schüller, T. Korn, and R. Huber, *Resonant Internal Quantum Transitions and Femtosecond Radiative Decay of Excitons in Monolayer WSe₂*, Nat. Mater. **14**, 889 (2015).

[89] A. Raja, A. Chaves, J. Yu, G. Arefe, H. M. Hill, A. F. Rigosi, T. C. Berkelbach, P. Nagler, C. Schüller, T. Korn, C. Nuckolls, J. Hone, L. E. Brus, T. F. Heinz, D. R. Reichman, and A. Chernikov, *Coulomb Engineering of the Bandgap and Excitons in Two-Dimensional Materials*, Nat. Commun. **8**, 15251 (2017).

[90] G. Long, C. Jiang, R. Sabatini, Z. Yang, M. Wei, L. N. Quan, Q. Liang, A. Rasmita, M. Askerka, G. Walters, X. Gong, J. X, X. Wen, R. Quintero-Bermudez, H. Yuan, G. Xing, X. R. Wang, D. Song, O. Voznyy, M. Zhang, S. Hoogland, W. Gao, Q. Xiong, and E. H. Sargent, *Spin Control in Reduced-Dimensional Chiral Perovskites*, Nat. Phot. **12**, 528 (2018).

List of Figures

Publications

A. Lerch, J.E. Zimmermann, A. Namgalies, K. Stallberg and U. Höfer
Two-photon photoemission spectroscopy of unoccupied electronic states at CuPc/PTCDA/Ag(1 1 1) interfaces
J. Phys.: Condens. Matter **30**, 494001 (2018)

N. Dehnhardt, M. Axt, J.E. Zimmermann, M. Yang, G. Mette and J. Heine
Band Gap-Tunable, Chiral Hybrid Metal Halides Displaying Second-Harmonic Generation
Chem. Mater. **32**, 11, 4801-4807 (2020)

G. Mette, J.E. Zimmermann, A. Lerch, K. Brixius, J. Güdde, A. Beyer, M. Dürr, K. Volz, W. Stolz, and U. Höfer
Femtosecond time-resolved nonlinear optical spectroscopy of charge transfer at the buried GaP/Si(001) interface
Appl. Phys. Lett. **117**, 081602 (2020)

J.E. Zimmermann, B. Li, J.C. Hone, U. Höfer, and G. Mette
Second-harmonic imaging microscopy for time-resolved investigations of transition metal dichalcogenides
Journal of Physics: Condensed Matter **32**, 485901 (2020)

J.E. Zimmermann, Y.D. Kim, J.C. Hone, U. Höfer, and G. Mette
Directional ultrafast charge transfer in a $WSe_2/MoSe_2$ heterostructure selectively probed by time-resolved SHG imaging microscopy
Nanoscale Horiz. **5**, 1603-1609 (2020)

J.E. Zimmermann, M. Axt, F. Mooshammer, P. Nagler, C. Schüller, T. Korn, U. Höfer, and G. Mette
Ultrafast charge-transfer dynamics in twisted MoS_2/WSe_2 heterostructures
(under review for publication in ACS Nano)

Contributions to conferences

J. Zimmermann, G. Mette und U. Höfer
A setup for time-resolved SHG-Microscopy of 2D heterostructures
DPG-Spring Meeting of the division of Condensed Matter Physics
(Regensburg, 2016, Germany)

G. Mette, A. Lerch, K. Brixius, J. Zimmermann A. Beyer, K. Volz, W. Stolz, and U. Höfer
Charge transfer dynamics at the buried GaP/Si(001) interface studied by means of time-resolved SHG
International Conference on the Formation of Semiconductor Interfaces
(Hannover, 2017, Germany)

J. Zimmermann, G. Mette und U. Höfer
Second-harmonic imaging microscopy: a newly developed experimental setup for time-resolved studies on two-dimensional heterostructures
DPG-Spring Meeting of the division of Condensed Matter Physics
(Dresden, 2017, Germany)

J. Zimmermann, G. Mette und U. Höfer
Charge-transfer across the $MoSe_2$ /WSe_2 interface studied with second-harmonic imaging microscopy
DPG-Spring Meeting of the division of Condensed Matter Physics
(Regensburg, 2019, Germany)

Wissenschaftlicher Werdegang

This page contains personal information and is therefore omitted from the public version.

Danksagung

Bevor es so richtig losgeht möchte ich mich bei allen bedanken, die mich während meiner Promotion unterstützt haben - ohne euch alle wäre das sicher nie was geworden.

An erster Stelle danke ich natürlich meinem Doktorvater Prof. Dr. Ulrich Höfer für das entgegengebrachte Vertrauen, aufgrund dessen ich die Chance erhalten habe zu promovieren. Die exzellente experimentelle Ausstattung erlaubte mir eine freie Entfaltung meiner natürlichen Neugier, wodurch die hier abgedruckten Paper entstanden sind.

Direkt als Zweitem will ich mich inständig bei Gerson Mette bedanken, ohne dein Auge für die Details, Übersicht, konstruktive Kommentare und Vorraussicht hätte ich mich mit Sicherheit verzettelt und wäre in meinem persönlichen Chaos verloren gegangen.

Ich danke Prof. Dr. Wolfgang Heimbrodt für die Erstellung des Zweitgutachtens; Prof. Dr. Florian Gebhard danke ich für die Mitarbeit in der Prüfungskomission.

Ich hatte die Ehre, die Freude und das Vergnügen mit der bunten Mischung an Menschen mit Namen Arbeitsgruppe Oberflächenphysik an meiner Seite zu promovieren. Seitdem ich 2010 meinen Bachelor hier angefangen habe, fühlte ich mich stets willkommen. Egal ob für Programmierratschläge oder intensive Diskussionen zu wissenschaftlichen Themen, irgendjemand wusste immer Rat oder gab einen entscheidenden Denkanstoß. Aber nicht nur auf professioneller Ebene, sondern besonders auch zwischenmenschlich hätte ich bestimmt nicht ohne euch alle bis heute durchgehalten. Als letzter meiner Generation an Doktoranden wäre die Liste der zu benennenden Personen für meinen Geschmack zu lang, weshalb ich hier einfach allen für die schöne Zeit danken will, die mir für immer in angenehmer Erinnerung bleiben wird. Namentlich erwähnen muss ich natürlich noch Jens Güdde, ohne dich und dein Elefantengedächtnis würden wir alle bestimmt häufger mit großen Fragezeichen im Gesicht durchs Labor stapfen. Außerdem danke ich meinen Korrekturlesern Gerson Mette, Mirjam Daum, Marleen Axt und Tim Bergmeier für ihre Hilfe und konstruktive Kritik.

Dann danke ich natürlich noch Eileen, du hast mir geholfen das Licht im Grau zu wiederzufinden.

Das Beste kommt am Schluss: Diese Arbeit ist meiner Familie gewidmet, ohne euch wilden Haufen währe ich nicht der Mensch der ich heute bin.

Article I

Second-Harmonic Imaging Microscopy for Time-Resolved Investigations of Transition Metal Dichalcogenides

J.E. Zimmermann, B. Li, J.C. Hone, U. Höfer, and G. Mette;

Second-harmonic imaging microscopy for time-resolved investigations of transition metal dichalcogenides

J E Zimmermann[1], B Li[2], J C Hone[2], U Höfer[1] and G Mette[1,3]

[1] Fachbereich Physik und Zentrum für Materialwissenschaften, Philipps-Universität, 35032 Marburg, Germany
[2] Department of Mechanical Engineering, Columbia University, New York 10027, United States of America

E-mail: gerson.mette@physik.uni-marburg.de

CrossMark

Abstract

Two-dimensional transition metal dichalcogenides (TMD) have shown promise for various applications in optoelectronics and so-called valleytronics. Their operation and performance strongly depend on the stacking of individual layers. Here, optical second-harmonic generation in imaging mode is shown to be a versatile tool for systematic time-resolved investigations of TMD monolayers and heterostructures in consideration of the material's structure. Large sample areas can be probed without the need of any mapping or scanning. By means of polarization dependent measurements, the crystalline orientation of monolayers or the stacking angles of heterostructures can be evaluated for the whole field of view. Pump-probe experiments then allow to correlate observed transient changes of the second-harmonic response with the underlying structure. The corresponding time-resolution is virtually limited by the pulse duration of the used laser. As an example, polarization dependent and time-resolved measurements on mono- and multilayer MoS_2 flakes grown on a SiO_2/ Si(001) substrate are presented.

Keywords: second-harmonic generation, pump-probe experiment, transition metal dichalcogenides, time-resolved nonlinear optical spectroscopy, second-harmonic generation imaging microscopy

S Supplementary material for this article is available online

(Some figures may appear in colour only in the online journal)

1. Introduction

Two-dimensional (2D) materials have been intensively investigated since the first successful isolation of graphene [1] and this interest has been stimulated further by the discovery of the special properties of single-layer transition metal dichalcogenides (TMD) [2, 3]. Van der Waals coupled 2D materials now span the whole range from metallic over semiconducting up to isolating materials and their combination leads to fascinating opportunities for designing stacked heterostructures

[4, 5]. Heterostructures of TMDs have shown promise for various optoelectronic applications (cf. [6] and references therein). Moreover, future applications beyond conventional optoelectronics might be based on the coupled spin and valley physics of TMD monolayers due to their broken inversion symmetry [7]. This coupling allows the excitation of specific spin carriers into a particular valley which has been demonstrated by optical pumping with circularly polarized light [8–10]. These findings pave the way for a new class of prospective devices called valleytronics.

TMD monolayer and heterostructure samples available at the moment are typically smaller than $(100\,\mu m)^2$. Further-

[3] Author to whom any correspondence should be addressed.

more, they usually exhibit considerable spatial inhomogeneity due to intrinsic defects within the layers or extrinsic inhomogeneity such as substrate roughness, interlayer bubbles or impurities. Therefore, it is particularly important to utilize appropriate imaging techniques for their exploration. Moreover, the energy alignment of TMD heterostructures [11–15] as well as interlayer charge- and energy-transfer processes [16–23] are of particular interest in fundamental and applied research. Due to the van der Waals coupling, arbitrary layer stacking is possible. Rotational misfit between two TMD monolayers of a layered structure results in a corresponding rotation of the hexagonal Brillouin zones of the two layers leading to momentum-mismatched interlayer excitations. Therefore, the stacking influences charge and energy transfer and thereby the performance of the device. It has been shown that the interlayer coupling of homo-stacked layers depends considerably on the respective stacking angles [24–27] and the same should hold for the coupling of hetero-bilayers [28–30]. Indeed, a distinct difference in the exciton recombination of coherently and randomly stacked MoS_2/WS_2 heterostructures was observed [31]. Furthermore, a strong influence of the stacking angle on the formation dynamics of interlayer excitons has been reported recently for WSe_2/WS_2 [23].

Thus, systematic studies are highly needed to investigate how structural characteristics like the stacking angle of 2D heterostructures correlate with other physical properties of the materials such as the existence and dynamics of charge transfer excitons. In this work, we demonstrate that spatially resolved optical second-harmonic generation (SHG), i.e. SHG imaging microscopy, is a powerful experimental technique to perform time-resolved studies in consideration of the material's structure. It allows studying systematically both the orientation and the charge-carrier dynamics of TMD monolayers and heterostructures with the same experimental setup. In particular, a complementary technique to analyze the stacking of the material is not needed. As an example, we report time-resolved SHG imaging microscopy studies on MoS_2 mono- and multilayer flakes grown by chemical vapor deposition (CVD) on a 285 nm $SiO_2/Si(001)$ substrate.

2. Time-resolved SHG on TMDs

Previous studies already demonstrated that second-harmonic generation is a versatile technique to investigate single- and multilayers of TMDs [32–44]. It has been shown that the SH response of the TMDs exhibits a dramatic odd–even oscillation with the number of layers consistent with the absence (presence) of inversion symmetry in odd (even) layers [32–35]. Rotational anisotropy SHG measurements probing the SH response of TMD monolayers as a function of the crystal orientation reveal the expected three-fold rotational symmetry [33–37]. This allows the determination of crystallographic orientations for single-layer flakes [33–37], domain boundaries and orientations of CVD grown monolayer structures [35, 38, 39] as well as stacking angles of twisted bilayers [40].

While all these examples represent basically static SH experiments for structural characterization of TMD materials, time-resolved SHG has been applied in particular to study the dynamics of various phenomena at surfaces and interfaces of bulk semiconductors. Its sensitivity to symmetry changes and to interface electronic states has been exploited for time-domain investigations of phase transformations [45, 46], of adsorbate reactions [47], of interface-specific electron dynamics [48–50] and to detect transient electric fields at interfaces [51–53]. Those time-resolved experiments on TMD samples have to cope with the small flake/domain size of exfoliated and CVD grown samples available at the moment. Therefore, almost all previous linear and nonlinear optical experiments were performed at normal incidence by means of microscope objectives ($\times 100$) with short working distances and probe beams focused to spot diameter of $\approx 1\ \mu$m. This kind of setup is disadvantageous for time-resolved pump-probe studies like SHG because it makes the non-collinear incidence of pump and probe beam difficult. As the pump beam also generates SH signal, this has to be differentiated from the SH response of the probe beam. Furthermore, the time-resolution is limited due to dispersion of the used optical elements. These difficulties might explain why, to the best of our knowledge, there is only one published time-resolved SHG study on TMDs. Here, the dynamical SH response of single-layer MoS_2 to intense above-bandgap photo-excitation was investigated [41].

SHG imaging microscopy combines the advantages of time-resolved SHG with an optical microscopy setup. The SH response of the sample is imaged optically magnified on a CCD chip. Similar setups have been used to study surface reactions like desorption or diffusion [54–56] as well as electric field distributions and carrier motion [57–60]. SHG imaging microscopy copes with both of the discussed challenges of time-resolved studies on TMDs. On the one hand, the SH response of pump and probe beam can be separated very easily. On the other hand, the time-resolution is virtually limited by the pulse duration of the laser system. The SH response of large sample areas ($\approx 400 \times 400\ \mu$m^2) can be probed without the need of any mapping or scanning. By means of polarization dependent measurements, the crystalline orientation of single-layer flakes and domains, or the stacking angles of heterostructures can be evaluated for the whole field of view. Pump-probe experiments at the corresponding area then allow to correlate observed transient changes of the SH response with the underlying structure. With this technique polarization- and time-resolved measurements can be performed systematically and routinely. SHG imaging microscopy is also suited to study fluence dependent phenomena [56].

3. Experimental procedure

The experiments were performed under ambient conditions using 50 fs laser pulses generated by a femtosecond Ti:sapphire laser amplifier system (Coherent RegA) operating at 800 nm with a repetition rate of 150 kHz. The main part of the amplifier output (90%) is used to pump a travelling-wave optical parametric amplifier (OPA) operating in the visible range. The output of the OPA is compressed by a pair
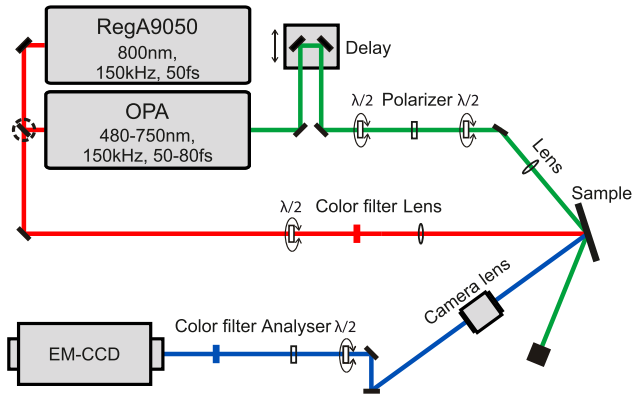
Figure 1. Experimental setup: fs-laser pulses are generated by a Ti:sapphire laser amplifier system (RegA). The main part of the amplifier output (90%) is used to pump an OPA generating visible pump pulses. The remaining part of the amplifier output is used to probe the SH response. Pump and probe beam are focussed onto the sample under an angle of 50° and 18°, respectively. The specular reflected SH light of the probe pulse is imaged optically magnified by a camera lens on the CCD camera.

of LaFN28 Brewster prisms. This visible pump beam is then focussed under the angle of 50° onto the sample as illustrated in figure 1. The remaining part of the amplifier output (10%) is focused on the sample under an angle of 18° to probe the SH response. Due to the different incident angles the SH signals generated by the pump and the probe beam are spatially separated.

The specular reflected SH response of the probe beam is imaged optically magnified by a camera lens (NIKON NIKKOR, $1 : 1.4$ ED, $f = 50$ mm) on an electron-multiplied CCD chip (PRINCETON INSTRUMENTS ProEM-HS) with a size of 1024×1024 pixels; each pixel covers an area of 13×13 μm^2 on the chip. The camera is sensitive in a spectral range from 300 nm up to 1050 nm and was operated in full image mode. The used magnification was $M \approx 35$–40, thus the visible sample region on the CCD was about 400×400 μm^2. The overall resolution of our imaging microscopy setup is better than 4 μm as determined by a standard resolution target [cf. figure S1 in the supplementary material (https://stacks.iop.org/JPCM/32/485901/mmedia)]. Thus, the resolution is close to the diffraction limit of ≈ 2 μm.

The time-delay between pump and probe beam is varied by a motorized delay stage. The polarization of pump and probe beam can be varied by means of $\lambda/2$-plates. The polarization of the second-harmonic (SH) response is analyzed by a combination of a $\lambda/2$-plate and analyzer. Color filters for separation of both the incident ω- and detected 2ω-light have been used (RG715, FBH400-40). The spot diameter of pump and probe beam on the sample (full width at half maximum) were 160 μm and 200 μm, respectively. A combination of $\lambda/2$-plate and polarizer enable the continuous variation of the incident pump fluences on the sample. The incident fluence of the 600 nm pump beam was ≈ 55 μJ cm^{-2} and ≈ 190 μJ cm^{-2} for the 800 nm probe beam. Long term measurements with these fluences applied did not exhibit any multishot damage.

The studied TMD sample consists of mono- and multilayers of MoS$_2$ flakes which were CVD grown on a 285 nm SiO$_2$/Si(001) substrate [61]. Photoluminescence (PL) measurements of the monolayer flakes exhibit an intense PL peak centered around 1.85 eV indicating low doping during the CVD process and relative low defect density compared to exfoliated MoS$_2$ as discussed in the supplementary material [62, 63]. Figures 2(a) and (b) show an optical microscope image ($\times 50$) in comparison to the respective SHG microscopy image (P-polarized SH component, $t_{\text{exposure}} = 300$ s) which is intensity-inverted for better comparability. Using a logarithmic color scale, one can differentiate easily between the triangular shaped mono- and multilayer crystals. Monolayers appear in grey color on the bright SiO$_2$/Si(001) substrate, while the multilayer flakes appear black. They exhibit an up to a factor of 30 times stronger SH response than the monolayer. This is in contrast to the reported negligible SH signals from MoS$_2$ bulk material [33] which naturally occurs in the inversion symmetric AA′ (2H) stacking. This discrepancy can be explained by an AB (3R) layer stacking which was calculated to have very similar adsorption energy in multilayer growth [64]. Thus, depending on the exact growth conditions, multilayers can grow predominantly AB stacked with the top layer zero degree aligned with the bottom layer [24]. The resulting multilayer structures are primarily non-centrosymmetric and the higher SH intensity can therefore be explained by a constructive interference of the stacked monolayer SH signals.

4. Results and discussion

4.1. Polarization dependent SHG measurements

Previous rotational anisotropy measurements probing the SH radiation component parallel (perpendicular) to the polarization of the fundamental field revealed the expected $\cos^2 3\Theta$ ($\sin^2 3\Theta$) dependence [33–38]. Here, Θ denotes the angle between the mirror plane in the crystal structure (i.e. the armchair direction) and the polarization of the probe beam. Rotating the sample then allows direct access to the symmetry of the sample and to the crystal orientation [33–38]. However, in order to exploit the advantage of SH imaging microscopy probing a larger surface area at once, the sample position is chosen to be fixed and the polarization of the fundamental is rotated as it has been previously applied on TMD monolayers [39, 41]. As it is known from literature [65] and further derived in the supplementary material, the expected dependence of P- and S-polarized components of the SH intensity on the polarization for normal incidence yield

$$\mathbf{I}_{\text{P}}^{2\omega}(\phi) \propto \cos^2(2\phi + 3\Psi) \tag{1}$$

$$\mathbf{I}_{\text{S}}^{2\omega}(\phi) \propto \sin^2(2\phi + 3\Psi). \tag{2}$$

Here, ϕ denotes the angle of the polarization with respect to the horizontal and Ψ the angle between the armchair direction of the TMD crystal and the horizontal as sketched in figure 3(b). Thus, instead of the three-fold rotational symmetry, a two-fold polarizational symmetry is expected for normal incidence.
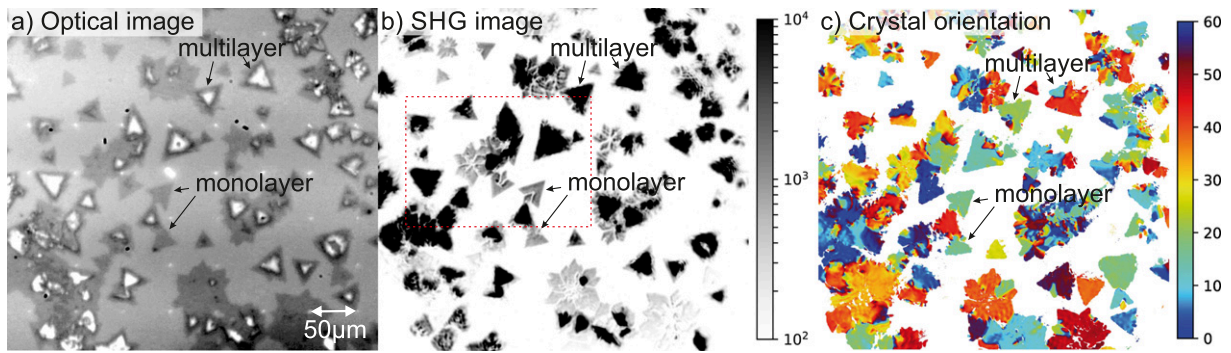
Figure 2. (a) Optical image of the CVD grown MoS_2 sample in comparison with (b) the respective intensity-inverted SH microscopy image ($400 \times 400 \ \mu m^2$). The MoS_2 mono- and multilayers are identified as triangular flakes (some marked by arrows). The multilayers exhibit an one order of magnitude stronger SH response than the monolayers. The red box marks the region used for the polarization- and time-dependent evaluations shown in figures 3 and 4. (c) Crystal angle modulo $60°$ for each individual pixel evaluated from polarization-dependent measurements. Different crystalline domains can be easily identified.

However, if the angle of incidence is $\neq 0$ like in our case, the polarization dependence of the Fresnel factors has to be considered and the equations become more complicated as derived explicitly in the supplementary material. In consequence, the two-fold symmetry is broken and the polarizational anisotropy drastically changes with increasing angle of incidence as shown in figure S4. In our case of a small angle of incidence of $18°$, the changes are comparably small, but one can clearly observe two pairs of maxima with slightly different heights in the polarization dependence shown in figure S5. The experimental data can be well described by the extended formalism to determine the crystal orientation. The polarizational anisotropy for different crystal orientations Ψ is visualized in figure S6 of the supplemental material simulating our experimental conditions. Please note, that because of the three-fold rotational symmetry of the TMD monolayers, SHG without phase information does not deduce opposite crystal orientations. Consequently, it only determines domain orientations modulo $60°$. The consistency of our evaluation has been confirmed by comparison with optical microscopy (cf. section 5 in the supplemental material). The mean value for the deviation of the extracted crystal orientations yields $0.8° \pm 0.4°$ and this accuracy probably could be further improved by longer exposure times and/or smaller angular steps. For the determination of stacking angles in TMD heterobilayers, the polarizational anisotropy of at least two regions (i.e. two monolayer regions or the heterobilayer plus one monolayer region) has to be evaluated, since the SH response from the heterobilayer represents a coherent superposition of the SH fields from the individual layers [40].

A movie of the polarization dependent SHG microscopy measurements showing the P-polarized SH component ($t_{exposure} = 60 \ s$) for varying polarization of the fundamental from $0°$ to $360°$ in steps of $3°$ can be found in the supplementary material. Figure 3 shows the corresponding polar plots of the SH intensity of (c) three mono- and (d) three multilayer regions marked in the SHG microscopy image (a). According to the derived equations, the crystal orientations Ψ of these MoS_2 mono- and multilayer flakes can be evaluated from the observed phases (3Ψ) of their polarizational anisotropy

by a corresponding fit. The crystal orientation can also be extracted for every pixel by an automatized fitting routine which is further described in the supplementary material. The result is illustrated in figure 2(c). The crystal orientation for each individual flake including overlapping domains and growth errors like twins can be easily identified. One has to point out that the determination of the crystal orientation or stacking angles by means of SHG originates directly from the symmetry properties of the TMD layers. Neither a complementary experimental technique nor further modelling is needed for the evaluation. This is in contrast to similar considerations for graphene which is, by the way, not accessible by SHG due to its inversion symmetry. Instead, the stacking of bilayer graphene has been studied systematically for example by the combination of structural and optical experimental techniques like transmission electron microscopy and Raman spectroscopy [66, 67].

4.2. Time-resolved SHG measurements

The results of a time-resolved pump-probe SHG experiment on the same surface area as in figure 3(a) are shown in figure 4. The used pump-wavelength of 600 nm (2.07 eV) was chosen to be slightly above the B-exciton resonance of MoS_2 (2.02 eV) [20] for generation of A- and B-excitons to gain access to the full domain of possible decay channels. The observed transients for both MoS_2 monolayers and multilayers show an ultrafast pump-induced decrease of the SH response and a subsequent relaxation on a picosecond timescale. The relaxation dynamics considerably differ between mono- and multilayers. The spatial resolution of SHG imaging micrococopy is particularly advantageous to monitor directly the homogeneity of the TMD monolayers and heterostructures after photoexcitation. As illustrated in figure 4(a), the individual monolayer flakes reveal a homogeneous SH response, and the same holds for the transient changes of the monolayers due to photoexcitation. Figures 4(b) and (c) display SH images at pump-probe delays of 0 ps and 12.5 ps which were normalized to an average of ten images at negative delays. While normalization improves the visibility of small pump-induced changes, it also amplifies the overall noise level. Thus, the noisy appearance
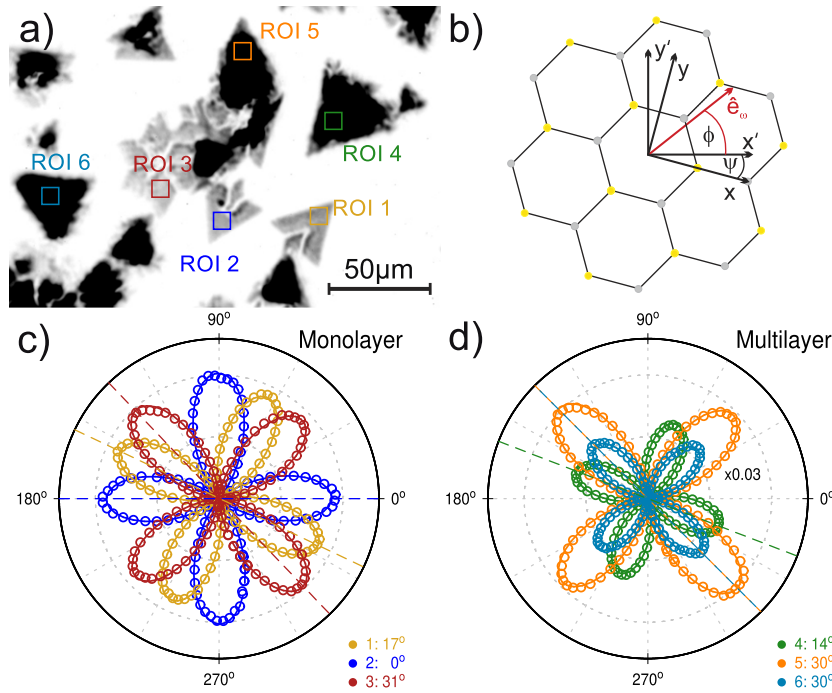
Figure 3. (a) SHG microscopy image (P-polarized SH component, $t_{exposure} = 60$ s) with colored regions of interests for which the polarizational anisotropy is evaluated in (c) and (d). (b) Schematic drawing of the experimental geometry. x', y' represent the lab coordinates and x, y the crystal coordinates. ϕ describes the angle between the polarization of the fundamental ($\hat{e}_\omega$) and the lab coordinate (x'). Ψ denotes the rotation angle of the crystal coordinates with respect to the lab coordinates. (c) and (d) Polar plots of the P-polarized component of the SH intensity of three mono- and three multilayer flakes of MoS_2 and corresponding fits (solid lines) from which the individual crystal orientations Ψ of the six regions have been extracted. Colored dashed lines visualize the orientation-dependent phases (3Ψ) of the polarizational anisotropies.

of the monolayer flakes in the normalized images is caused by their lower SH signal and not due to sample degradation. In comparison to the rather homogeneous transient changes of the monolayer flakes, the dynamics of the multilayer flakes exhibit clear inhomogeneity within the flakes such as the apparent differences for the inner and outer part of the multilayer flake at ROI 4. Appropriate regions of interest are therefore chosen to evaluate the transient change for a homogeneous area.

The different monolayer flakes (ROI 1–3, figure 4(d)) exhibit very reproducible transients with an initial pump-induced decrease of the SH signal of about 6% followed by a bi-exponential recovery. As determined from a rate-equation model the fast decaying component corresponds to an averaged time-constant of $\tau_1 = 1.9 \pm 0.7$ ps, followed by a second slow component with a time-constant of $\tau_2 = 48.5 \pm 2.1$ ps. In direct comparison, the multilayer flakes (ROI 4–6, figure 4(e)) show a slightly larger variance with regard to the initial drop ($\sim$3–6%) as well as the following dynamics. Most likely, this variance can be attributed to a certain thickness variation of individual multilayer flakes. For all multilayer transients, however, a clear mono-exponential recovery can be observed. The corresponding averaged time-constant is determined to be $\tau = 3.2 \pm 0.9$ ps.

In linear optical spectroscopy, a sub-picosecond initial decay of the transient absorption signal from TMD monolayers has been observed upon ultrafast interband excitation (3.18 eV), which was attributed to the formation of excitons from electron–hole pairs [68]. Accordingly, this fast decay is

absent, if the pump pulses are tuned to the exciton resonances, like in our case, and the excitons are directly injected [68]. Furthermore, thermalization and energy relaxation processes of non-thermal carrier distributions were reported to appear on even shorter time scales [69] and should play a minor role for resonant exciton injection. We therefore attribute the fast initial decrease of the SH response to pump-induced changes in the second-order nonlinear susceptibility, e.g., due to the pump-induced depopulation of the valence band associated with the generation of excitons. The subsequent progression is then interpreted as exciton relaxation. Please note, that no pump-induced changes have been observed for different TMD monolayers, if the pump photon energy is tuned below their A-exciton resonance (not shown). Further evidence for our attribution is given by fluence dependent measurements, which exhibit a linear increase of the initial signal change with increasing applied pump power (cf. insets of figures 4(d) and (e)) [70]. Beside this linear increase, the dynamics of the SH transients do not show any dependence on the applied pump fluence. The latter would have been expected for higher exciton densities for which exciton–exciton annihilation was shown to dominate the decay of the exciton population [71]. We therefore attribute the observed lifetimes of the SH signals as defect-mediated non-radiative recombination in accordance with previous studies on MoS_2 monolayers [72–74].

The determined time-constants of the MoS_2 monolayer compare very well with excitonic lifetimes obtained from linear optical spectroscopy [72, 73]. However, the overall number
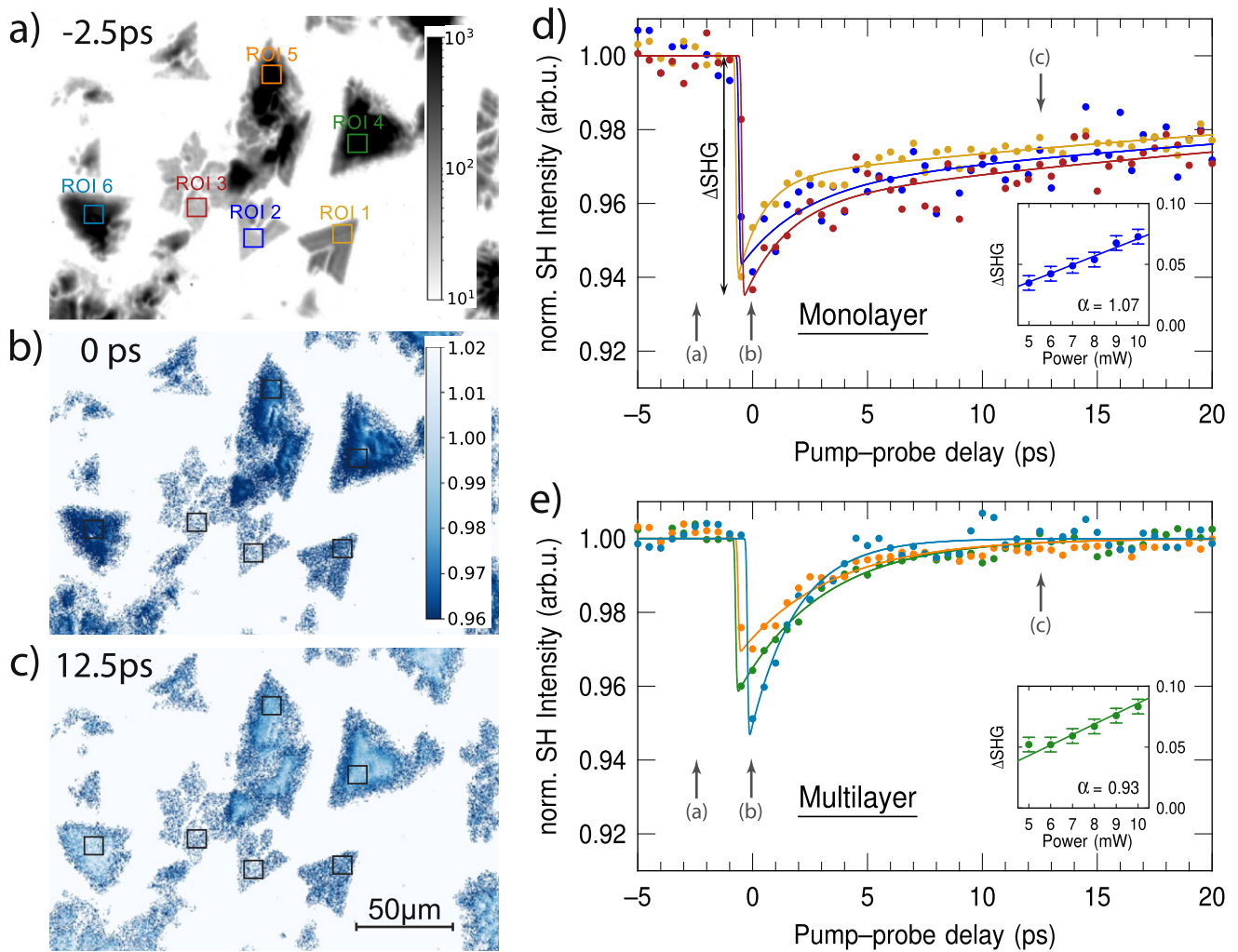
Figure 4. Time-resolved SHG from MoS$_2$ monolayer and multilayer flakes upon 600 nm excitation at an applied laser power of 10 mW ($F_{pump} = 55\ \mu$J cm^{-2}). (a) SH image of the same area as shown in figure 3 at a pump-probe delay of -2.5 ps. (b) and (c) show normalized SH images at different pump-probe delays of 0 ps and 12.5 ps, respectively. The two images are normalized to an average of ten images at negative delay times, i.e. before excitation, and therefore share the same color scale. Dark blue color represents a pump-induced decrease in intensity, light blue signifies no change. At temporal overlap (b), a clear decrease of the SH intensity is observed for all MoS$_2$ flakes. After 12.5 ps (c), the intensity of all flakes has recovered to some extent, in particular in the center of the multilayers flakes. (d) and (e) show the averaged SH intensities of the individual regions in dependence of the pump-probe delay for monolayers (ROI 1–3) and multilayers (ROI 4–6), respectively. The grey arrows mark the temporal position of the images (a), (b) and (c). The insets show the fluence dependence of the initial decrease of the SH intensity (ΔSHG) as indicated by the arrow in (d).

and values of reported time-constants for MoS$_2$ monolayers differ quite strongly [18, 41, 71–73, 75–80]. Single- [41, 76, 78], bi- [18, 71, 73, 75, 77, 79] and tri- [72, 80] exponential behavior has been reported. The value of the shortest time-constant ranges from 500 fs up to 100 ps and that of the longest time-constant from 15 ps up to 500 ps.

For the MoS$_2$ multilayer, we observe that the overall decay is clearly faster than the monolayer decay. Experimental studies comparing directly the dynamics of MoS$_2$ mono- and multilayers are rare and, furthermore, report contrary effects: Shi *et al* observed slightly smaller time-constants of few-layer systems without discussing the physical origin [72]. In contrast, Wang *et al* found a strong increase of the time-constants with increasing layer number, which was attributed to enhanced surface recombination due to larger defect density of surface

layers in multilayer samples [74]. The observed difference in the multilayer dynamics of our study and the work by Wang *et al* might be caused by the different stacking configuration (3R vs. 2H) or different defect densities due to the different preparation methods (CVD vs. exfoliation). While the former is less likely because of the very similar bandstructure of the 3R- and the 2H-configuration [3, 81], it seems reasonable that the defect density in the CVD grown multilayer is more homogeneous than for the exfoliated sample. Due to the indirect bandgap of multilayer MoS$_2$ optical excitation results in momentum indirect excitons with the electrons and holes located at the Σ- and the Γ-point, respectively [3, 81]. The bands at these points consist of hybridized states and are therefore delocalized over multiple layers, which enables effective interlayer charge transfer [82, 83]. Therefore, the fast decay of

the exciton population in the multilayer could be facilitated by vertical transport across the layers resulting in a faster trapping compared with the monolayer.

Thus, the values and trends in the dynamics of MoS_2 mono- and multilayer systems reported in literature deviate considerably from each other. While the reasons for these differences remain ambiguous, they might be explained especially by varying sample quality and among other things also by the use of different substrates, different temperatures, different pump- and probe energies and laser fluences, and of course, also by systematic effects of the applied techniques. From this lack of clarity for these quite simple 2D mono- and multilayer systems, one might anticipate the complexity for 2D heterostructures and corresponding devices. Thus, systematic time-resolved studies on monolayer and heterostructure systems are mandatory in identifying the genuine physical effects and understanding the underlying mechanisms. Consequently, this knowledge will facilitate the further development and improvement of prospective applications based on 2D materials.

Overall, SHG imaging microscopy enables such systematic investigations of μm small 2D monolayers and heterostructures on various substrates. It is universally applicable to all materials without inversion symmetry. The underlying substrate should ideally generate no SH light, but the substrate can of course strongly modify the dielectric environment of the 2D structure which will also affect the SHG intensity (cf. supplementary material). One particular advantage of our imaging microscopy over scanning techniques is the large field of view allowing the simultaneous evaluation of several flakes or spatially inhomogeneous structures. The intrinsic sensitivity of SHG to symmetry changes, electronic states or transient electric fields permits a plethora of time-resolved studies such as ultrafast charge transfer within TMD heterostructures and its correlation to the layer stacking. Especially by applying the particular strengths of polarization-resolved measurements in combination with time-resolved experiments unique opportunities arise for misaligned heterostructures. Since the signals from the individual monolayers can be isolated, the investigation of directional interlayer charge transfer becomes feasible which is not directly accessible by linear optical pump-probe techniques.

5. Conclusion

We have introduced time-resolved SHG imaging microscopy for the investigation of monolayers and heterostructures of two-dimensional transition metal dichalcogenides. For single- and multilayer MoS_2 flakes grown on $SiO_2/Si(001)$ crystalline orientations are evaluated from polarization dependent measurements. Time-resolved experiments exhibit an ultrafast pump-induced decrease of the SH response in both systems while their relaxation behavior differs considerably. From the corresponding time-constants the transient changes are attributed to the generation and relaxation of excitons. The results demonstrate that SHG imaging microscopy is a powerful method to investigate the dynamics of charge carriers

and excitons of TMD heterostructures by systematic pump-probe experiments of spatially inhomogeneous samples. The observed transient changes of the second-harmonic response can be readily correlated to the stacking of the material.

ORCID iDs

B Li https://orcid.org/0000-0002-2345-6735
U Höfer https://orcid.org/0000-0002-5706-1205
G Mette https://orcid.org/0000-0001-7561-3264

References

[1] Novoselov K S, Geim A K, Morozov S V, Jiang D, Zhang Y, Dubonos S V, Grigorieva I V and Firsov A A 2004 Electric field effect in atomically thin carbon films *Science* **306** 666–9

[2] Mak K F, Lee C, Hone J, Shan J and Heinz T F 2010 Atomically thin MoS_2: a new direct-gap semiconductor *Phys. Rev. Lett.* **105** 136805

[3] Splendiani A, Sun L, Zhang Y, Li T, Kim J, Chim C-Y, Galli G and Wang F 2010 Emerging photoluminescence in monolayer MoS_2 *Nano Lett.* **10** 1271–5

[4] Geim A K and Grigorieva I V 2013 van der Waals heterostructures *Nature* **499** 419–25

[5] Lim H, Yoon S I, Kim G, Jang A R and Shin H S 2014 Stacking of two-dimensional materials in lateral and vertical directions *Chem. Mater.* **26** 4891–903

[6] Mak K F and Shan J 2016 Photonics and optoelectronics of 2D semiconductor transition metal dichalcogenides *Nat. Photon.* **10** 216–26

[7] Xiao D, Liu G B, Feng W X, Xu X D and Yao W 2012 Coupled spin and valley physics in monolayers of MoS_2 and other group-VI dichalcogenides *Phys. Rev. Lett.* **108** 196802

[8] Mak K F, He K L, Shan J and Heinz T F 2012 Control of valley polarization in monolayer MoS_2 by optical helicity *Nat. Nanotechnol.* **7** 494–8

[9] Zeng H L, Dai J F, Yao W, Xiao D and Cui X D 2012 Valley polarization in MoS_2 monolayers by optical pumping *Nat. Nanotechnol.* **7** 490–3

[10] Sallen G *et al* 2012 Robust optical emission polarization in MoS_2 monolayers through selective valley excitation *Phys. Rev.* B **86** 081301

[11] Komsa H P and Krasheninnikov A V 2013 Electronic structures and optical properties of realistic transition metal dichalcogenide heterostructures from first principles *Phys. Rev.* B **88** 085318

[12] Kang J, Tongay S, Zhou J, Li J B and Wu J Q 2013 Band offsets and heterostructures of two-dimensional semiconductors *Appl. Phys. Lett.* **102** 012111

[13] Chiu M H *et al* 2015 Determination of band alignment in the single-layer MoS_2/WSe_2 heterojunction *Nat. Commun.* **6** 7666

[14] Özcelik V O, Azadani J G, Yang C, Koester S J and Low T 2016 Band alignment of two-dimensional semiconductors for designing heterostructures with momentum space matching *Phys. Rev.* B **94** 035125

[15] Hill H M, Rigosi A F, Rim K T, Flynn G W and Heinz T F 2016 Band alignment in MoS_2/WS_2 transition metal

dichalcogenide heterostructures probed by scanning tunneling microscopy and spectroscopy *Nano Lett.* **16** 4831–7

[16] Lee C H *et al* 2014 Atomically thin p–n junctions with van der Waals heterointerfaces *Nat. Nanotechnol.* **9** 676–81

[17] Hong X P *et al* 2014 Ultrafast charge transfer in atomically thin MoS$_2$/WS$_2$ heterostructures *Nat. Nanotechnol.* **9** 682–6

[18] Ceballos F, Bellus M Z, Chiu H Y and Zhao H 2014 Ultrafast charge separation and indirect exciton formation in a MoS$_2$–MoSe$_2$ van der Waals heterostructure *ACS Nano* **8** 12717–24

[19] Rivera P *et al* 2015 Observation of long-lived interlayer excitons in monolayer MoSe$_2$–WSe$_2$ heterostructures *Nat. Commun.* **6** 6242

[20] Rigosi A F, Hill H M, Li Y, Chernikov A and Heinz T F 2015 Probing interlayer interactions in transition metal dichalcogenide heterostructures by optical spectroscopy: MoS$_2$/WS$_2$ and MoSe$_2$/WSe$_2$ *Nano Lett.* **15** 5033–8

[21] Kozawa D, Carvalho A, Verzhbitskiy I, Giustiniano F, Miyauchi Y, Mouri S, Neto A H C, Matsuda K and Eda G 2016 Evidence for fast interlayer energy transfer in MoSe$_2$/WS$_2$ heterostructures *Nano Lett.* **16** 4087–93

[22] Zhu H M, Wang J, Gong Z Z, Kim Y D, Hone J and Zhu X Y 2017 Interfacial charge transfer circumventing momentum mismatch at two-dimensional van der Waals heterojunctions *Nano Lett.* **17** 3591–8

[23] Merkl P *et al* 2019 Ultrafast transition between exciton phases in van der Waals heterostructures *Nat. Mater.* **18** 691

[24] Liu K H *et al* 2014 Evolution of interlayer coupling in twisted molybdenum disulfide bilayers *Nat. Commun.* **5** 4966

[25] Zheng S J, Sun L F, Zhou X H, Liu F C, Liu Z, Shen Z X and Fan H J 2015 Coupling and interlayer exciton in twist-stacked WS$_2$ bilayers *Adv. Opt. Mater.* **3** 1600–5

[26] Akashi R, Ochi M, Bordacs S, Suzuki R, Tokura Y, Iwasa Y and Arita R 2015 Two-dimensional valley electrons and excitons in noncentrosymmetric 3R-MoS$_2$ *Phys. Rev. Appl.* **4** 014002

[27] Yeh P C *et al* 2016 Direct measurement of the tunable electronic structure of bilayer MoS$_2$ by interlayer twist *Nano Lett.* **16** 953–9

[28] Yu H Y, Wang Y, Tong Q J, Xu X D and Yao W 2015 Anomalous light cones and valley optical selection rules of interlayer excitons in twisted heterobilayers *Phys. Rev. Lett.* **115** 187002

[29] Jin W C *et al* 2015 Substrate interactions with suspended and supported monolayer MoS$_2$: angle-resolved photoemission spectroscopy *Phys. Rev.* B **91** 121409

[30] Wang H, Bang J, Sun Y Y, Liang L B, West D, Meunier V and Zhang S B 2016 The role of collective motion in the ultrafast charge transfer in van der Waals heterostructures *Nat. Commun.* **7** 11504

[31] Heo H *et al* 2015 Interlayer orientation-dependent light absorption and emission in monolayer semiconductor stacks *Nat. Commun.* **6** 7372

[32] Zeng H *et al* 2013 Optical signature of symmetry variations and spin-valley coupling in atomically thin tungsten dichalcogenides *Sci. Rep.* **3** 1608

[33] Li Y, Rao Y, Mak K F, You Y, Wang S, Dean C R and Heinz T F 2013 Probing symmetry properties of few-layer MoS$_2$ and h-BN by optical second-harmonic generation *Nano Lett.* **13** 3329–33

[34] Malard L M, Alencar T V, Barboza A P M, Mak K F and de Paula A M 2013 Observation of intense second harmonic generation from MoS$_2$ atomic crystals *Phys. Rev.* B **87** 201401

[35] Kumar N, Najmaei S, Cui Q, Ceballos F, Ajayan P M, Lou J and Zhao H 2013 Second harmonic microscopy of monolayer MoS$_2$ *Phys. Rev.* B **87** 161403

[36] Janisch C, Wang Y X, Ma D, Mehta N, Elias A L, Perea-Lopez N, Terrones M, Crespi V and Liu Z W 2014 Extraordinary second harmonic generation in tungsten disulfide monolayers *Sci. Rep.* **4** 5530

[37] Miyauchi Y, Morishita R, Tanaka M, Ohno S, Mizutani G and Suzuki T 2016 Influence of the oxide thickness of a Sio$_2$/Si(001) substrate on the optical second harmonic intensity of few-layer MoSe$_2$ *Jpn. J. Appl. Phys.* **55** 085801

[38] Zhang X-Q, Lin C-H, Tseng Y-W, Huang K-H and Lee Y-H 2015 Synthesis of lateral heterostructures of semiconducting atomic layers *Nano Lett.* **15** 410–5

[39] Yin X, Ye Z, Chenet D A, Ye Y, O'Brien K, Hone J C and Zhang X 2014 Edge nonlinear optics on a MoS$_2$ atomic monolayer *Science* **344** 488–90

[40] Hsu W-T, Zhao Z-A, Li L-J, Chen C-H, Chiu M-H, Chang P-S, Chou Y-C and Chang W-H 2014 Second harmonic generation from artificially stacked transition metal dichalcogenide twisted bilayers *ACS Nano* **8** 2951–8

[41] Mannebach E M *et al* 2014 Ultrafast electronic and structural response of monolayer MoS$_2$ under intense photoexcitation conditions *ACS Nano* **8** 10734–42

[42] Wang G, Marie X, Gerber I, Amand T, Lagarde D, Bouet L, Vidal M, Balocchi A and Urbaszek B 2015 Giant enhancement of the optical second-harmonic emission of WSe$_2$ monolayers by laser excitation at exciton resonances *Phys. Rev. Lett.* **114** 097403

[43] Li D W *et al* 2016 Multimodal nonlinear optical imaging of MoS$_2$ and MoS$_2$-based van der Waals heterostructures *ACS Nano* **10** 3766–75

[44] Yao K Y *et al* 2020 Continuous wave sum frequency generation and imaging of monolayer and heterobilayer two-dimensional semiconductors *ACS Nano* **14** 708–14

[45] Shank C V, Yen R and Hirlimann C 1983 Femtosecond-time-resolved surface structural dynamics of optically excited silicon *Phys. Rev. Lett.* **51** 900–2

[46] Tom H W K, Aumiller G D and Brito-Cruz C H 1988 Time-resolved study of laser-induced disorder of Si surfaces *Phys. Rev. Lett.* **60** 1438–41

[47] Höfer U 1996 Nonlinear optical investigations of the dynamics of hydrogen interaction with silicon surfaces *Appl. Phys. Mater. Sci. Process.* **63** 533–47

[48] Voelkmann C, Reichelt M, Meier T, Koch S W and Höfer U 2004 Five-wave-mixing spectroscopy of ultrafast electron dynamics at a Si(001) surface *Phys. Rev. Lett.* **92** 127405

[49] Mauerer M, Shumay I L, Berthold W and Höfer U 2006 Ultrafast carrier dynamics in Si(111)7 × 7 dangling bonds probed by time-resolved second-harmonic generation and two-photon photoemission *Phys. Rev.* B **73** 245305

[50] McGuire J A, Raschke M B and Shen Y R 2006 Electron dynamics of silicon surface states: second-harmonic hole burning on Si(111)-(7 × 7) *Phys. Rev. Lett.* **96** 087401

[51] Qi J, Yeganeh M S, Koltover I, Yodh A G and Theis W M 1993 Depletion-electric-field-induced changes in 2nd-harmonic generation from GaAs *Phys. Rev. Lett.* **71** 633–6

[52] Lupke G 1999 Characterization of semiconductor interfaces by second-harmonic generation *Surf. Sci. Rep.* **35** 77–161

[53] Tisdale W A, Williams K J, Timp B A, Norris D J, Aydil E S and Zhu X Y 2010 Hot-electron transfer from semiconductor nanocrystals *Science* **328** 1543–7

[54] Boyd G T, Shen Y R and Hansch T W 1986 Continuous-wave 2nd-harmonic generation as a surface microprobe *Opt. Lett.* **11** 97–9

[55] Schultz K A and Seebauer E G 1992 Surface-diffusion of Sb on Ge(111) monitored quantitatively with optical 2nd harmonic microscopy *J. Chem. Phys.* **97** 6958–67

[56] Klass K, Mette G, Güdde J, Dürr M and Höfer U 2011 Second-harmonic microscopy for fluence-dependent investigation of laser-induced surface reactions *Phys. Rev.* B **83** 125116

[57] Wu K, Canterbury J D, Wilson P T and Downer M C 2003 Electric-field-induced second-harmonic microscopy *Phys. Status Solidi* c **0** 3081−5

[58] Manaka T, Lim E, Tamura R and Iwamoto M 2007 Direct imaging of carrier motion in organic transistors by optical secondharmonic generation *Nat. Photon.* **1** 581−4

[59] Satou H, Ohshima Y, Kohn H, Manaka T and Iwamoto M 2011 Direct observation of space charge field in tetracene field-effect transistor using time-resolved microscopic optical second harmonic generation *J. Appl. Phys.* **109** 054506

[60] Morris J D, Atallah T L, Lombardo C J, Park H, Dodabalapur A and Zhu X Y 2013 Mapping electric field distributions in biased organic bulk heterojunctions under illumination by nonlinear optical microscopy *Appl. Phys. Lett.* **102** 033301

[61] Gao J, Li B C, Tan J W, Chow P, Lu T M and Koratkar N 2016 Aging of transition metal dichalcogenide monolayers *ACS Nano* **10** 2628−35

[62] Mouri S, Miyauchi Y and Matsuda K 2013 Tunable photoluminescence of monolayer MoS$_2$ via chemical doping *Nano Lett.* **13** 5944−8

[63] Edelberg D *et al* 2019 Approaching the intrinsic limit in transition metal diselenides via point defect control *Nano Lett.* **19** 4371−9

[64] Yang S X, Kang J, Yue Q and Yao K 2014 Vapor phase growth and imaging stacking order of bilayer molybdenum disulfide *J. Phys. Chem.* C **118** 9203−8

[65] Heinz T F, Loy M M T and Thompson W A 1985 Study of Si(111) surfaces by optical 2nd-harmonic generation-reconstruction and surface phase-transformation *Phys. Rev. Lett.* **54** 63−6

[66] Kim K *et al* 2012 Raman spectroscopy study of rotated double-layer graphene: misorientation-angle dependence of electronic structure *Phys. Rev. Lett.* **108** 246103

[67] Havener R W, Zhuang H L, Brown L, Hennig R G and Park J 2012 Angle-resolved Raman imaging of inter layer rotations and interactions in twisted bilayer graphene *Nano Lett.* **12** 3162−7

[68] Ceballos F, Cui Q, Bellus M Z and Zhao H 2016 Exciton formation in monolayer transition metal dichalcogenides *Nanoscale* **8** 11681−8

[69] Nie Z *et al* 2014 Ultrafast carrier thermalization and cooling dynamics in few-layer MoS$_2$ *ACS Nano* **8** 10931−40

[70] You Y M, Zhang X X, Berkelbach T C, Hybertsen M S, Reichman D R and Heinz T F 2015 Observation of biexcitons in monolayer WSe$_2$ *Nat. Phys.* **11** 477−81

[71] Sun D Z, Rao Y, Reider G A, Chen G G, You Y M, Brezin L, Harutyunyan A R and Heinz T F 2014 Observation of rapid exciton–exciton annihilation in monolayer molybdenum disulfide *Nano Lett.* **14** 5625−9

[72] Shi H, Yan R, Bertolazzi S, Brivio J, Gao B, Kis A, Jena D, Xing H G and Huang L B 2013 Exciton dynamics in suspended monolayer and few-layer MoS$_2$ 2D crystals *ACS Nano* **7** 1072−80

[73] Wang H N, Zhang C J and Rana F 2015 Ultrafast dynamics of defect-assisted electron hole recombination in monolayer MoS$_2$ *Nano Lett.* **15** 339−45

[74] Wang H N, Zhang C J and Rana F 2015 Surface recombination limited lifetimes of photoexcited carriers in few-layer transition metal dichalcogenide MoS$_2$ *Nano Lett.* **15** 8204−10

[75] Korn T, Heydrich S, Hirmer M, Schmutzler J and Schüller C 2011 Low-temperature photocarrier dynamics in monolayer MoS$_2$ *Appl. Phys. Lett.* **99** 102109

[76] Wang R, Ruzicka B A, Kumar N, Bellus M Z, Chiu H Y and Zhao H 2012 Ultrafast and spatially resolved studies of charge carriers in atomically thin molybdenum disulfide *Phys. Rev.* B **86** 045406

[77] Wang Q S, Ge S F, Li X, Qiu J, Ji Y X, Feng J and Sun D 2013 Valley carrier dynamics in monolayer molybdenum disulfide from helicity-resolved ultrafast pump-probe spectroscopy *ACS Nano* **7** 11087−93

[78] Seo M *et al* 2016 Ultrafast optical microscopy of single monolayer molybdenum disulfide flakes *Sci. Rep.* **6** 21601

[79] Cha S, Sung J H, Sim S, Park J, Heo H, Jo M H and Choi H 2016 1s-intraexcitonic dynamics in monolayer MoS$_2$ probed by ultrafast mid-infrared spectroscopy *Nat. Commun.* **7** 10768

[80] Goswami T, Rani R, Hazra K S and Ghosh H N 2019 Ultrafast carrier dynamics of the exciton and trion in MoS$_2$ monolayers followed by dissociation dynamics in Au@MoS$_2$ 2D heterointerfaces *J. Phys. Chem. Lett.* **10** 3057−63

[81] He J G, Hummer K and Franchini C 2014 Stacking effects on the electronic and optical properties of bilayer transition metal dichalcogenides MoS$_2$, MoSe$_2$, WS$_2$, and WSe$_2$ *Phys. Rev.* B **89** 075409

[82] Wang Y, Wang Z, Yao W, Liu G B and Yu H Y 2017 Interlayer coupling in commensurate and incommensurate bilayer structures of transition-metal dichalcogenides *Phys. Rev.* B **95** 115429

[83] Ou Y, Kang Z, Liao Q, Gao S, Zhang Z and Zhang Y 2020 Point defect induced intervalley scattering for the enhancement of interlayer electron transport in bilayer MoS$_2$ homojunctions *Nanoscale* **12** 9859−65

Supplemental Material

Second-harmonic imaging microscopy for time-resolved investigations of transition metal dichalcogenides

J. E. Zimmermann[1], B. Li[2], J. Hone[2], U. Höfer[1], and G. Mette[1,*]

[1]Fachbereich Physik und Zentrum für Materialwissenschaften, Philipps-Universität, 35032 Marburg, Germany

[2]Department of Mechanical Engineering, Columbia University, New York 10027, United States

* corresponding author: gerson.mette@physik.uni-marburg.de

1   Spatial resolution

The spatial resolution of our SHG imaging microscopy setup has been determined by usage of a standard resolution target to be better than 4 μm (Fig. S1).
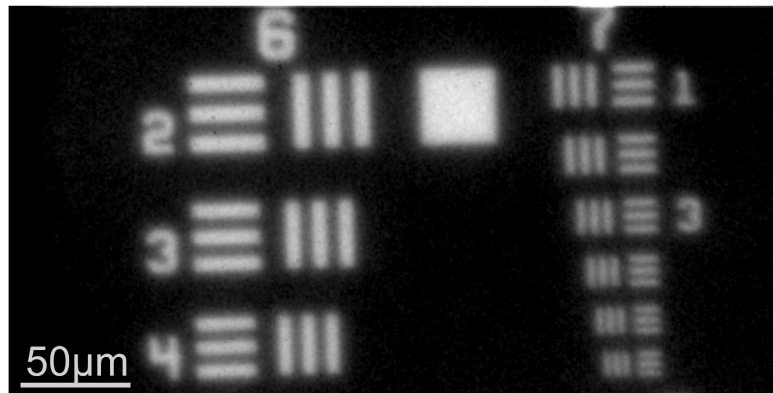

Figure S1: Microscopy image of the standard 1951 USAF resolution target. Clear differentiation of the smallest line pairs determines the resolution to be better than 4 μm.

2 Photoluminescence

Photoluminescence (PL) is measured at room temperature by a Renishaw inVia Micro-Raman system using monochromatic laser excitation of 532 nm. Fig. S2 compares the PL signals obtained from CVD grown and exfoliated MoS_2 monolayer flakes on the same SiO_2/Si substrate. The PL peak of both, exfoliated and CVD grown MoS_2, is centered at 1.85 eV indicating low doping during the CVD synthesis process, since doping would not only change the PL peak intensity, but also its energetic position [1]. Although PL is not a quantitative measurement of defect density, the increase of PL quantum yield implies the reduction of band edge disorder, which also indicates a lower number of defect states [2]. Therefore, the high peak intensity in comparison to exfoliated MoS_2 suggests a relatively low defect density of the CVD grown monolayers.
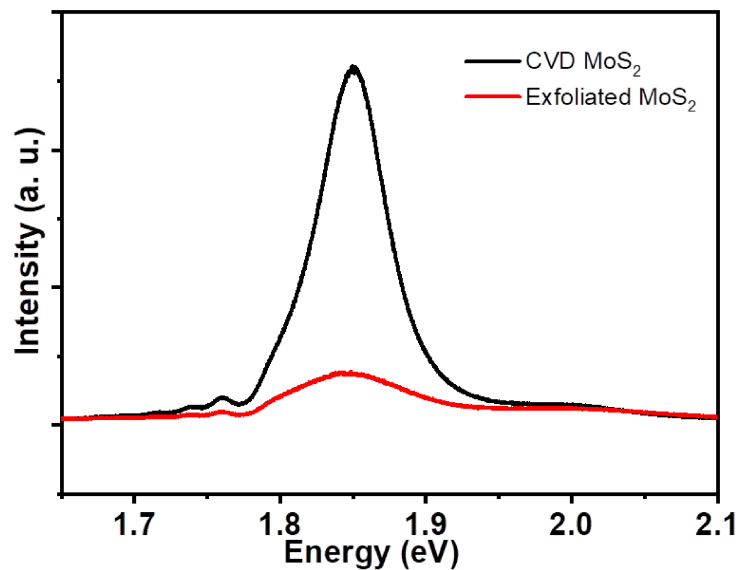

Figure S2: Photoluminescence of CVD grown MoS_2 (black) in comparison with exfoliated MoS_2 (red).

3 Symmetry of the second-harmonic polarization

The majority of previous rotational anisotropy SHG studies on TMDs are rotating the sample while the angle between the incoming fundamental and outgoing second harmonic is fixed [3–8]. This gives direct access to the symmetry of the sample and to the crystal orientation. However, in order to exploit the advantage of SHG imaging microscopy probing a larger surface area at once, we chose to fixate the angle between the outgoing second harmonic and the sample orientation while changing the polarization angle of the incoming fundamental as it has been applied previously [9, 10]. In general the polarization in dipole approximation for the second harmonic is given by:

$$\mathbf{P}^{(2)}(2\omega) = \epsilon_0 \chi^{(2)}(2\omega) : \mathbf{E}(\omega)\mathbf{E}(\omega) \tag{1}$$

where $\chi^{(2)}$ stands for the second-order non-linear susceptibility which is represented as a third order tensor with 27 elements.

For second-harmonic generation, this tensor is reduced to a 3×6 matrix

$$\chi^{(2)} = \begin{pmatrix} \chi_{xxx}^{(2)} & \chi_{xyy}^{(2)} & \chi_{xzz}^{(2)} & \chi_{xzy}^{(2)} & \chi_{xzx}^{(2)} & \chi_{xxy}^{(2)} \\ \chi_{yxx}^{(2)} & \chi_{yyy}^{(2)} & \chi_{yzz}^{(2)} & \chi_{yzy}^{(2)} & \chi_{yzx}^{(2)} & \chi_{yxy}^{(2)} \\ \chi_{zxx}^{(2)} & \chi_{zyy}^{(2)} & \chi_{zzz}^{(2)} & \chi_{zzy}^{(2)} & \chi_{zzx}^{(2)} & \chi_{zxy}^{(2)} \end{pmatrix} \tag{2}$$

where x, y and z represent the crystal coordinates.

A rotation of the crystal coordinates in relation to the lab coordinates (Ψ) around the z-axis corresponds to the transformation matrix

$$\mathrm{A} = \begin{pmatrix} a_{11} & a_{12} & a_{13} \\ a_{21} & a_{22} & a_{23} \\ a_{31} & a_{32} & a_{33} \end{pmatrix} = \begin{pmatrix} \cos(\Psi) & \sin(\Psi) & 0 \\ -\sin(\Psi) & \cos(\Psi) & 0 \\ 0 & 0 & 1 \end{pmatrix} \tag{3}$$

which transforms $\chi^{(2)}$ as follows

$$\chi_{ijk}^{(2)} = \sum_{lmn} a_{il} a_{jm} a_{kn} \chi_{lmn}'^{(2)} \tag{4}$$

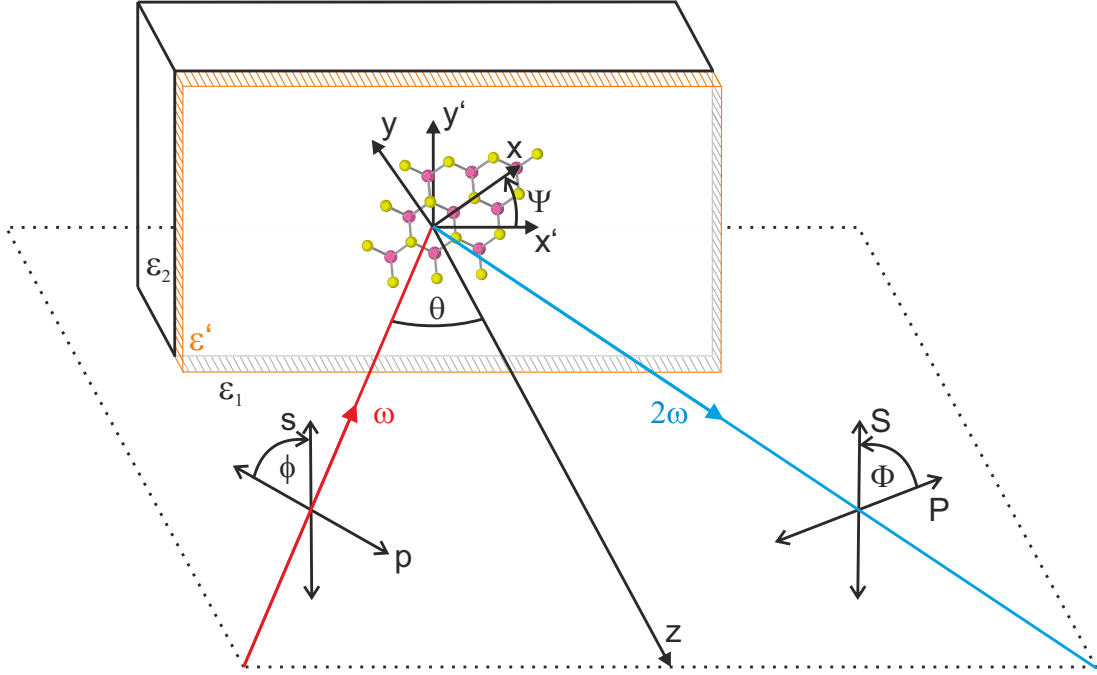between the lab coordinates (ijk) and the crystal coordinates (lmn).

Figure S3: Schematic drawing of the experimental geometry for the incoming fundamental ω and the outgoing second-harmonic signal 2ω. The dashed rectangle marks the plane of incidence, θ is the angle of incidence. ϕ and Φ describe the polarization angles of the fundamental and the second-harmonic light, respectively. x', y' represent the lab coordinates and x,y the crystal coordinates. Ψ denotes the rotation angle of the crystal coordinates with respect to the lab coordinates.

The transformation in combination with an even further reduction of the tensor due to the D_{3h} symmetry of TMD monolayer crystals leads to the following form of $\chi^{(2)}$

$$\chi^{(2)} = \chi_{xxx} \cdot \begin{pmatrix} \cos(3\Psi) & -\cos(3\Psi) & 0 & 0 & 0 & -\sin(3\Psi) \\ -\sin(3\Psi) & \sin(3\Psi) & 0 & 0 & 0 & -\cos(3\Psi) \\ 0 & 0 & 0 & 0 & 0 & 0 \end{pmatrix}. \tag{5}$$

By applying the theoretical model of Heinz [11] which assumes a finite nonlinear sheet with dielectric constant ϵ' imbedded between two media with dielectric constants ϵ_1 and ϵ_2 as sketched in Fig. S3, we can directly access the SH response of the system from Eq. 6:

$$\mathbf{E}(2\omega) = \frac{i2\omega}{c\sqrt{\epsilon_i(2\omega)}} \frac{2\pi}{\cos(\theta)(2\omega)} \mathbf{F}(2\omega)\chi^{(2)}\mathbf{f}(\omega)|\mathbf{E}(\omega)|^2. \tag{6}$$

$\mathbf{F}(2\omega)$ and $\mathbf{f}(\omega)$ represent the Fresnel factors which describe the interaction of the outgoing and incoming electric fields with the dielectric medium of the sample and the underlying substrate:

$$\mathbf{F}(2\omega) = \left(\begin{array}{ccc} F_{ij}^{xx} F_c^i \cos(\Phi) \exp^{i\Delta}, & F_{ij}^{yy} \sin(\Phi), & F_{ij}^{zz} F_s^i \cos(\Phi) \exp^{i\Delta} \end{array} \right) \tag{7}$$

$$\mathbf{f}(\omega) = \begin{pmatrix} (f_{ij}^{xx})^2 f_c^{i2} \cos^2(\phi) \exp^{i2\delta} \\ (f_{ij}^{yy})^2 \sin^2(\phi) \\ (f_{ij}^{zz})^2 f_s^{i2} \cos^2(\phi) \exp^{i2\delta} \\ 2 f_{ij}^{yy} f_{ij}^{zz} f_s^i \cos(\phi) \sin(\phi) \exp^{i\delta} \\ 2 f_{ij}^{xx} f_{ij}^{zz} f_s^i f_c^i \cos^2(\phi) \exp^{i2\delta} \\ 2 f_{ij}^{xx} f_{ij}^{yy} f_c^i \cos(\phi) \sin(\phi) \exp^{i\delta} \end{pmatrix} \tag{8}$$

with

$$f_{ij}^{xx} = t_{ij}^p \frac{f_c^j}{f_c^i}, \ \ f_{ij}^{yy} = t_{ij}^s, \ \ f_{ij}^{zz} = t_{ij}^p \frac{\epsilon_j(\omega) f_s^j}{\epsilon'(\omega) f_s^i} \tag{9}$$

$$F_{ij}^{xx} = T_{ij}^p \frac{F_c^j}{F_c^i}, \ \ F_{ij}^{yy} = T_{ij}^s, \ \ F_{ij}^{zz} = T_{ij}^p \frac{\epsilon_j(2\omega) F_s^j}{\epsilon'(2\omega) F_s^i} \tag{10}$$

$$f_s^i = \frac{\sin(\theta_i(\omega))}{\tilde{n}_i(\omega)}, \ \ f_c^i = \sqrt{1 - f_s^{i2}}, \ \ f_s^j = \sin(\theta_i(\omega)) \frac{\tilde{n}_i(\omega)}{\tilde{n}_j(\omega)}, \ \ f_c^j = \sqrt{1 - f_s^{j2}} \tag{11}$$

$$F_s^i = f_s^i(2\omega), \ \ F_c^i = f_c^i(2\omega), \ \ T_{ij}^s = t_{ij}^s(2\omega), \ \ T_{ij}^p = t_{ij}^p(2\omega) \tag{12}$$

$$t_{ij}^s = \frac{2 f_c^i \tilde{n}_i(\omega)}{f_c^i \tilde{n}_i(\omega) + f_c^j \tilde{n}_j(\omega)}, \ \ t_{ij}^p = \frac{2 f_c^i \tilde{n}_i(\omega)}{f_c^i \tilde{n}_j(\omega) + f_c^j \tilde{n}_i(\omega)}. \tag{13}$$

$\tilde{n}_x$ represent the wavelength-dependent complex refractive indices $\tilde{n}_x = n_x + \mathrm{i}k_x$ in the two embedding media. In our case, $\tilde{n}_i$ corresponds to air with $n_i(\omega) = 1$, $k_i(\omega) = 0$, $n_i(2\omega) = 1$ and $k_i(2\omega) = 0$. $\tilde{n}_j$ corresponds to SiO$_2$ with $n_j(\omega) = 1.5383$, $k_j(\omega) = 0$, $n_j(2\omega) = 1.5577$ and $k_j(2\omega) = 0$. In our case of linearly polarized probe light $\delta = 0$. For left or right circularly polarized light $\delta \pm \pi/2$ and $\phi = \pi/4$. The same adheres to Δ and Φ for circularly polarized second-harmonic light.

In order to access the rotational or polarizational anisotropy of the SH response in dependence of the crystal orientation, the polarization of the generated SH light and the angle of incidence, one has to solve Eq. 6. Multiplication of $\mathbf{E}(2\omega)$ with its conjugated complex will then yield the

SH intensity. However, because the general solution of this equation becomes rather long, the specification of some variables helps to gain more insight without loss of generality.

For the description of polarizational anisotropy, it is of course reasonable to constrain the crystal orientation to a specific value (e.g. its armchair direction parallel to the horizontal, i.e. $\Psi = 0°$). Furthermore, the analyzed polarization of the SH light can be constrained to p-polarization (i.e. parallel to the horizontal, $\Phi = 0°$). If the nonlinear sheet is situated on a specific substrate and the probe beam approaches this interface via air or vacuum (medium 1), real and imaginary part of the respective refractive index correspond to $n_i(\omega) = 1$, $k_i(\omega) = 0$, $n_i(2\omega) = 1$ and $k_i(2\omega) = 0$.

This simplification then results in the following Eq. 14 describing the electric field of the generated SH light in dependence of the probe polarization ϕ and the angle of incidence θ:

$$
\mathbf{E}_{2\omega}(\phi, \theta, n_\omega, n_{2\omega}, k_\omega, k_{2\omega}) \propto 8|\cos(\theta)|^3 \sqrt{1 + \frac{\sin(\theta)^2}{(k_{2\omega} - \mathrm{i}n_{2\omega})^2}} \times
$$

$$
\left(\frac{\dfrac{\cos(\phi)^2 \left(1 + \frac{\sin(\theta)^2}{(k_\omega - \mathrm{i}n_\omega)^2}\right)}{\left((\mathrm{i}k_\omega + n_\omega)|\cos(\theta)| + \sqrt{1 + \frac{\sin(\theta)^2}{(k_\omega - \mathrm{i}n_\omega)^2}}\right)^2} - \dfrac{\sin(\phi)^2}{\left(|\cos(\theta)| + (\mathrm{i}k_\omega + n_\omega)\sqrt{1 + \frac{\sin(\theta)^2}{(k_\omega - \mathrm{i}n_\omega)^2}}\right)^2}}{(\mathrm{i}k_{2\omega} + n_{2\omega})|\cos(\theta)| + \sqrt{1 + \frac{\sin(\theta)^2}{(k_{2\omega} - \mathrm{i}n_{2\omega})^2}}} \right) \quad (14)
$$

 with n and k representing the wavelength-dependent complex refractive index of the substrate (medium 2): $n_\omega = n_j(\omega)$, $k_\omega = k_j(\omega)$, $n_{2\omega} = n_j(2\omega)$ and $k_{2\omega} = k_j(2\omega)$.

In the same way, the rotational anisotropy can be derived with the polarizations of the fundamental and the SH light constrained (e.g. both p-polarized, i.e. parallel to the horizontal, $\phi = 0°$, $\Phi = 0°$) resulting in Eq. 15 describing the electric field of the generated SH light in dependence of the sample orientation Ψ and the angle of incidence θ:

$$
\mathbf{E}_{2\omega}(\Psi, \theta, n_\omega, n_{2\omega}, k_\omega, k_{2\omega}) \propto
$$

$$
\frac{8|\cos(\theta)|^3 \cos(3\Psi) \left(1 + \frac{\sin(\theta)^2}{(k_\omega - \mathrm{i}n_\omega)^2}\right) \sqrt{1 + \frac{\sin(\theta)^2}{(k_{2\omega} - \mathrm{i}n_{2\omega})^2}}}{\left((\mathrm{i}k_\omega + n_\omega)|\cos(\theta)| + \sqrt{1 + \frac{\sin(\theta)^2}{(k_\omega - \mathrm{i}n_\omega)^2}}\right)^2 \left((\mathrm{i}k_{2\omega} + n_{2\omega})|\cos(\theta)| + \sqrt{1 + \frac{\sin(\theta)^2}{(k_{2\omega} - \mathrm{i}n_{2\omega})^2}}\right)} \quad (15)
$$

6

For the special case of normal incidence of the incoming laser beam ($\theta = 0°$), the polarization dependence of the Fresnel factors vanishes and we get for the rotational anisotropy:

$$\mathbf{E}_{2\omega}(\Psi, n_\omega, n_{2\omega}, k_\omega, k_{2\omega}) \quad = \frac{8\cos(3\Psi)}{(1+\mathrm{i}k_\omega+n_\omega)^2(1+\mathrm{i}k_{2\omega}+n_{2\omega})}, \tag{16}$$

which describes the well-known three-fold rotational symmetry expected for TMD monolayers in consistence with previous studies [3–8].

In the same way, we yield for the polarizational anisotropy for a fixed crystal orientation $\Psi = 0°$ and p-polarized SH light:

$$\mathbf{E}_{2\omega}(\phi, n_\omega, n_{2\omega}, k_\omega, k_{2\omega}) \quad = \frac{8\mathrm{i}\cos(2\phi)}{(k_\omega-\mathrm{i}(1+n_\omega))^2(k_{2\omega}-\mathrm{i}(1+n_{2\omega}))}, \tag{17}$$

describing a two-fold symmetric anisotropy.

For an unrestricted crystal orientation Ψ, the P- and S-polarized components of the SH response depend on the incoming polarization angle ϕ at normal incidence as follows:

$$\begin{aligned} \mathbf{E}_{\mathrm{P}}^{2\omega}(\phi) &\propto \cos(2\phi + 3\Psi) \\ \mathbf{E}_{\mathrm{S}}^{2\omega}(\phi) &\propto \sin(2\phi + 3\Psi) \end{aligned} \tag{18}$$

Accordingly, in the polarization dependent measurements at normal incidence, one will always find a two-fold symmetry, but with a specific phase 3Ψ depending on the crystal orientation Ψ of the sample[1]. It is necessary to mention that the applied SH approach without phase information does not discriminate opposite crystal orientations. Consequently, the evaluation only determines domain orientations modulo $60°$.

---

[1]Please note that our result of this additional phase deviates from a similar derivation in Ref. [10]
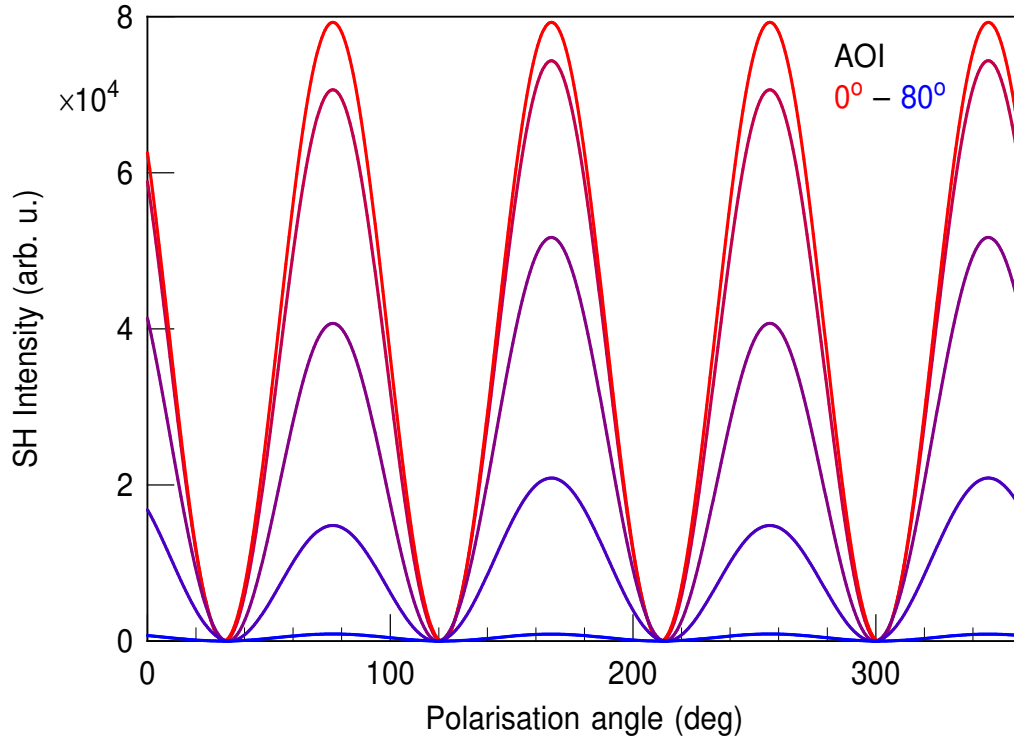
Figure S4: Simulation of the polarizational anisotropy of the SH intensity in dependence of the angle of incidence (AOI).

In our experiments, the incoming laser beam does not incident normal to the surface, but the fundamental is focused on the sample under an angle of $\theta = 18°$. With rising angle of incidence, the influence of the Fresnel factors on the polarization dependence increases which breaks the two-fold symmetry and considerably changes the detected SH anisotropy as simulated in Fig. S4. In our case of a small angle of incidence, a comparably small change of the intensities finally yields two pairs of maxima with slightly different heights as shown in Fig. S5 for an experimental polarization dependence in comparison with two model fits including and excluding the influence of the non-vanishing angle of incidence.
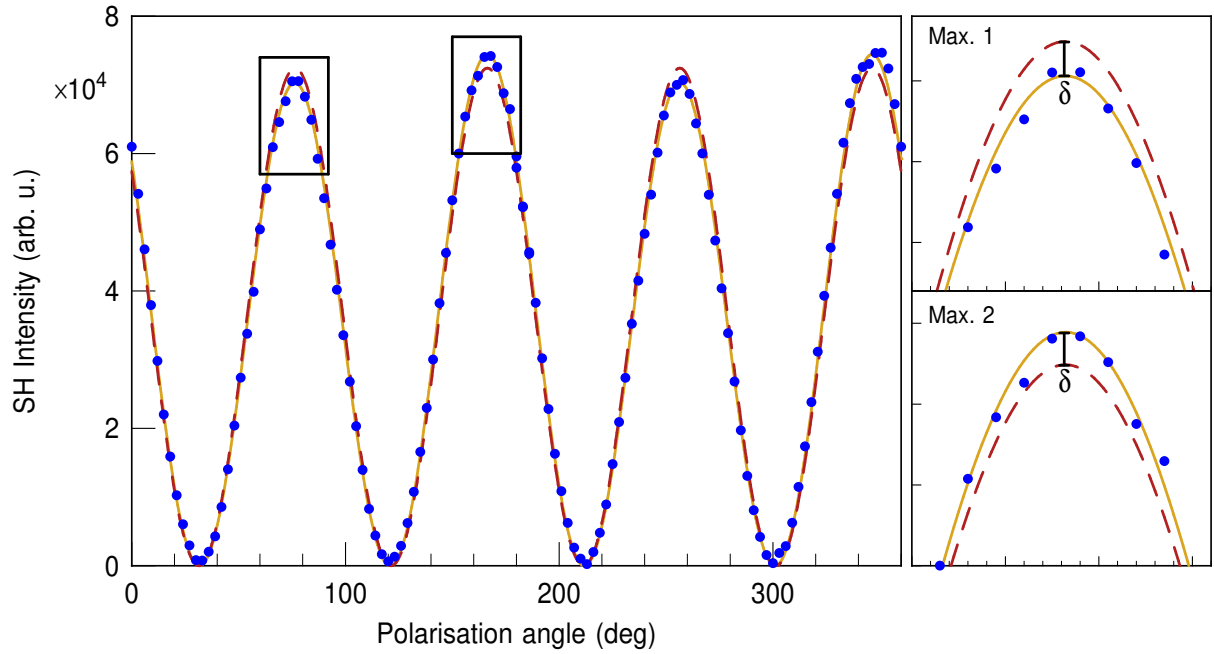
Figure S5: Left: Measured polarisation dependence of the SH intensity (blue) in comparison with two model fits including (orange solid line) and excluding (red dashed line) the polarization dependence of the Fresnel factors due to the non-vanishing angle of incidence. Since the incoming probe laser beam does not incident normal to the surface, the polarization dependence of the Fresnel factors has to be considered. The two-fold symmetry obtained for normal incidence is clearly broken and one observes two pairs of maxima with different heights which can be well described by the respective model for an angle of incidence of $\theta = 18°$. Right: Close-up of the two different maxima. δ denotes the small but still clear difference between the two models.
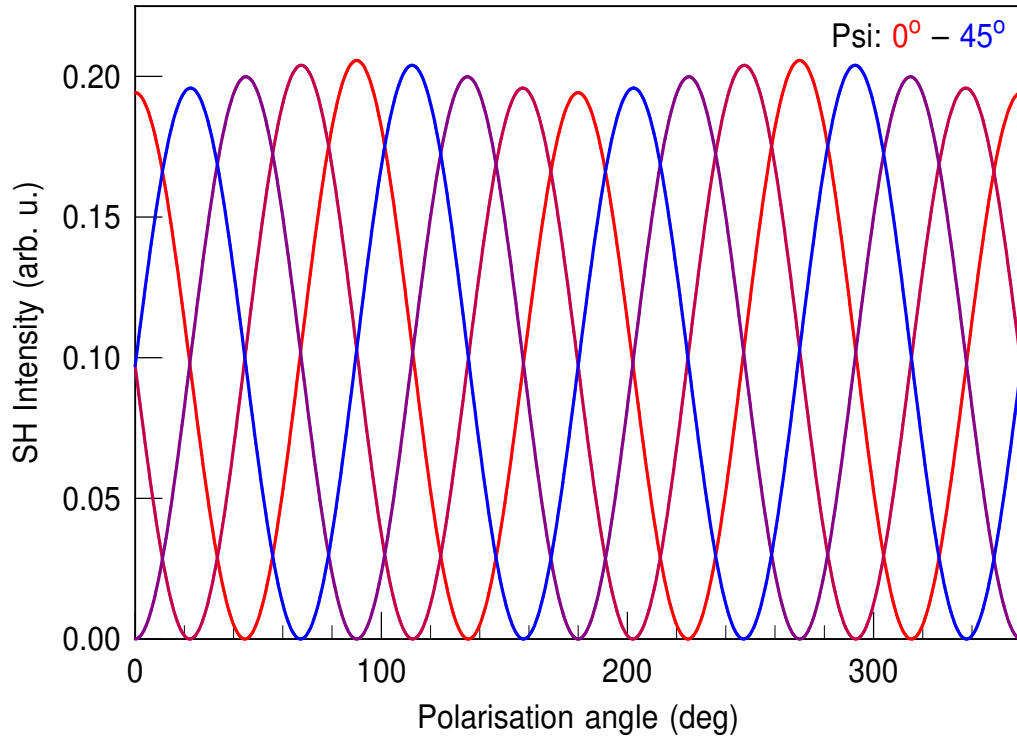
9

Figure S6: Simulated polarizational anisotropies for different crystal orientations Ψ for p-polarized SH light and an angle of incidence of 18°.

As discussed above, the crystal orientation Ψ leads to a phase 3Ψ in the polarizational anisotropy. In combination with a non-vanishing angle of incidence θ, this leads to an intensity variation in the polarizational anisotropy which is simulated in Fig. S6 for our experimental conditions ($\theta = 18°$, p-polarized SH light) for crystal orientations Ψ between 0° and 45°.

4 Automatized evaluation of crystal orientations

By applying the afore discussed formalism, the polarization dependence of the second-harmonic intensity of every single pixel of the obtained image series is fitted by an automated routine. This gives us direct access to the orientation of all the visible flakes in the SH image. The result of this procedure is displayed in Fig. S7. The raw image (left) after the evaluation looks rather unclear at first sight. In order to refine the picture, the error given by the fit procedure for each pixel (center) is used as a filter to eliminate all pixels without a defined polarization dependence, i.e. in particular all uncovered substrate areas. The final result after this background elimination can be seen on the right side of Fig. S7. The crystal orientation for each individual flake including overlapping domains and growth errors like twins can be easily identified.
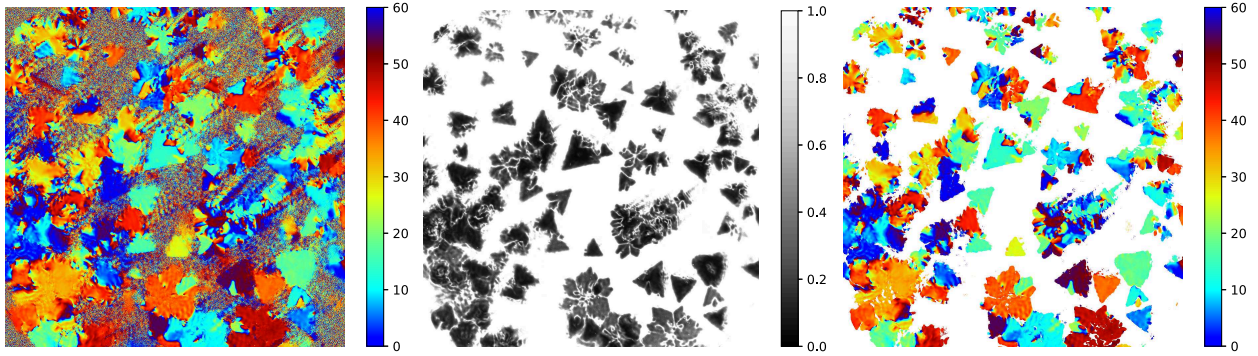

Figure S7: Left: Raw image of the crystal orientation as evaluated by an automated fitting routine for each single pixel of the whole SHG image. Middle: Error map of the fitting routine. Large errors (white) correspond to uncovered substrate regions, while small errors (black) reproduce the sample area which is covered by MoS_2 mono- and multilayer flakes. Right: Result of the automatized evaluation of the crystal orientation after filtering the raw image with the error map.

5 Consistency and accuracy of the evaluation

The consistency of the introduced formalism for the evaluation of crystal orientations can easily be confirmed by comparison with optical microscopy. Since it is well known that MoS$_2$ flakes grow in triangular shape with the zigzag direction parallel to the edges [12, 13], one can determine the crystal orientations of the MoS$_2$ flakes from the optical image and compare these to the orientations evaluated from the polarization-dependent SHG measurements. As shown in Fig. S8 the agreement of the determined angles is very good. The mean value for the deviation yields 0.8° ± 0.4°. Thus, the validity of our evaluation method within the estimated experimental errors is confirmed.
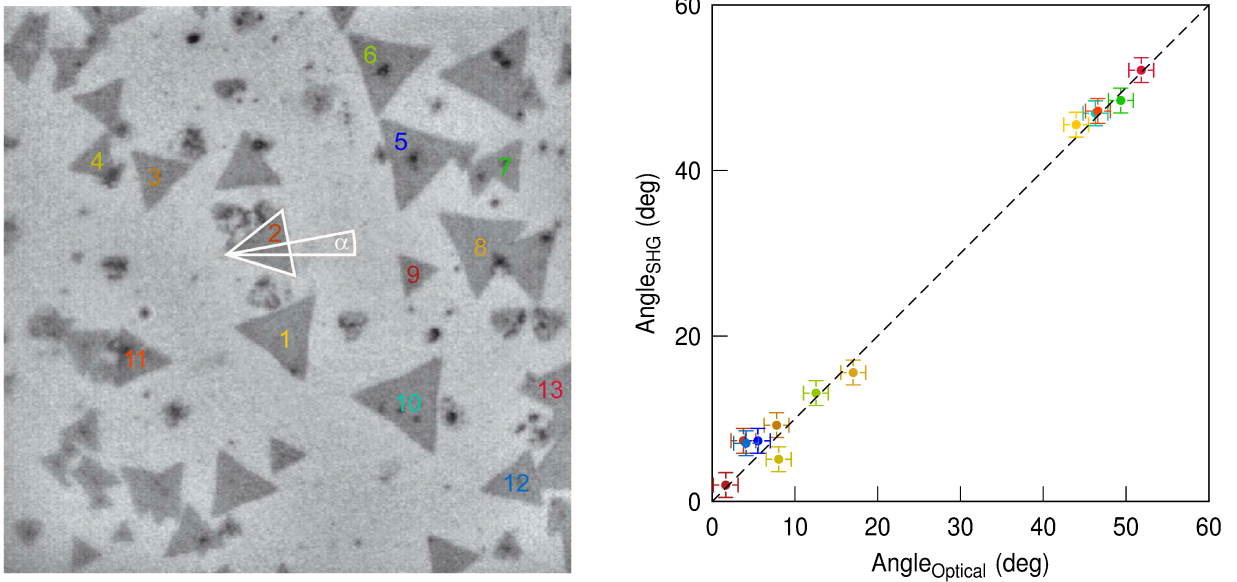

Figure S8: **Left:** Optical image of a CVD grown MoS$_2$ monolayer sample with 13 evaluated MoS$_2$ flakes. An exemplary angle α between the determined armchair direction and the horizontal is shown. **Right:** Crystal orientation for the armchair direction of the corresponding MoS$_2$ flakes determined by SHG imaging microscopy and optical microscopy. Experimental errors are estimated to be $\approx 1°$ for both techniques. The dashed line represents the identity function.

6 Rate-equation model for fitting procedure

To describe the relaxation dynamics visible in the SH transients a simple rate-equation approach is used. Here, a population is generated by the pump pulse which is then analyzed by the probe pulse. The change in SH intensity is proportional to the density of excited states. The decay mechanism for the intensity change is interpreted as a defect-assisted scattering process. We assume here that two populations N_1 and N_2 exist which decay via two independent channels back to the ground state:

$$\frac{dN}{dt} = -N_1(t)\lambda_1 - N_2(t)\lambda_2 \tag{19}$$

$$\Rightarrow N(t) = N_1(t) + N_2(t) \tag{20}$$

$$N_1(t) = N_{1,0} \exp^{-\lambda_1 t} \tag{21}$$

$$N_2(t) = N_{2,0} \exp^{-\lambda_2 t} \tag{22}$$

where λ_1 and λ_2 are the respective decay rates and $N(t)$ represents the total number of excited states. $N_1(t)$ is proportional to the density of fast defects. As soon as the fast defects are saturated the slower decay process dominates the dynamics.

References

[1] S. Mouri, Y. Miyauchi, and K. Matsuda, Nano Letters **13**, 5944 (2013), pMID: 24215567.

[2] D. Edelberg, D. Rhodes, A. Kerelsky, B. Kim, J. Wang, A. Zangiabadi, C. Kim, A. Abhinandan, J. Ardelean, M. Scully, D. Scullion, L. Embon, R. Zu, E. J. G. Santos, L. Balicas, C. Marianetti, K. Barmak, X. Zhu, J. Hone, and A. N. Pasupathy, Nano Letters **19**, 4371 (2019).

[3] Y. Li, Y. Rao, K. F. Mak, Y. You, S. Wang, C. R. Dean, and T. F. Heinz, Nano Lett. **13**, 3329 (2013).

[4] L. M. Malard, T. V. Alencar, A. P. M. Barboza, K. F. Mak, and A. M. de Paula, Phys. Rev. B **87**, 201401 (2013).

[5] N. Kumar, S. Najmaei, Q. Cui, F. Ceballos, P. M. Ajayan, J. Lou, and H. Zhao, Phys. Rev. B **87**, 161403 (2013).

[6] C. Janisch, Y. X. Wang, D. Ma, N. Mehta, A. L. Elias, N. Perea-Lopez, M. Terrones, V. Crespi, and Z. W. Liu, Sci. Rep. **4**, 5530 (2014).

[7] Y. Miyauchi, R. Morishita, M. Tanaka, S. Ohno, G. Mizutani, and T. Suzuki, Jpn. J. Appl. Phys. **55**, 085801 (2016).

[8] X.-Q. Zhang, C.-H. Lin, Y.-W. Tseng, K.-H. Huang, and Y.-H. Lee, Nano Lett. **15**, 410 (2015).

[9] X. Yin, Z. Ye, D. A. Chenet, Y. Ye, K. O'Brien, J. C. Hone, and X. Zhang, Science **344**, 488 (2014).

[10] E. M. Mannebach, K.-A. N. Duerloo, L. A. Pellouchoud, M.-J. Sher, S. Nah, Y.-H. Kuo, Y. Yu, A. F. Marshall, L. Cao, E. J. Reed, and A. M. Lindenberg, ACS Nano **8**, 10734 (2014).

[11] T. F. Heinz, in *Nonlinear Surface Electromagnetic Phenomena*, edited by H.-E. Ponath and G. I. Stegeman (Elsevier, Amsterdam, 1991).

[12] L. S. Byskov, J. K. Norskov, B. S. Clausen, and H. Topsoe, Catal. Lett. **64**, 95 (2000).

[13] J. V. Lauritsen, J. Kibsgaard, S. Helveg, H. Topsoe, B. S. Clausen, E. Laegsgaard, and F. Besenbacher, Nat. Nanotechnol. **2**, 53 (2007).

Article II

Directional Ultrafast Charge Transfer in a WSe$_2$/MoSe$_2$ Heterostructure Selectively Probed by Time-Resolved SHG Imaging Microscopy

J.E. Zimmermann, Y.D. Kim, J.C. Hone, U. Höfer, and G. Mette;

COMMUNICATION

Check for updates

Directional ultrafast charge transfer in a WSe₂/MoSe₂ heterostructure selectively probed by time-resolved SHG imaging microscopy†

Jonas E. Zimmermann,[a] Young Duck Kim,‡[b] James C. Hone,[b] Ulrich Höfer[a] and Gerson Mette (ID) *[a]

Heterostructures of two-dimensional transition metal dichalcogenides (TMD) have shown promise for various optoelectronic and novel valleytronic applications. Due to their type-II band alignment, photoexcited electrons and holes can separate into different layers through ultrafast charge transfer. While this charge-transfer process is critical for potential applications, the underlying mechanisms still remain elusive. Here, we demonstrate for a rotationally mismatched WSe₂/MoSe₂ heterostructure that directional ultrafast charge transfer between the layers becomes accessible by time-resolved optical second-harmonic generation. By tuning the photon energy of the pump pulse, one of the two materials is resonantly excited, whereas the polarization of the probe pulse can be optimized to selectively detect the charge transfer into the other material. This allows us to explore the interlayer hole transfer from the WSe₂ into the MoSe₂ layer and *vice versa*, which appears within a few hundred femtoseconds *via* hybridized intermediate states at the Γ-point. Our approach enables systematic investigations of the charge transfer in dependence of the rotational layer mismatch in TMD heterostructures.

Van-der-Waals coupled 2D materials feature fascinating opportunities for designing stacked heterostructures.[1,2] In particular, heterostructures of transition metal dichalcogenides (TMDs) have shown promise for various optoelectronic and valleytronic applications.[3,4] Several combinations of TMDs in a heterobilayer reveal a type-II band alignment resulting in spatially separated electron–hole pairs after optical excitation (so called charge-transfer or interlayer excitons).[5–12] Beside the choice of

New concepts

Heterostructures of transition metal dichalcogenides (TMD) feature a type-II band alignment which can separate photoexcited electrons and holes into different layers through ultrafast charge transfer and can host long-lived interlayer excitons due to their spatially indirect nature. While this charge transfer is essential for potential applications, the underlying mechanisms still remain elusive. The main drawbacks of previous approaches were insufficient time-resolution of the employed microscopy setups and deficiencies of linear optical spectroscopies to address individual layers of the heterostructure selectively. We introduce a new experimental concept for investigating ultrafast charge-transfer processes in TMD heterostructures by means of optical pump second-harmonic probe microscopy. Our technique combines the advantages of time-resolved optical second-harmonic generation (SHG) with an optical microscopy setup. On the one hand, the method allows for pump–probe experiments in μm small structures with a superior time-resolution. On the other hand, the tensorial nature of the second-order nonlinear susceptibility allows us to distinguish the response from differently oriented layers to elucidate directional interlayer charge transfer as demonstrated for a rotationally mismatched WSe₂/MoSe₂ heterostructure. Thus, by combining polarization- and time-resolved measurements, very clear and systematic experiments can be performed for a variety of heterostructures to correlate observed transient changes with the underlying structure.

the materials, the relative orientation of the stacked layers can affect the interlayer coupling and the properties of the interlayer excitons.[13–20] Rotational misfit between two TMD monolayers results in a corresponding rotation of the hexagonal Brillouin zones and momentum-mismatched interlayer excitations. Therefore, the stacking should considerably influence the ultrafast charge transfer as well as the interlayer recombination following an optical excitation. Accordingly, a distinct difference in the exciton recombination of coherently and randomly stacked MoS₂/WS₂ heterostructures has been observed.[21] Systematic measurements on MoS₂/WSe₂ heterostructures, however, exhibit strong variations of the charge-recombination lifetime from sample to sample but no clear correlation with the twist angle.[22] With respect to the ultrafast charge transfer, recent experimental studies

[a] *Fachbereich Physik, Philipps-Universität Marburg, Marburg D-35032, Germany.*
 E-mail: gerson.mette@physik.uni-marburg.de

[b] *Department of Mechanical Engineering, Columbia University, New York 10027, USA*

obtained surprisingly diverse results. For MoS_2/WSe_2 heterostructures, the initial charge transfer was reported to be faster than the experimental time resolution of 40 fs independent of the examined stacking angles.[22] In contrast, much slower transfer times of a few hundred femtoseconds and a significant increase for larger rotational mismatch were observed for a WS_2/WSe_2 interface.[23]

Thus, despite the recent progress in the study of ultrafast dynamics in TMD heterostructures, the underlying mechanism for the charge-transfer process still remains elusive.[24] In this work, we therefore introduce a new experimental concept for the investigation of ultrafast charge transfer in TMD heterostructures by means of time-resolved optical second-harmonic generation (SHG). Our SHG imaging microscopy technique can overcome the main drawbacks of previous experimental approaches which were insufficient time-resolution of the employed microscopy setups and deficiencies to address pump-induced changes in a particular layer of the heterostructure selectively. Thus, in the commonly used linear pump–probe spectroscopy the measured transient response consists of a superposition of monolayer and heterostructure contributions. Furthermore, charge transfer can appear in both directions simultaneously depending on the excitation energy. Here, we demonstrate for the example of a rotationally mismatched WSe_2/$MoSe_2$ heterostructure that directional ultrafast charge transfer between the layers becomes accessible. By tuning the photon energy of the pump pulse, we can resonantly excite one of the two materials, whereas the polarization of the probe pulse allows us to selectively detect the charge transfer in the other material. The observed hole transfer times differ considerably for the opposite directions: from the WSe_2 into the $MoSe_2$ layer (and *vice versa*) charge transfer appears within 610 ± 150 fs (210 ± 60 fs) as determined from our second-harmonic (SH) transients. Furthermore, our results indicate that the charge transfer takes place *via* hybridized intermediate states at the Γ-point.

The applied SHG imaging microscopy technique, illustrated in Fig. S1 of the ESI,† combines the advantages of time-resolved SHG with an optical microscopy setup. It allows pump–probe experiments with an ideal time-resolution only limited by the used laser system to explore ultrafast dynamical changes in µm small structures. Since the SHG process is described by a third-rank tensor in the electric-dipole approximation, it has been established as a sensitive optical probe of the crystal orientation in TMD monolayers[25–27] or for the stacking angle in heterostructures.[28] By combination of polarization- and time-resolved measurements, very clear and systematic measurements can be performed to correlate the observed transient changes in the SH response with the underlying structure. The studied heterostructure consists of two stacked TMD monolayers (WSe_2/$MoSe_2$) encapsulated between thick layers of hexagonal boron nitride (hBN) for environmental protection.[29] The heterostructure was fabricated by using a stamp of polydimethylsiloxane elastomer to stack the different materials consecutively, starting with the hBN top-layer, followed by the WSe_2 monolayer and the $MoSe_2$ monolayer. This stack was then finally put onto the hBN bottom-layer which was exfoliated

on SiO_2/Si(001). This polymer-free layer assembly enables fabrication of ultraclean interfaces without contamination of interfaces by polymer or solvent.[29,30] An optical microscopy image of the final stack is shown in Fig. 1(a). The various mono- and multilayer flakes in combination with observable cracks and wrinkles make a clear identification of the individual layers rather difficult. Therefore, Fig. 1(b) displays a detail of (a) with the individual WSe_2 and $MoSe_2$ layers highlighted with dashed and dotted lines, respectively. Thus, the actual WSe_2/$MoSe_2$ heterostructure region is visualized by the marked red area. Details about the structural characterization of the WSe_2/$MoSe_2$ heterostructure can be found in the ESI.†

Fig. 1(e) displays the second-harmonic response in dependence of the polarization ϕ of the 800 nm probe laser evaluated for the $MoSe_2$ monolayer (blue), the WSe_2 monolayer (green) and the WSe_2/$MoSe_2$ heterostructure (red) regions. As discussed above, we can utilize the rotational anisotropy of SHG in TMD monolayers to determine the crystal orientation of the individual flakes.[25–27] For *p*-polarized SH light and normal incidence of the probe beam, the polarizational anisotropy from the monolayers can be described by a $\cos(2\phi + 3\Psi)$-dependence, where $\phi = 0°$ corresponds to *p*-polarized incoming light and Ψ is the angle between the armchair direction of the crystal and the horizontal.[31] In our case of a small angle of incidence, the expected two-fold symmetry is broken and two pairs of maxima with different heights are observed.[31] From the corresponding fits (solid lines) to the polarization dependence of the monolayer flakes, the crystal orientations with respect to the horizontal are determined to be $2.1°$ and $34.4°$ for the WSe_2 and the $MoSe_2$ monolayer, respectively. From this, a stacking angle of $32.3°$ for the heterostructure can be deduced. By tuning the polarization of the probe laser to an intensity maximum of a specific monolayer, one can visualize the shape of the respective flake in the SHG microscopy image. As shown in Fig. 1(c) and (d), the SH images at polarization I and II nicely reproduce the contours of the $MoSe_2$ and the WSe_2 monolayer, respectively. The SH response of the individual monolayers clearly exhibits spatial inhomogeneity within each flake. In particular the intensity along the visible diagonal wrinkles marked by arrows in Fig. 1(a) is strongly reduced for both polarizations. Despite this spatial inhomogeneity of the absolute SH signal, the normalized pump-induced changes in the SH response are comparatively homogeneous as can be seen for example in Fig. 2(b).

In order to investigate the ultrafast charge transfer in the heterostructure, the pump-induced change of the SH response in dependence of the pump–probe delay is studied. At a probe polarization of 110°, decent SH intensity can be obtained from the heterostructure and both monolayers [*cf.* polarization III in Fig. 1(e)]. Time-resolved SHG measurements upon 593 nm excitation for this particular probe polarization are shown in Fig. 2. At this pump–photon energy (2.09 eV) the B-exciton of WSe_2 is resonantly excited.[32] Fig. 2(a) represents the averaged SH intensities of the heterostructure (red) as well as WSe_2 (green) and $MoSe_2$ (blue) monolayers in dependence of the pump–probe delay. The transients are normalized to the signal
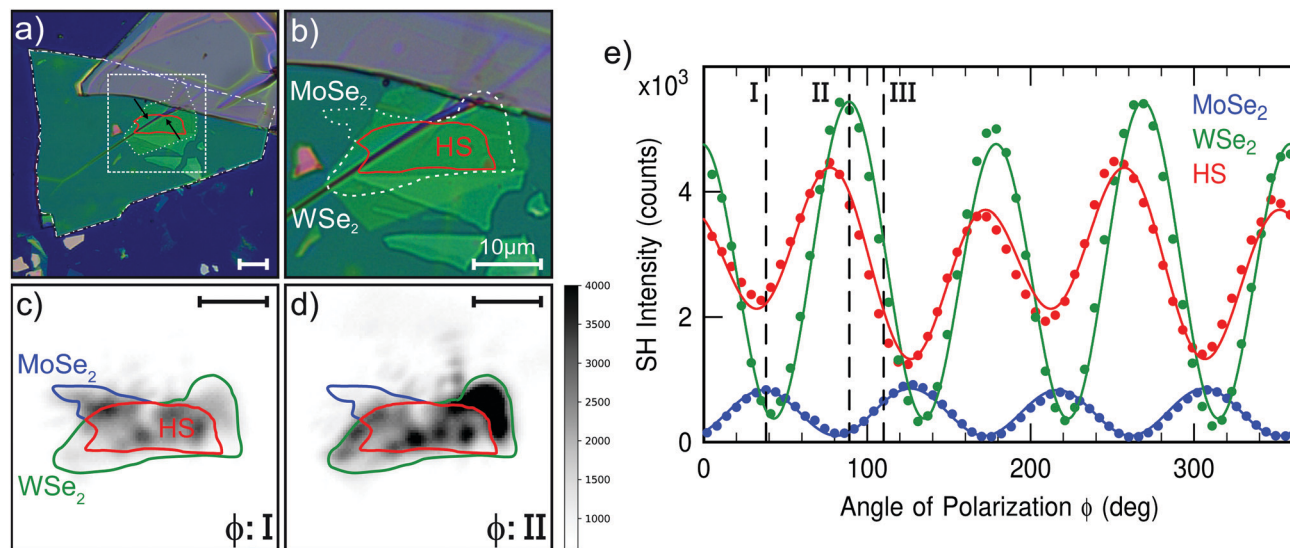
Fig. 1 (a) Optical microscopy image of the studied hBN/WSe$_2$/MoSe$_2$/hBN heterostructure. The dashed square represents the area shown in (b). Two visible wrinkles are marked by black arrows. Bottom and top hBN flakes are highlighted by dot–dashed and dotted lines, respectively. (b) Detail of the microscopy image in (a) highlighting the MoSe$_2$ and WSe$_2$ monolayer flake edges by dotted and dashed lines, respectively. The area within the red line represents the actual heterostructure. (c and d) SHG microscopy images for the polarization angles I and II which correspond to the intensity maxima of MoSe$_2$ and WSe$_2$ layers as shown in (e). The SH response agrees very well with the shape of the individual monolayer flakes as obtained from (b). All scalebars denote 10 μm. (e) Polarization dependent SH data evaluated from the MoSe$_2$ monolayer (blue), the WSe$_2$ monolayer (green) and the heterostructure (red) regions. Blue and green solid lines are the corresponding fits from which the crystal orientations of the MoSe$_2$ and WSe$_2$ monolayer are extracted. The polarization dependence of the heterostructure can be described by a superposition of the electric field components generated by the two monolayers (red solid line). The time–resolved SHG measurements shown in Fig. 2 were performed at probe polarization III.

at negative delay, *i.e.* before arrival of the pump–pulse, and therefore show the relative intensity changes in %. Normalized SHG microscopy images at two different pump–probe delays of 0 ps and 150 ps in Fig. 2(b) and (c) visualize the pump-induced changes within the different regions of the structure. A complete movie of the time-resolved SHG microscopy measurements can be found in the ESI.† The transient SH response of the hetero-structure exhibits significant differences when compared with the two monolayer signals. At temporal overlap, all three signals show a pump-induced ultrafast decrease of the SH intensity. After the optical excitation, the monolayer signals begin to recover immediately. In the heterostructure, however, there is a continued/delayed decrease in SH intensity occurring within several hundred femtoseconds after temporal overlap as shown in the inset of Fig. 2(a). Additionally, the subsequent relaxation of the heterostructure signal for large pump–probe delays is considerably slower than for the monolayers [Fig. 2(a)]. The transients of the heterostructure and the monolayers can be described by a bi-exponential decay. The corresponding lifetimes τ_1 and τ_2 as determined from a rate-equation model correspond to 5 ps and 32 ps for MoSe$_2$, 7 ps and 102 ps for WSe$_2$, and 19 ps and 203 ps for the heterostructure.

We attribute the fast initial decrease of the SH response to pump-induced changes in the second-order nonlinear suscepti-bility of the TMD monolayers, *e.g.*, due to depopulation of the valence band associated with the generation of intralayer excitons.[31] The subsequent progression as observable in the monolayer transients is then interpreted as exciton relaxation. In the heterostructure, ultrafast charge transfer between the

layers can lead to the generation of spatially separated inter-layer excitons. Accordingly, photoluminescence measurements on the very same heterostructure revealed characteristic emis-sion from interlayer excitons at 1.4 eV.[33] We therefore assign the continued decrease of the SH signal in the heterostructure within the first picosecond to the delayed formation of those charge-transfer excitons. Due to the reduced spatial overlap of electron- and hole-wavefunctions the interlayer excitons reveal an enhanced lifetime in accordance with our findings.[10]

The particular advantage of time-resolved second-harmonic generation to investigate the ultrafast charge transfer in TMD heterostructures is the intrinsic sensitivity of SHG on the crystal symmetry. By tuning the probe polarization we can, thus, enhance the sensitivity for a particular layer in the heterostruc-ture. Fig. 3 shows a polarizational anisotropy measurement of the SH response obtained from the heterostructure region upon optical excitation at 2.09 eV. At negative delays, *i.e.* without any influence of the pump beam, the same anisotropy as in Fig. 1 is observed for the heterostructure [*cf.* empty dots in Fig. 3(a)]. At a positive delay of 1.5 ps, however, the heterostructure signal is considerably reduced due to the fast initial decrease induced by the pump pulse [*cf.* filled dots in Fig. 3(a)]. Clearly, the absolute change of the SH response represented by the differ-ence of the two data sets [*cf.* crosses in Fig. 3(a)] exhibits a striking anisotropy, which becomes even more apparent when this absolute difference Δ is divided by the SH response at negative delays for each polarization angle. The resulting signal shown in Fig. 3(b) represents the relative pump-induced change δ of the SH signal which reveals a two-fold symmetric
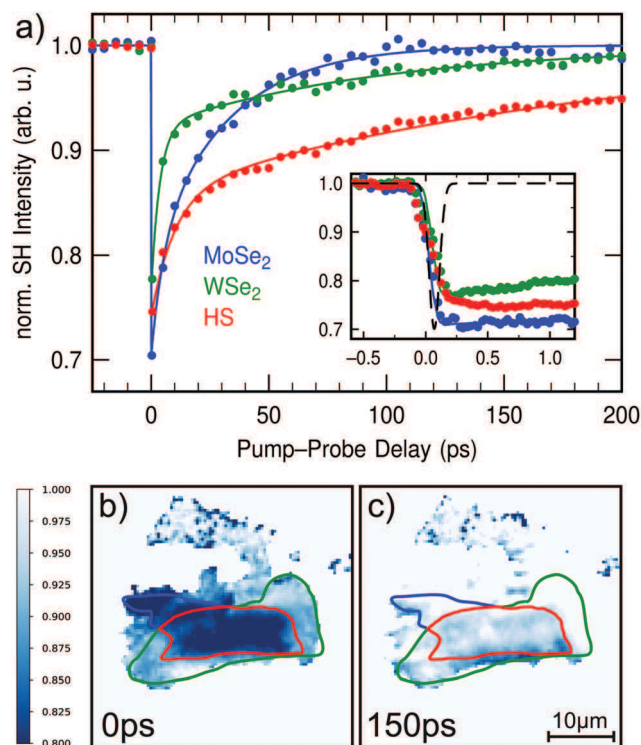
Fig. 2 Time-resolved SHG of the WSe₂/MoSe₂ heterostructure upon 2.09 eV optical excitation measured with probe polarization III. (a) Averaged SH intensities of the heterostructure and monolayer regions in dependence of the pump–probe delay. The inset shows the SH transients around temporal overlap measured with higher resolution. The cross correlation of the laser pulses corresponds to the black line. (b and c) Show normalized SH images at two different pump–probe delays of 0 ps and 150 ps, respectively. The SH response of the heterostructure exhibits significant differences compared with the two monolayer signals. At first, the three signals show a pump-induced ultrafast decrease of the SH intensity. However, while the monolayer signals begin to recover immediately after the optical excitation, a delayed decrease in SH intensity occurs in the heterostructure within several hundred femtoseconds after temporal overlap (inset). Furthermore, the subsequent relaxation of the heterostructure signal is considerably slower than for the monolayers.

Fig. 3 (a) Polarizational anisotropy measurements of the SH response obtained from the WSe₂/MoSe₂ heterostructure upon 2.09 eV excitation for two different pump–probe delays of −1.5 ps (empty dots) and +1.5 ps (filled dots), i.e. before and after temporal overlap. The difference of the two data sets (crosses) displays the absolute change Δ of the SH signal in dependence of the probe polarization. (b) The relative pump-induced change δ obtained by dividing the absolute change by the SH response at negative delays exhibits a striking anisotropy. The pump-induced decrease of the SH signal is found to vary between ≈20% and ≈75%.

polarization dependence with strong pump-induced decrease of the SH signal by up to 75%. Our finding implies that the size of the pump-induced effect depends on the polarization of the probe laser, which at first glance might seem implausible. Closer examination, however, shows that the greatest pump influence occurs exactly when the probe polarization is tuned to the intensity maximum of the MoSe₂ monolayer (cf. polarization I in Fig. 1 and 3). Corresponding SHG microscopy images shown in Fig. S3 of the ESI† furthermore illustrate that this strong polarization dependence on the pump-induced effect only appears in the heterostructure while the respective decrease in the monolayers is basically constant for all polarization angles. Our results thus reveal, that for resonant excitation of the WSe₂ monolayer at 2.09 eV, the detection efficiency for interlayer charge transfer is the highest when the probe polarization is most sensitive to the MoSe₂ monolayer. This allows us to selectively study directional differences of the ultrafast charge transfer in TMD heterostructures as we will show in the following.
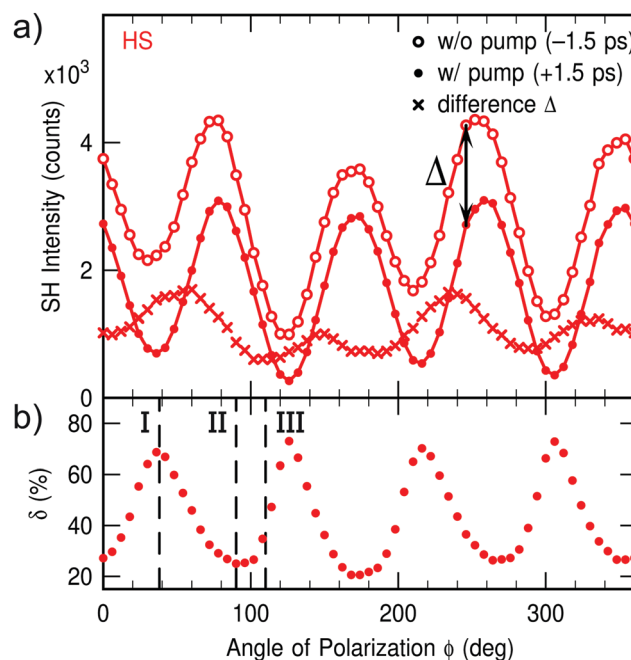
Applying our time- and polarization-resolved SHG microscopy technique in combination with pump–photon energy dependent measurements reveals a very clear picture of the ultrafast charge-transfer process in the WSe₂/MoSe₂ heterostructure. Fig. 4 shows time-resolved SH measurements for two pump–photon energies and two different probe polarizations. The chosen excitation energies are 2.09 eV (Fig. 4(a)) and 1.80 eV (Fig. 4(c)), resonant to the B-excitons of WSe₂ and MoSe₂, respectively. The polarizations are selected in order to enhance the sensitivity to an individual layer in the heterostructure. As shown in Fig. 4(a) for resonant excitation of WSe₂, the normalized SH signal of the heterostructure exhibits significant differences for the two probe polarizations. Thus, the delayed decrease of the SH signal which was associated with ultrafast interlayer charge transfer is observed only for probe polarization I sensitive to the MoSe₂ layer. In contrast, the heterostructure signal measured at polarization II exhibits no delayed decrease but very similar dynamics as obtained from the WSe₂ monolayer. The opposite behavior is found for resonant excitation of MoSe₂ shown in Fig. 4(c). Here, the delayed decrease in the heterostructure transient is only observed for probe polarization II. Surprisingly, the heterostructure transient for resonant excitation of the A-excitons of WSe₂ at 1.70 eV shows no indication of any charge transfer as shown in Fig. S4 and S5(a) in the ESI.† In contrast, non-resonant excitation of the MoSe₂ A-excitons
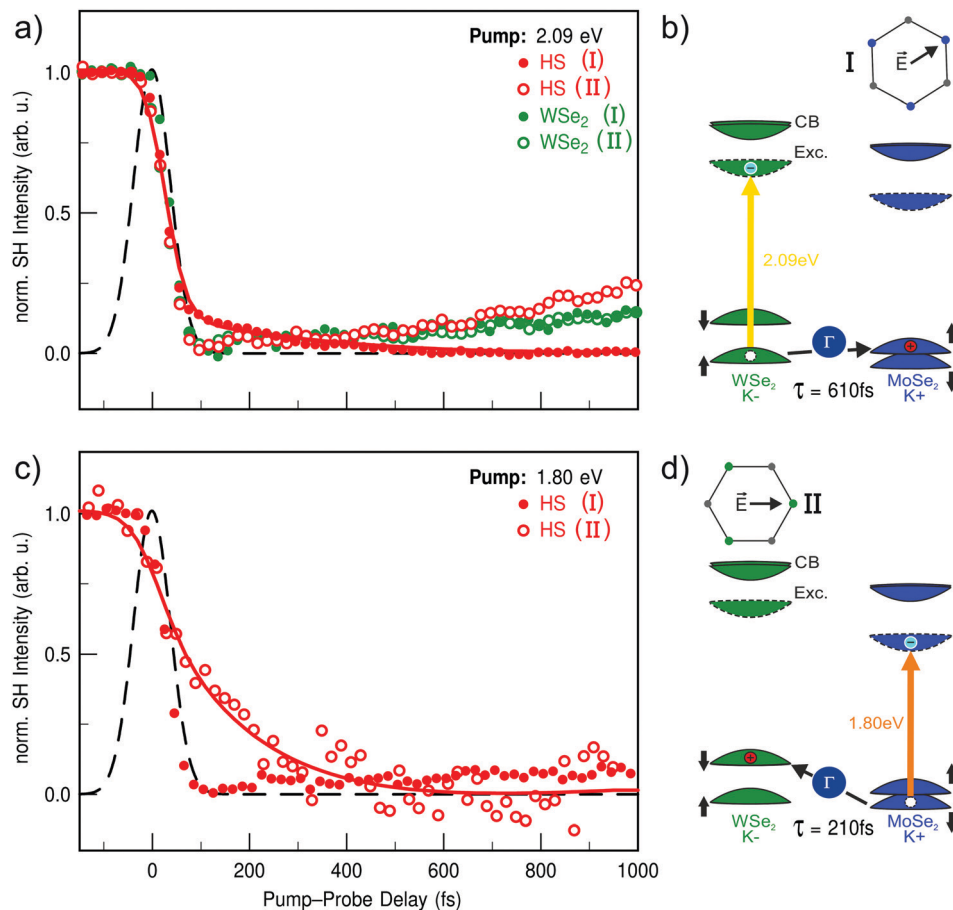
Fig. 4 Time-resolved SHG of the WSe$_2$/MoSe$_2$ heterostructure for two different pump–photon energies and two different probe polarizations. All SH transients are normalized, first to the signal at negative delays and then to the maximal pump-induced decrease for easier comparison of the dynamical changes. (a) SH transients for 2.09 eV pump–photon energy, resonant with the WSe$_2$ B-exciton. Filled and unfilled red data points correspond to the heterostructure signal with the probe polarization sensitive to MoSe$_2$ and WSe$_2$, respectively. A delayed decrease of the SH signal associated with ultrafast interlayer charge transfer is only observed for probe polarization I sensitive to the MoSe$_2$ layer. For probe polarization II, however, the transient of the heterostructure signal (unfilled) exhibits the very same dynamics as obtained from the WSe$_2$ monolayer (green). (b) Schematic drawing of the charge transfer into the MoSe$_2$ following resonant optical excitation of WSe$_2$ probed by polarization I. (c) SH transients like in (a) but for 1.80 eV pump–photon energy, resonant with the MoSe$_2$ B-exciton. Contrary to (a), the delayed decrease of the SH signal due to the interlayer charge transfer is only observed for probe polarization II sensitive to the WSe$_2$ layer. (d) Schematic drawing of the charge transfer into the WSe$_2$ following resonant optical excitation of MoSe$_2$ probed by polarization II. Solid lines in (a and c) correspond to a rate-equation fit to extract the interlayer transfer times. The cross correlation of the laser pulses is shown as a black line.

using the same photon energy shows a weak signature for charge transfer into the WSe$_2$ monolayer [cf. Fig. S5(b), ESI†]. In the case of resonant excitation of the WSe$_2$ A-exciton (1.68 eV), one would expect solely electron transfer into MoSe$_2$. Our results thus suggest, that this process is either not feasible or faster than our experimental time-resolution, estimated to be $\approx$ 15 fs (1/5th of the cross correlation FWHM). However, due to the large lattice mismatch of the layers in the studied heterostructure, the latter seems less likely. In order to describe the observed dynamics in the heterostructure quantitatively, we have applied a rate-equation model which takes a delayed filling by interlayer charge transfer into account as discussed in the ESI.† From this model, the transfer times for charge transfer from WSe$_2$ into MoSe$_2$ ($\tau_{WSe2 \rightarrow MoSe2}$ = 610 $\pm$ 150 fs) and vice versa ($\tau_{MoSe2 \rightarrow WSe2}$ = 210 $\pm$ 60 fs) were extracted. The corresponding fits are shown as solid lines in Fig. 4(a) and (c).

It has been proposed that intermediate states outside the K-valleys play a central role for the charge transfer in momentum-mismatched TMD heterostructures.[8,34–38] Band structure calculations show that conduction band states at the Σ-point shift energetically below the K-point minimum for certain stacking angles.[34] These states show strong hybridization of the individual wavefunctions of the monolayers,[34,35,37] and therefore enable a more efficient interlayer transfer. Further evidence for this process is given by two-photon photoemission measurements on bulk MoS$_2$, where ultrafast charge transfer to the Σ-point has been observed,[39] underlining the strong influence these states may have on the charge transfer in heterostructures. Since there is no experimental evidence for electron transfer from our energy-dependent measurements, we thus interpret the observed delayed filling as hole transfer between the layers assisted by hybridized states around the

Γ-point as illustrated in Fig. 4(b) and (d). Further evidence for this attribution is given by systematic measurements changing the pump–photon energy successively to explore the charge transfer from WSe_2 to $MoSe_2$ in more detail. Here, the pump-induced decrease of the SH intensity shows a clear resonance around the B-exciton energy of WSe_2 as shown in Fig. S4 of the ESI.† Furthermore, ultrafast charge transfer to $MoSe_2$ is only observed for excitation energies equal to or higher than the WSe_2 B-exciton resonance. From bandstructure calculations it is known that the Γ-point in the heterostructure is energetically located between the valence band maxima of the individual monolayers.[34,37] After their generation the excitons can access multiple relaxation routes. Within the monolayer, intra-valley scattering from B- to A-excitons is spin forbidden, but scattering from the K^+ to the K^- valleys is allowed. In direct competition to this process is the interlayer transfer observed in our measurements, e.g. from the $MoSe_2$ K^+ to WSe K^- valley or vice versa as illustrated in Fig. 4(b) and (d).

Similarly, our measurements also indicate ultrafast hole transfer from the $MoSe_2$ K^+ to WSe_2 K^+ valley after optical excitation of $MoSe_2$ A-excitons as shown in Fig. S5(b) of the ESI.† However, there is no experimental evidence for electron transfer from WSe_2 to $MoSe_2$ after resonant excitation of WSe_2 A-excitons [cf. Fig. S5(a), ESI†]. As discussed above, this result suggests that electron transfer in our heterostructure is either faster than the experimental time-resolution or not feasible due to the relatively large stacking angle. Of course, the charge transfer could also be so slow or inefficient, that its particular signature is superimposed by the faster monolayer dynamics. A recent study of a WS_2/WSe_2 heterostructure has observed electron transfer occurring within 200 fs and 1.2 ps after resonant excitation of WSe_2 A-excitons depending on the rotational mismatch.[23] While the order of magnitude compares reasonably well with our extracted transfer times for interlayer hole transfer, the question remains why electron transfer is not observable for our particular heterostructure. To further elucidate possible charge-transfer mechanisms in TMD heterostructures, stacking-dependent measurements have to be performed systematically for different material combinations. Our results demonstrate that the introduced SHG imaging microscopy technique is ideally suited for such systematic investigations of the ultrafast dynamics in momentum-mismatched TMD heterostructures. Those measurements would be further improved by an extended tuning range for the pump–photon energies to access all the exciton resonances of a certain heterostructure sample. In addition, a wavelength-tunable probe beam could further enhance the sensitivity for charge transfer into a certain material by making use of a resonant enhancement of the SH process.

In conclusion, we have introduced time-resolved SHG imaging microscopy for the investigation of ultrafast charge transfer in heterostructures of two-dimensional transition metal dichalcogenides. This method combines superior time-resolution with layer-sensitive detection and in situ determination of stacking angles. For a rotationally mismatched $WSe_2/MoSe_2$ heterostructure, our polarization- and energy-dependent measurements reveal

directional interlayer hole transfer from the WSe_2 into the $MoSe_2$ layer and vice versa, which appears in both cases within a few hundred femtoseconds. These results demonstrate that our approach enables systematic investigations of the charge transfer in dependence of the rotational layer mismatch in TMD heterostructures.

Methods

The experiments were performed under ambient conditions using 50 fs laser pulses generated by a femtosecond Ti:sapphire laser amplifier system (Coherent RegA 9050) operating at 800 nm center wavelength with a repetition rate of 150 kHz. The main part of the amplifier output (90%) is used to pump an optical parametric amplifier (OPA) operating in the visible range. The output of the OPA is compressed by a pair of LaFN28 Brewster prisms. The remaining part of the amplifier output (10%) is focused on the sample to probe the SH response. Both beams are nearly collinear and have an angle of incidence of about $18°$. After passing a 400 nm dielectric filter, the specular reflected SH response of the probe beam is imaged optically magnified by a camera lens (Nikon Nikkor, 1:1.4 ED, f = 50 mm) on an electron-multiplied CCD chip (Princeton Instruments ProEM-HS). Typical exposure times were between 20 and 60 seconds. The applied magnification was $M \approx 35$–40. The overall resolution of our imaging microscopy setup is better than 4 μm. The time-delay between pump and probe beam is varied by a motorized delay stage. The polarization of the pump and probe beam can be varied by means of $\lambda/2$-plates. The typically detected p-polarization of the second-harmonic light is separated by an analyzer. A combination of $\lambda/2$-plate and polarizer enable the continuous variation of the applied pump fluence in the range from 30–150 μJ cm^{-2} on the sample. The applied probe fluence was fixed to 220 μJ cm^{-2}. Long term measurements with these fluences applied did not exhibit any multishot damage.

Conflicts of interest

There are no conflicts to declare.

Acknowledgements

Notes and references

1 A. K. Geim and I. V. Grigorieva, Nature, 2013, 499, 419–425.
2 H. Lim, S. I. Yoon, G. Kim, A. R. Jang and H. S. Shin, Chem. Mater., 2014, 26, 4891–4903.
3 K. F. Mak and J. Shan, Nat. Photonics, 2016, 10, 216–226.

4 X. D. Xu, W. Yao, D. Xiao and T. F. Heinz, *Nat. Phys.*, 2014, **10**, 343–350.

5 E. V. Calman, L. H. Fowler-Gerace, D. J. Choksy, L. V. Butov, D. E. Nikonov, I. A. Young, S. Hu, A. Mishchenko and A. K. Geim, *Nano Lett.*, 2020, **20**, 1869–1875.

6 S. Ovesen, S. Brem, C. Linderalv, M. Kuisma, T. Korn, P. Erhart, M. Selig and E. Malic, *Commun. Phys.*, 2019, **2**, 23.

7 P. Rivera, H. Yu, K. L. Seyler, N. P. Wilson, W. Yao and X. Xu, *Nat. Nanotechnol.*, 2018, **13**, 1004–1015.

8 B. Miller, A. Steinhoff, B. Pano, J. Klein, F. Jahnke, A. Holleitner and U. Wurstbauer, *Nano Lett.*, 2017, **17**, 5229–5237.

9 J. R. Schaibley, P. Rivera, H. Y. Yu, K. L. Seyler, J. Q. Yan, D. G. Mandrus, T. Taniguchi, K. Watanabe, W. Yao and X. D. Xu, *Nat. Commun.*, 2016, **7**, 13747.

10 P. Rivera, J. R. Schaibley, A. M. Jones, J. S. Ross, S. F. Wu, G. Aivazian, P. Klement, K. Seyler, G. Clark, N. J. Ghimire, J. Q. Yan, D. G. Mandrus, W. Yao and X. D. Xu, *Nat. Commun.*, 2015, **6**, 6242.

11 H. Fang, C. Battaglia, C. Carraro, S. Nemsak, B. Ozdol, J. S. Kang, H. A. Bechtel, S. B. Desai, F. Kronast, A. A. Unal, G. Conti, C. Conlon, G. K. Palsson, M. C. Martin, A. M. Minor, C. S. Fadley, E. Yablonovitch, R. Maboudian and A. Javey, *Proc. Natl. Acad. Sci. U. S. A.*, 2014, **111**, 6198–6202.

12 X. P. Hong, J. Kim, S. F. Shi, Y. Zhang, C. H. Jin, Y. H. Sun, S. Tongay, J. Q. Wu, Y. F. Zhang and F. Wang, *Nat. Nanotechnol.*, 2014, **9**, 682–686.

13 P. Merkl, F. Mooshammer, S. Brem, A. Girnghuber, K.-Q. Lin, L. Weigl, M. Liebich, C.-K. Yong, R. Gillen, J. Maultzsch, J. M. Lupton, E. Malic and R. Huber, *Nat. Commun.*, 2020, **11**, 2167.

14 P. K. Gogoi, Y. C. Lin, R. Senga, H. P. Komsa, S. L. Wong, D. Z. Chi, A. V. Krasheninnikov, L. J. Li, M. B. H. Breese, S. J. Pennycook, A. T. S. Wee and K. Suenaga, *ACS Nano*, 2019, **13**, 9541–9550.

15 J. Kunstmann, F. Mooshammer, P. Nagler, A. Chaves, F. Stein, N. Paradiso, G. Plechinger, C. Strunk, C. Schüller, G. Seifert, D. R. Reichman and T. Korn, *Nat. Phys.*, 2018, **14**, 801–805.

16 W. T. Hsu, L. S. Lu, P. H. Wu, M. H. Lee, P. J. Chen, P. Y. Wu, Y. C. Chou, H. T. Jeng, L. J. Li, M. W. Chu and W. H. Chang, *Nat. Commun.*, 2018, **9**, 1356.

17 P. C. Yeh, W. Jin, N. Zaki, J. Kunstmann, D. Chenet, G. Arefe, J. T. Sadowski, J. I. Dadap, P. Sutter, J. Hone and R. M. Osgood, *Nano Lett.*, 2016, **16**, 953–959.

18 S. J. Zheng, L. F. Sun, X. H. Zhou, F. C. Liu, Z. Liu, Z. X. Shen and H. J. Fan, *Adv. Opt. Mater.*, 2015, **3**, 1600–1605.

19 K. H. Liu, L. M. Zhang, T. Cao, C. H. Jin, D. A. Qiu, Q. Zhou, A. Zettl, P. D. Yang, S. G. Louie and F. Wang, *Nat. Commun.*, 2014, **5**, 4966.

20 S. X. Huang, X. Ling, L. B. Liang, J. Kong, H. Terrones, V. Meunier and M. S. Dresselhaus, *Nano Lett.*, 2014, **14**, 5500–5508.

21 H. Heo, J. H. Sung, S. Cha, B. G. Jang, J. Y. Kim, G. Jin, D. Lee, J. H. Ahn, M. J. Lee, J. H. Shim, H. Choi and M. H. Jo, *Nat. Commun.*, 2015, **6**, 7372.

22 H. M. Zhu, J. Wang, Z. Z. Gong, Y. D. Kim, J. Hone and X. Y. Zhu, *Nano Lett.*, 2017, **17**, 3591–3598.

23 P. Merkl, F. Mooshammer, P. Steinleitner, A. Girnghuber, K. Q. Lin, P. Nagler, J. Holler, C. Schüller, J. M. Lupton, T. Korn, S. Ovesen, S. Brem, E. Malic and R. Huber, *Nat. Mater.*, 2019, **18**, 691–696.

24 C. H. Jin, E. Y. Ma, O. Karni, E. C. Regan, F. Wang and T. F. Heinz, *Nat. Nanotechnol.*, 2018, **13**, 994–1003.

25 Y. Li, Y. Rao, K. F. Mak, Y. You, S. Wang, C. R. Dean and T. F. Heinz, *Nano Lett.*, 2013, **13**, 3329–3333.

26 N. Kumar, S. Najmaei, Q. Cui, F. Ceballos, P. M. Ajayan, J. Lou and H. Zhao, *Phys. Rev. B: Condens. Matter Mater. Phys.*, 2013, **87**, 161403.

27 L. M. Malard, T. V. Alencar, A. P. M. Barboza, K. F. Mak and A. M. de Paula, *Phys. Rev. B: Condens. Matter Mater. Phys.*, 2013, **87**, 201401.

28 W.-T. Hsu, Z.-A. Zhao, L.-J. Li, C.-H. Chen, M.-H. Chiu, P.-S. Chang, Y.-C. Chou and W.-H. Chang, *ACS Nano*, 2014, **8**, 2951–2958.

29 G. H. Lee, X. Cui, Y. D. Kim, G. Arefe, X. Zhang, C. H. Lee, F. Ye, K. Watanabe, T. Taniguchi, P. Kim and J. Hone, *ACS Nano*, 2015, **9**, 7019–7026.

30 L. Wang, I. Meric, P. Y. Huang, Q. Gao, Y. Gao, H. Tran, T. Taniguchi, K. Watanabe, L. M. Campos, D. A. Muller, J. Guo, P. Kim, J. Hone, K. L. Shepard and C. R. Dean, *Science*, 2013, **342**, 614–617.

31 J. E. Zimmermann, B. Li, J. C. Hone, U. Höfer and G. Mette, *J. Phys.: Condens. Matter*, 2020, **32**, 485901.

32 A. F. Rigosi, H. M. Hill, Y. Li, A. Chernikov and T. F. Heinz, *Nano Lett.*, 2015, **15**, 5033–5038.

33 L. M. Schneider, S. Lippert, J. Kuhnert, O. Ajayi, D. Renaud, S. Firoozabadi, Q. Ngo, R. Guo, Y. D. Kim, W. Heimbrodt, J. C. Hone and A. Rahimi-Iman, *Nano-Struct. Nano-Objects*, 2018, **15**, 84–97.

34 P. K. Nayak, Y. Horbatenko, S. Ahn, G. Kim, J. U. Lee, K. Y. Ma, A. R. Jang, H. Lim, D. Kim, S. Ryu, H. Cheong, N. Park and H. S. Shin, *ACS Nano*, 2017, **11**, 4041–4050.

35 Y. Wang, Z. Wang, W. Yao, G. B. Liu and H. Y. Yu, *Phys. Rev. B*, 2017, **95**, 115429.

36 Q. J. Zheng, W. A. Saidi, Y. Xie, Z. G. Lan, O. V. Prezhdo, H. Petek and J. Zhao, *Nano Lett.*, 2017, **17**, 6435–6442.

37 A. T. Hanbicki, H. J. Chuang, M. R. Rosenberger, C. S. Hellberg, S. V. Sivaram, K. M. McCreary, I. Mazin and B. T. Jonker, *ACS Nano*, 2018, **12**, 4719–4726.

38 Q. J. Zheng, Y. Xie, Z. G. Lan, O. V. Prezhdo, W. A. Saidi and J. Zhao, *Phys. Rev. B*, 2018, **97**, 205417.

39 R. Wallauer, P. Marauhn, J. Reimann, S. Zoerb, F. Kraus, J. Güdde, M. Rohlfing and U. Höfer, *Phys. Rev. B*, 2020, **102**, 125417.

Electronic Supplementary Information

Directional ultrafast charge transfer in a WSe$_2$/MoSe$_2$ heterostructure selectively probed by time-resolved SHG imaging microscopy

J. E. Zimmermann[1], Y. D. Kim[2,3], J. C. Hone[2], U. Höfer[1], and G. Mette[1,*]

[1]Fachbereich Physik und Zentrum für Materialwissenschaften, Philipps-Universität, 35032 Marburg, Germany

[2]Department of Mechanical Engineering, Columbia University, New York 10027, United States

[3]Present Address: Department of Physics, Kyung Hee University, Seoul 02447, Republic of Korea

* corresponding author: gerson.mette@physik.uni-marburg.de
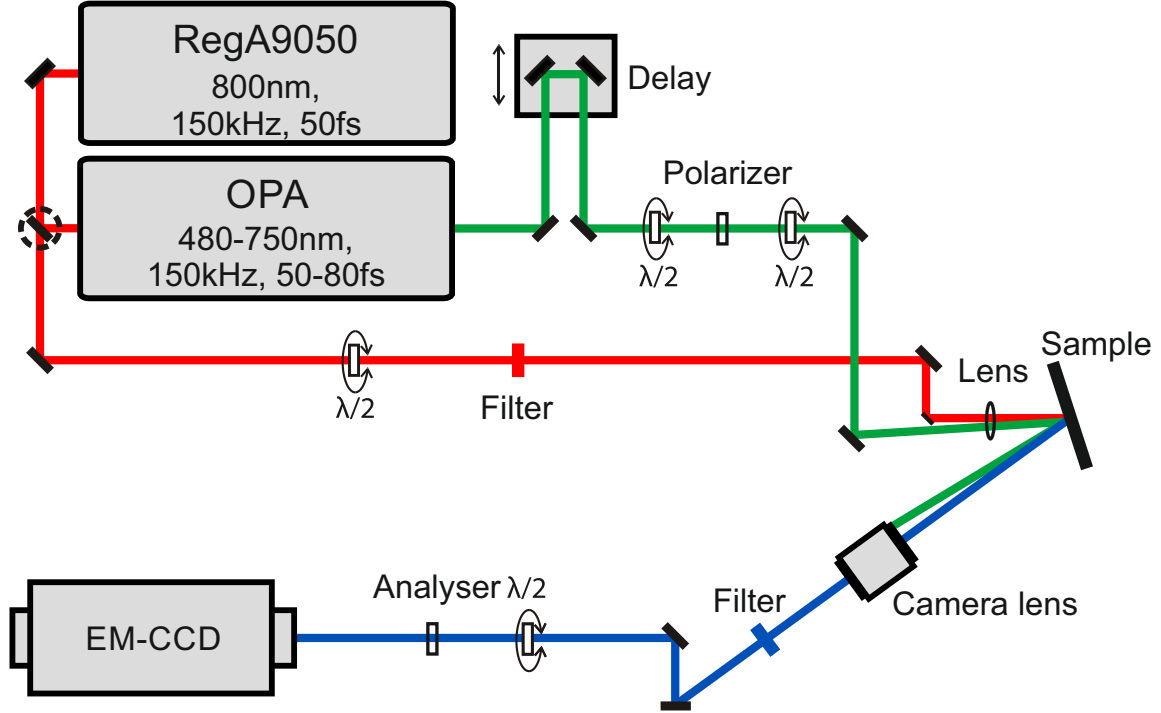
1 Experimental setup

Figure S1: **Experimental setup.** The fs-laser pulses are generated by a Ti:Sapphire laser amplifier system (RegA). The main part of the amplifier output (90 %) is used to pump an optical parametric amplifier (OPA) generating visible pump pulses. The remaining part of the amplifier output is sent through an RG715 filter and then used to probe the SH response. Pump and probe beam are focussed onto the sample nearly collinear under an angle of 18°. The specular reflected SH light of the probe pulse is imaged optically magnified by a camera lens through a FBH400-40 filter onto the CCD camera.

2 Sample characterization

The studied $hBN/WSe_2/MoSe_2/hBN$ heterostructure has been characterized in detail by optical spectroscopy in a previous work [1]. Fig. 11(a) of Ref. [1] shows the photoluminescence (PL) spectra of our sample at 300 K and 10 K. At room temperature, the PL spectrum obtained

from the heterostructure can be fitted with the sum of three Gaussian functions representing the A-exciton and trion of WSe_2 and the A-exciton of $MoSe_2$. At low temperature, the biexciton of WSe_2 and the trion of $MoSe_2$ can be observed additionally. Furthermore, PL lifetimes derived from transient photoluminescence are shown in Fig. 14 of Ref. [1] (last column). Raman spectra of the heterostructure at 300 K are given in Fig. 12 of Ref. [1] (sample 6). Three Raman modes are observed which can be attributed to WSe_2 A_g^1 and E_{2g}^1 and $MoSe_2$ E_{2g}^1 modes. These Raman and PL measurements of Ref. [1] confirm that the $hBN/WSe_2/MoSe_2/hBN$ heterostructure studied in the present work by time-resolved SHG microscopy represents a heterobilayer of WSe_2 and $MoSe_2$.

In addition, the heterostructure has been characterized by atomic force microscopy (Agilent SPM 5500) operated under ambient conditions in tapping mode. The AFM image and different topographic line scans are shown in Fig. S2.
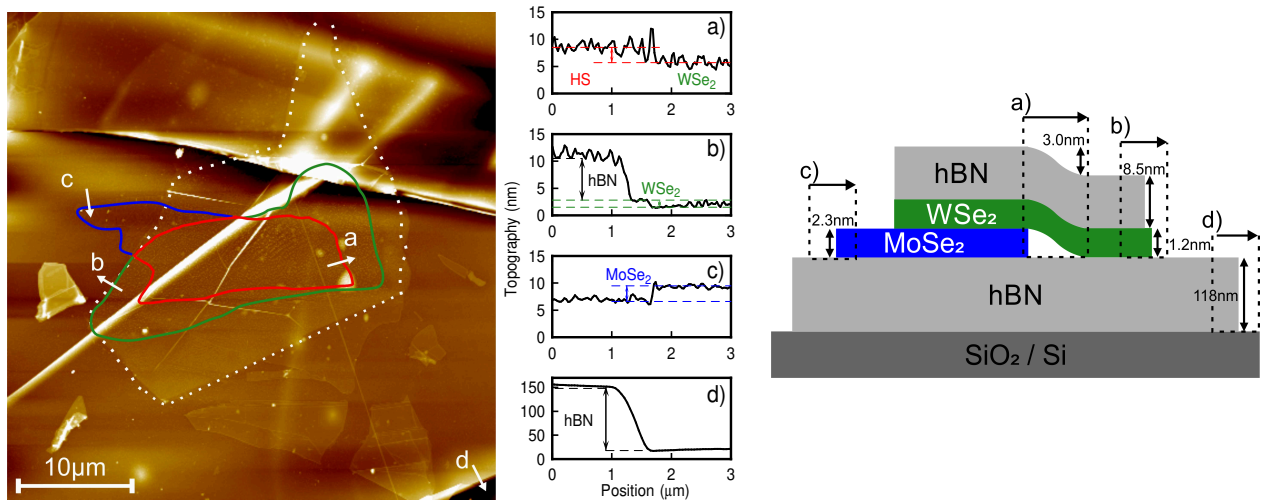

Figure S2: **AFM measurements.** Left: AFM image of the studied $hBN/WSe_2/MoSe_2/hBN$ sample with the heterostructure (HS) and the WSe_2 and $MoSe_2$ monolayer regions highlighted by red, green and blue color, respectively. Center: Topographic line scans along the white arrows labelled as (a) - (d) in the AFM image. Right: Schematic side view of the heterostructure illustrating the particular regions of the different line scans and the extracted height differences.
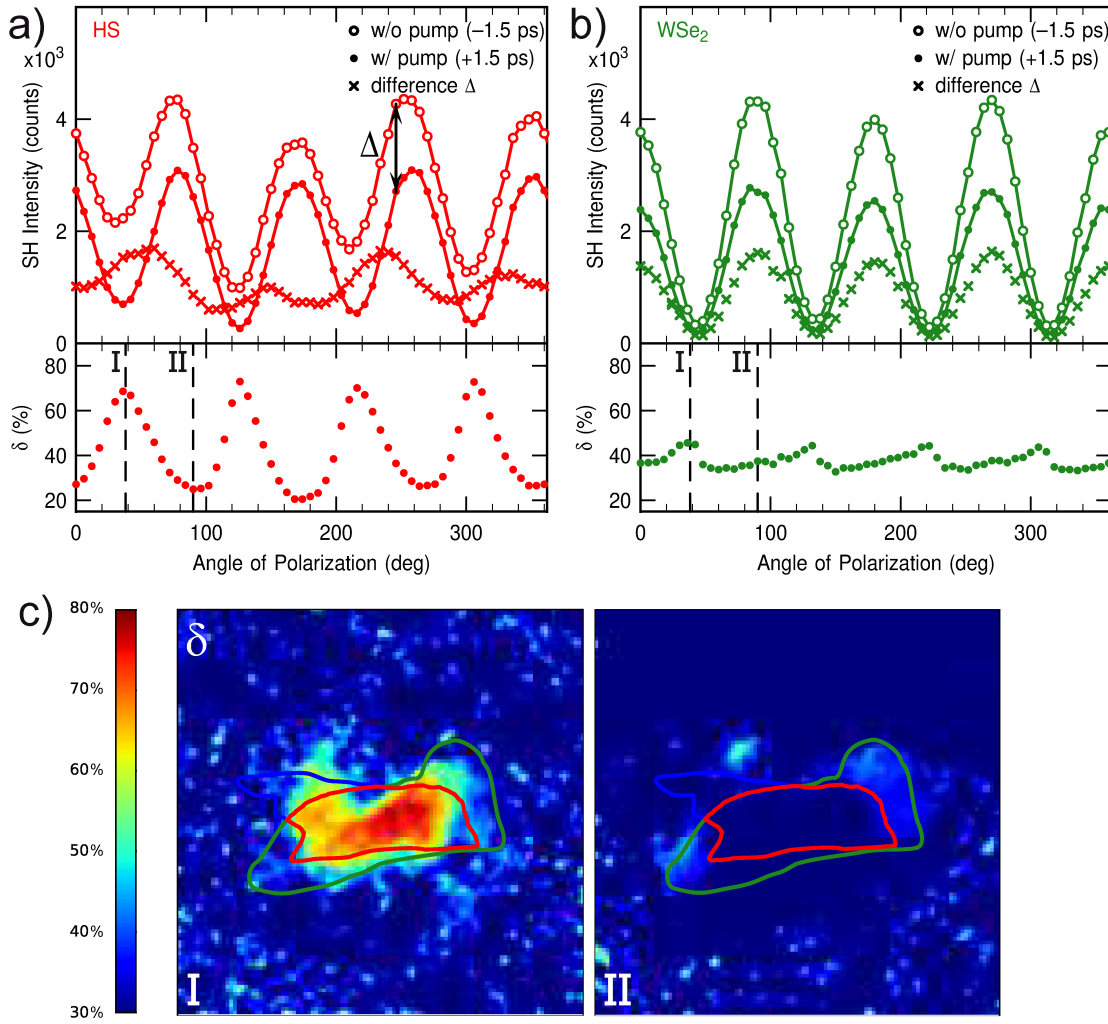
3 Supplemental time-resolved data

Figure S3: **Polarizational SHG anisotropy upon optical excitation.** (a) Polarization dependent measurements of the SH response obtained from the WSe$_2$/MoSe$_2$ heterostructure upon 2.09 eV excitation for two different pump-probe delays of -1.5 ps (empty dots) and +1.5 ps (filled dots) as already shown in Fig. 3 of the maintext. The difference of the two data sets (crosses) displays the absolute change of the SH signal (Δ) in dependence of the probe polarization. Dividing the absolute signal change by the SH response at negative delays exhibits a striking anisotropy of the relative change of the SH signal (δ) varying between $\approx 20\%$ and $\approx 75\%$ of pump-induced decrease. (b) Direct comparison of the corresponding evaluation for the WSe$_2$ monolayer reveals the absence of the strong anisotropy present in the heterostructure. Instead an almost isotropic pump-induced decrease of $\approx 40\%$ is observed. (c) Images of the spatial distribution of δ for two different polarizations (I and II). The strong pump-induced change is clearly localized within the heterostructure region.
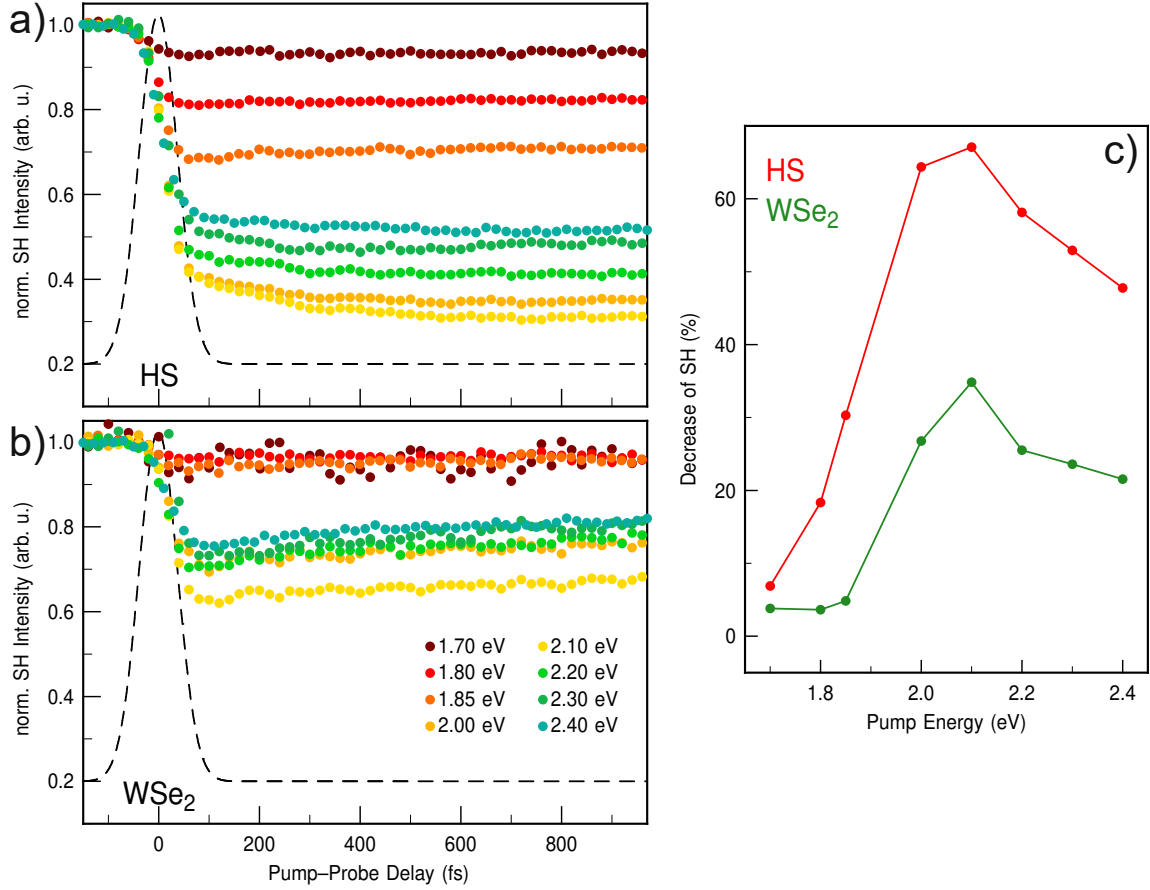
4

Figure S4: **Time-resolved SHG in dependence of the pump-photon energy.** The pump-photon energy is varied between $1.70-2.40\,\text{eV}$, the SH response is measured with probe polarization I most sensitive to the $MoSe_2$ layer. (a) Averaged SH intensities of the heterostructure region in dependence of the pump-probe delay. The cross correlation of the laser pulses corresponds to the black line. (b) Corresponding SH transients of the WSe_2 monolayer region. (c) Extracted decrease of the SH signal in temporal overlap in dependence of the pump-photon energy. For both, the heterostructure and the WSe_2 monolayer, a clear resonant behavior can be observed, which matches well with the B-exciton energy of WSe_2. The SH response of the heterostructure exhibits significant differences compared to the WSe_2 monolayer signal as soon as the threshold energy of $2.00\,\text{eV}$ is reached. For pump-photon energies $\geq 2.00\,\text{eV}$, the form of the SH transient changes substantially and reveals a delayed intensity decrease as discussed further in the main text.
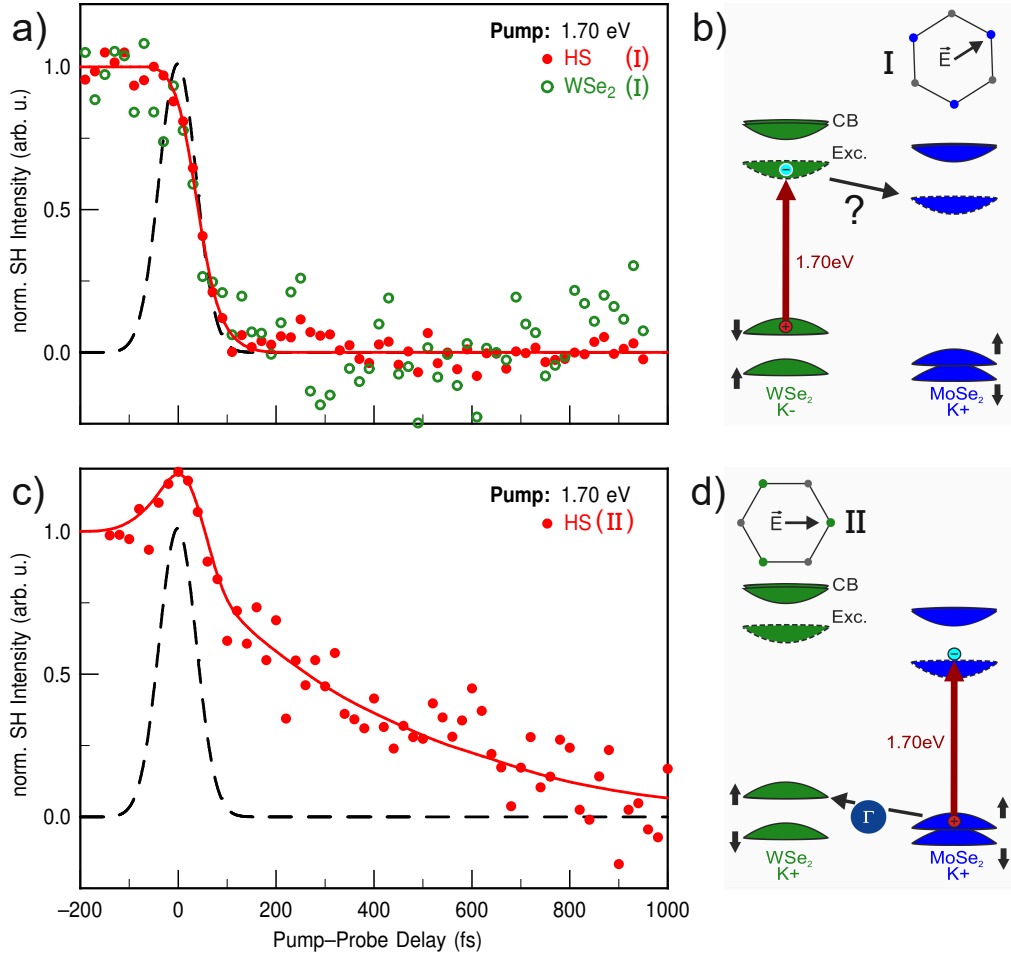
5

Figure S5: **Time-resolved SHG for photoexcitation with 1.7 eV.** The chosen pump-photon energy is resonant with the WSe_2 A-excitons (1.68 eV) and non-resonant with the $MoSe_2$ A-excitons (1.56 eV). (a) SH transients of the heterostructure (red) in comparison with the respective WSe_2 signal (green) for probe polarization I sensitive to $MoSe_2$. A delayed decrease of the heterostructure signal associated with ultrafast electron transfer from WSe_2 to $MoSe_2$ is not observed. (b) Schematic drawing of the potential electron transfer to $MoSe_2$ after resonant optical excitation of WSe_2 A-excitons. (c) SH transient of the heterostructure as in (a) for probe polarization II sensitive to WSe_2. Direct comparison with the heterostructure signal in a) indicates a delayed decrease due to interlayer hole transfer. (d) Schematic drawing of the hole transfer to WSe_2 after non-resonant optical excitation of $MoSe_2$ A-excitons. Please note, that the noise level of this measurement is comparatively large, since it was performed at the tuning limit of our laser setup. Solid red lines are a guide to the eye. The cross correlation of the laser pulses is shown as a black line. The increase of the SH intensity around temporal overlap for polarization II is caused by an interference of pump and probe beam due to their similar wavelength and polarisation.

6

4 Rate-equation model for interlayer charge transfer

To describe the relaxation dynamics visible in the SH transients a rate-equation approach is used. Here, a population is generated from two ground states by convolution with the pump pulse. This change in charge-carrier density is then in turn monitored by the probe pulse. For the delayed decrease seen in the heterostructure transients, the energetically higher lying state $|2>$ couples to the lower lying state $|1>$ further filling it with the time constant τ_{transfer}. This repopulation manifests as a further reduction of SH intensity even after the pump pulse has fully subsided as can be seen in Fig. 4 of the main text. The dynamics can therefore be described by:

$$\frac{\text{dN}_1}{\text{dt}} = -\text{N}_1\lambda_1 + \text{N}_2\lambda_{\text{transfer}} \tag{1}$$

where N_1 is the population of state $|1>$, N_2 is the population of state $|2>$ and λ_1 the decay rate of state $|1>$. For an easier understanding Fig. S6 illustrates the transfer process for the example of the $\text{MoSe}_2 \rightarrow \text{WSe}_2$ hole transfer.
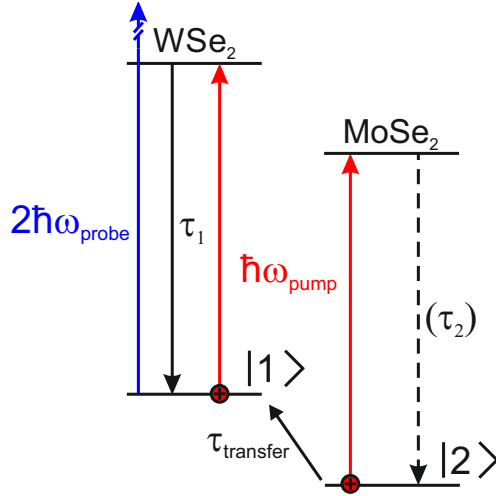

Figure S6: **Illustration of the decay mechanism.** In the shown example MoSe_2 is pumped resonantly after which the holes scatter into the VBM of WSe_2. The applied model neglects the decay τ_2 for the excited states in MoSe_2 since it occurs on a slower timescale.

References

[1] L. M. Schneider, S. Lippert, J. Kuhnert, O. Ajayi, D. Renaud, S. Firoozabadi, Q. Ngo, R. Guo, Y. D. Kim, W. Heimbrodt, J. C. Hone, and A. Rahimi-Iman, Nano-Structures & Nano-Objects **15**, 84 (2018).

Article III

Ultrafast Charge-Transfer Dynamics in Twisted MoS$_2$/WSe$_2$ Heterostructures

Jonas E. Zimmermann, Marleen Axt, Fabian Mooshammer, Philipp Nagler, Christian Schüller, Tobias Korn, Ulrich Höfer, and Gerson Mette*

Cite This: https://doi.org/10.1021/acsnano.1c04549

Read Online

ACCESS | Metrics & More | Article Recommendations | SI Supporting Information

ABSTRACT: Two-dimensional transition metal dichalcogenides offer a fascinating platform for creating van der Waals heterojunctions with exciting physical properties. Because of their typical type-II band alignment, photoexcited electrons and holes can separate *via* interfacial charge transfer. Furthermore, the relative crystallographic alignment of the individual layers in these heterostructures represents an important degree of freedom. Based on both effects, various fascinating ideas for applications in optoelectronics and valleytronics have been suggested. Despite its utmost importance for the design and

efficiency of potential devices, the nature and the dynamics of ultrafast charge transfer are not yet well understood. This is mainly because the charge transfer can be surprisingly fast, usually faster than the temporal resolution of previous experimental approaches. Here, we apply time- and polarization-resolved second-harmonic imaging microscopy to investigate the charge-transfer dynamics for three MoS$_2$/WSe$_2$ heterostructures with different stacking angles at a previously unattainable time resolution of ≈10 fs. For 1.70 eV excitation energy, electron transfer from WSe$_2$ to MoS$_2$ is found to depend considerably on the stacking angle with the fastest transfer time observed to be as short as 12 fs. At 1.85 eV excitation energy, ultrafast hole transfer from MoS$_2$ to hybridized states at the Γ-point and to the K-points of WSe$_2$ has to be considered. Surprisingly, the corresponding decay dynamics show only a minor stacking-angle dependence indicating that radiative recombination of momentum-space indirect Γ-K excitons becomes the dominant decay route for all samples.

KEYWORDS: *time-resolved second-harmonic generation, transition metal dichalcogenides, ultrafast charge transfer, heterostructure, pump−probe experiment, nonlinear optical spectroscopy, stacking angle*
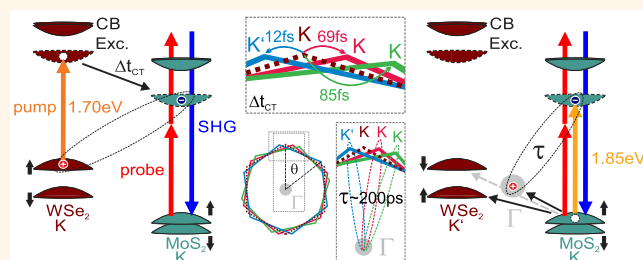
T wo-dimensional van der Waals materials offer a plethora of opportunities for the design and investigation of stacked heterostructures (HS).[1,2] In particular, heterostructures of transition metal dichalcogenides (TMD) have revealed fascinating properties stimulating fundamental and applied research in the field of optoelectronics and valleytronics.[3,4] Many combinations of different TMD layers form type-II heterojunctions[5] which enables efficient charge separation and results in spatially separated electron−hole pairs following an optical excitation (so-called charge-transfer or interlayer excitons).[6−17] Due to their van der Waals coupled nature, structures with arbitrary stacking angles can be designed and manufactured. The relative orientation of the TMDs, in turn, influences the coupling between the layers and therefore charge transfer, recombination, and other properties of the interlayer excitons.[17−24] However, recent experimental studies investigating the influence of the stacking on the ultrafast charge transfer obtained surprisingly diverse results. For MoS$_2$/WSe$_2$ heterostructures, charge transfer has been reported to be faster than the experimental time

resolution of 40 fs independent of the examined stacking angles.[26] In contrast, much slower charge-transfer times of a few hundred femtoseconds and a significant increase for larger rotational mismatch were observed for WS$_2$/WSe$_2$.[27] In general, previous time-resolved studies on TMD heterostructures have focused primarily on the decay dynamics of generated interlayer excitons and gave only upper limits for the charge-transfer times due to their limited time resolution.[16,26,28−32] Theoretical studies also have considered the influence of the stacking on the charge-transfer process but usually only for a few selected stacking configurations.[19,21,27,32−34] Thus, the underlying mechanism for the
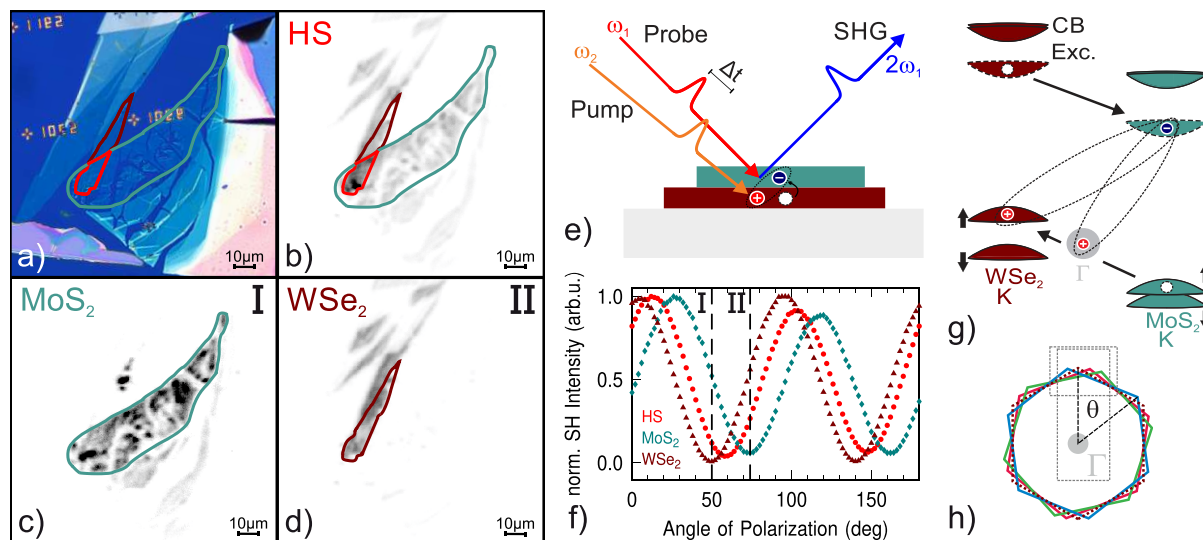
Figure 1. (a) Optical microscopy image of the studied misaligned (16°) MoS$_2$/WSe$_2$ sample. MoS$_2$ and WSe$_2$ monolayers as well as the heterostructure regions are highlighted with teal, maroon, and red outlines, respectively. (b)−(d) SH images measured with three different probe polarizations sensitive to both monolayers (b), exclusively to MoS$_2$ (c) or WSe$_2$ (d), respectively. (e) Sketch of the pump−probe experiment for an example of resonant optical excitation in WSe$_2$ and selective SHG detection of potential charge transfer in MoS$_2$. (f) Polarization-dependent SHG of the misaligned sample shown in (a) evaluated for MoS$_2$ (teal) and WSe$_2$ (maroon) monolayers and the heterostructure (red). The dashed lines mark the polarization angles I and II applied for the SH images shown in (c) and (d). (g) Schematic band alignment of MoS$_2$/WSe$_2$ showing the individual K-points of both materials and the hybridized Γ-point.[17] The dashed ellipses mark the previously reported K−K and Γ−K interlayer excitons.[17,25] (h) Corresponding hexagonal Brillouin zones of the studied heterostructures for the three stacking angles 9° (red), 16° (green), and 52° (blue). The colored solid lines represent the respective MoS$_2$ Brillouin zones rotated relative to the WSe$_2$ (dotted maroon line). The dotted rectangles delineate the regions of interest highlighted in Figures 2(d) and 3(d) respectively.

charge-transfer process for different van der Waals hetero-structures still remains elusive, and there are several unresolved questions concerning the influence of the stacking config-uration on the ultrafast interlayer charge transfer. We have recently shown the capabilities of the experimental method of time- and polarization-resolved second-harmonic (SH) imag-ing microscopy giving us direct access to the directional ultrafast charge transfer in a rotationally mismatched WSe$_2$/MoSe$_2$ heterostructure.[8] In particular, our technique allows for pump−probe experiments in μm-sized regions of TMD heterostructures with a time resolution estimated from the cross-correlation of pump and probe pulse to be ≈10 fs not accessible in previous studies.

Here, we employ this approach to examine the charge-carrier dynamics in MoS$_2$/WSe$_2$ heterostructures with different stacking angles. The three MoS$_2$/WSe$_2$ samples studied in the present work had been examined beforehand in a systematic study by Kunstmann et al.[17] There it has been shown that for all stacking configurations photoluminescence from momentum-space indirect Γ-K interlayer excitons is visible after optical excitation with 532 nm (2.33 eV) photons. It is therefore established that for excitation energies significantly exceeding the respective band gaps interlayer charge transfer occurs and that a part of the excited charge carriers recombine radiatively via a Γ-K transition. The interlayer exciton energy was observed to shift slightly as a continuous function of the twist angle over the range of 50 meV with a maximum near 30° and minima at 0° and 60°.[17] The intralayer A-exciton and trion energies of MoS$_2$ and WSe$_2$, in contrast, have not shown a distinct dependence on the interlayer twist but only a minor 25 meV shift in energy due to the modified dielectric environment in the heterobilayers.[17] Recently, also momentum-space direct K−K photolumines-

cence at ≈1.0 eV has been observed for well-aligned MoS$_2$/WSe$_2$ heterostructures.[25] In the present study, we want to elucidate the corresponding ultrafast dynamics in dependence of the stacking angle for three selected stacking angles: 9° (referred to as quasi-3R), 52° (quasi-2H), and 16° (misaligned).

RESULTS AND DISCUSSION

Our method of choice is polarization- and time-resolved second-harmonic imaging microscopy. By careful selection of the polarization angle of the 800 nm (1.55 eV) probe light, we are able to extract changes in the nonlinear susceptibility of individual monolayers inside the TMD heterostructures. For TMD monolayers, the pump-induced changes of the SH response upon resonant optical excitation of intralayer excitons have been shown to be closely correlated to the observed exciton dynamics in linear optical spectroscopy.[35] In the case of TMD heterostructures, our pump−probe experiments schematically sketched in Figure 1(e) allow us to distinguish the transient SH response from differently oriented layers by polarization-dependent measurements. By changing the pump-photon energy in addition, our technique can reveal a very clear picture of the ultrafast charge-transfer process.[8] The three studied MoS$_2$/WSe$_2$ samples were mechanically exfoliated and transferred onto a SiO$_2$/Si(001) substrate as described in ref 17. Figure 1(a)−(d) compares an optical microscopy image of one of the studied samples with respective images obtained for different probe polarizations with our SH imaging microscope. Due to the inherent structural sensitivity of second-harmonic generation (SHG), we are able to directly identify the different monolayer regions and their overlap to determine the position of the heterostructure.

Figure 1(f) displays the normalized SH response in dependence of the polarization of the probe laser evaluated for the monolayer and heterostructure regions. From these measurements, the crystal orientations in relation to the lab coordinates can be determined. The probe polarization for our time-resolved measurements is then chosen to maximize the sensitivity for the MoS_2 layer by fully suppressing the SH contribution of WSe_2 (polarization I). For 1.70 eV pump-photon energy, intralayer A-excitons of WSe_2 are resonantly excited.[36,37] Figure 2(a) shows the corresponding SH
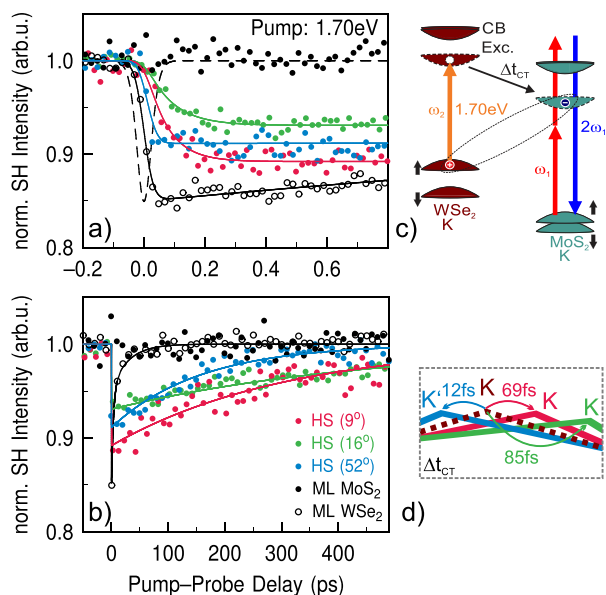

Figure 2. Time-resolved SHG of the MoS_2/WSe_2 heterostructures with three different stackings. (a,b) SH transients upon 1.70 eV resonant excitation of the WSe_2 intralayer A-exciton for a subpicosecond and an extended range of pump−probe delays, respectively. Colored data points represent the heterostructure samples, and black data points represent the corresponding monolayer dynamics as denoted in (b). Solid lines correspond to rate-equation fits. Filled (unfilled) data points are measured at probe polarization I (II), sensitive to MoS_2 (WSe_2). The dashed line in (a) represents the simulated cross-correlation of the laser pulses. (c) Sketch of the band alignment for MoS_2/WSe_2. Ultrafast charge transfer to MoS_2 after resonant optical excitation of WSe_2 results in the formation of K−K interlayer excitons (dashed ellipse). SH detection selectively probes the transient response of MoS_2. (d) Cutout from the Brillouin zone illustrating the electron transfer for the respective samples.

transients of the heterostructures selectively detected by probing the ultrafast nonlinear response of the MoS_2 layer in direct comparison with the respective transients obtained from the individual monolayers. All SH transients have been normalized to the signal at negative delays. As expected, the MoS_2 monolayer transient (filled black data) shows no pump-induced change since the excitation energy is below its A-exciton resonance. In contrast, the SH intensity of the MoS_2 layers of the heterostructures exhibits a clear modulation as a function of the pump−probe delay time. We observe a rapid decrease and a subsequent slower recovery. Since any direct excitation of the MoS_2 can be excluded from the monolayer results, we can therefore assign the observed dynamics in the heterostructures to ultrafast electron transfer to MoS_2 after optical excitation of WSe_2 as sketched in Figure 2(c). This

attribution is also corroborated by the delayed onset of the heterostructure signals in relation to the WSe_2 monolayer response and by the ongoing/delayed decrease of the SH intensity, which extends even beyond the duration of the pump pulse (cf. dashed line, simulated cross-correlation).

While there is clear evidence for charge transfer in all heterostructure samples, the observed ultrafast dynamics differ considerably for the three different stackings. Apparently, the fastest electron transfer can be found for the quasi-2H stacked sample (blue data), followed by the quasi-3R (red data) and the misaligned sample (green data). This is confirmed quantitatively by a rate-equation model consisting of two coupled differential equations in which one energetically higher lying state N_0 is filled by a Gaussian pump pulse $G(A, \sigma, t_0)$ and then subsequently populates the lower lying state N_1 with a transfer time Δt_{CT}.

$$\frac{dN_0}{dt} = G(A, \sigma, t_0) - \frac{N_0}{\Delta t_{CT}} \qquad (1)$$

$$\frac{dN_1}{dt} = \frac{N_0}{\Delta t_{CT}} - \frac{N_1}{\tau_{HS}} \qquad (2)$$

The temporal overlap t_0 and the temporal width $\sigma = \text{FWHM}/(2\sqrt{2 \ln 2})$ of the Gaussian source term are extracted from the respective cross-correlation. Therefore, three fit parameters remain: the amplitude A of the Gaussian pulse, the transfer time Δt_{CT}, and the lifetime of the filled state τ_{HS}. The extracted transfer time Δt_{CT} for the quasi-3R and the misaligned sample are comparable with values of 69 ± 10 fs and 85 ± 9 fs, respectively, whereas the transfer time for the quasi-2H stacked sample is more than five times faster (12 ± 4 fs). This disparity might be surprising since the variation of the lattice separation between the layers, which has a central influence on the tunneling probability,[28] is negligible between 2H- and 3R-stacking.[17] However, the wave function overlap between the layers plays an important role for the charge transfer across the interface as well as for the subsequent recombination dynamics.[19] Accordingly, wave function calculations for the interfacial plane in TMD heterostructures have shown strong differences for 3R- and 2H-stacking,[34] which then, in turn, can indeed influence the dynamics.[33]

Consequently, we conclude that the faster interlayer electron transfer for the quasi-2H stacked sample is caused by the stronger interlayer interaction of the involved monolayer states at the K-point. In accordance, the observed recombination dynamics shown in Figure 2(b) also differ significantly for the three heterostructures as determined from the individual lifetimes τ_{HS} extracted by the rate-equation fits. The misaligned sample shows the longest lifetime (467 ± 16 ps), the quasi-3R stacked sample shows an intermediate lifetime (309 ± 12 ps), and the quasi-2H stacked sample shows the shortest lifetime (158 ± 10 ps). The enhanced lifetime for the misaligned sample could be an indication for the absence of the radiative decay channel as it was reported recently.[25] The difference in lifetime between quasi-2H and quasi-3R can then be explained by the same reasoning as the enhanced transfer. Since the charge transfer via a phonon-assisted tunneling process can be amplified by the spatial overlap of the involved wave functions,[6,28] the same should hold for the reversed process of interlayer exciton recombination: A stronger spatial coincidence facilitates the recombination resulting then in a reduced lifetime. Please note that all three heterostructure

lifetimes are considerably extended in comparison to the lifetime observed for the WSe$_2$ monolayer. The WSe$_2$ intralayer recombination can be described by a biexponential recovery behavior with much shorter lifetimes of τ_1 = 3.5 ps and τ_2 = 30 ps. The much slower interlayer recombination observed for the heterostructure signals is in perfect agreement with our interpretation, since the spatially indirect nature of interlayer excitons leads to a strong increase of their lifetimes in comparison to intralayer excitons.[14,31]

In the following, we would like to address open questions concerning the ultrafast hole transfer and the particular influence that hybridized states at the Γ-point have on charge transfer and recombination. In order to elucidate these processes, the pump-photon energy is tuned to 1.85 eV for resonant optical excitation of MoS$_2$ intralayer A-excitons.[36,37] While at this photon energy both materials are excited, the generated exciton density in MoS$_2$ (5.3 · 10^{12}/cm^2) is about five times larger than in WSe$_2$ (9.3 · 10^{11}/cm^2), as calculated based on energy-dependent absorption of the two layers (see the Methods section). Thus, the pump-induced effects in WSe$_2$ are not negligible; however, the dynamic response measured in MoS$_2$ is mainly dominated by its inherently generated charge carriers. Figure 3 shows the same time regimes as before using identical colors for the different structures, but now the systems are pumped at 1.85 eV. By comparing the dynamics of Figures 2(a) and 3(a), striking differences become obvious: First of all, upon 1.85 eV photoexcitation, the pump-induced effects now already start to occur precisely at temporal overlap
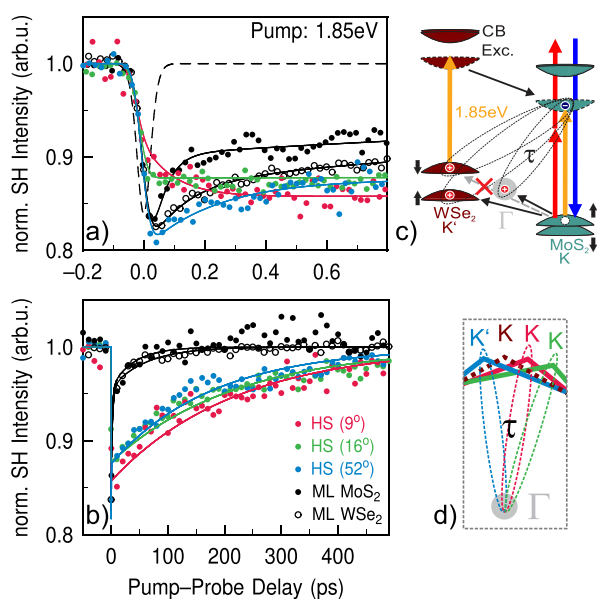

Figure 3. Time-resolved SHG of the MoS$_2$/WSe$_2$ heterostructures with three different stackings. (a,b) SH transients and corresponding fits as in Figure 2(a,b) but for 1.85 eV pump-photon energy, resonant with the MoS$_2$ intralayer A-exciton. (c) Sketch of the energy alignment for MoS$_2$/WSe$_2$ following the same scheme as in Figure 2(c) but for resonant excitation in MoS$_2$ while still probing MoS$_2$. The higher excitation energy opens up additional relaxation pathways by ultrafast hole transfer to the hybridized Γ-point or to the K/K′-points of WSe$_2$. Three different kinds of conceivable interlayer excitons are marked by dashed ellipses. For the quasi-2H stacked sample, hole transfer to K′ is spin-forbidden, and only two transfer possibilities remain. (d) Cutout from the Brillouin zone illustrating the charge recombination *via* the Γ-point.

in accordance with a direct excitation in MoS$_2$. With respect to the delayed filling, the SH transients of the quasi-3R and the misaligned sample stay similar, whereas the behavior of the quasi-2H stacked sample changes drastically. In contrast to the 1.70 eV excitation, where the SH signal of the quasi-2H sample was observed to recover monoexponentially with a slow recovery rate, the SH response after 1.85 eV excitation begins to recover immediately on a femtosecond time scale. The extracted lifetime (τ_{2H} = 215 fs) is only slightly slower than the corresponding monolayer decay times for 1.85 eV excitation $\left(\tau_{MoS_2} = 44 \text{ fs}, \tau_{WSe_2} = 123 \text{ fs}\right)$.

This ultrafast decay process is associated with the coherent radiative recombination of intralayer excitons.[38,39] On the one hand, the slightly slower recovery of the heterostructure signal compared to the monolayer can be explained by the change of the dielectric environment: The enhanced screening for the heterostructure decreases the binding energy of the excitons[40] and therefore increases their Bohr radius and the recombination time. On the other hand, the coherent radiative recombination competes with an additional relaxation mechanism in the heterostructure such as hole transfer to the hybridized Γ-point or to the WSe$_2$ layer as illustrated in Figure 3(c). Since at 1.85 eV excitation electron transfer from WSe$_2$ to MoS$_2$ is feasible as well, the detected SH signal in the MoS$_2$ is a mixture of various processes. Thus, a clear interpretation of our SH transients and an unambiguous determination of specific hole-transfer times becomes challenging. The competing processes might also explain why we do not observe any clear ultrafast component for the quasi-3R and the misaligned heterostructure sample in our data. Another plausible explanation for the absence of the ultrafast decay in these two heterostructures could also be related to the energy alignment and the spin structure of the involved states. After photoexcitation inside the MoS$_2$, the generated hole has two obvious relaxation pathways alternative to intralayer recombination: it can either be scattered to the hybridized states around the Γ-point or to the K/K′-point in WSe$_2$. In the case of 2H-stacking, transfer to the valence band maximum of WSe$_2$ at K′ is spin forbidden as sketched in Figure 3(c). For the misaligned sample, scattering to K/K′ should also be reduced due to the large momentum mismatch. In contrast, hole transfer to the valence band maximum at the K-point should be most efficient in the case of 3R-stacking. Assuming the hole transfer to K/K′ to be a competing process to the coherent recombination and taking place on a similar or faster time scale, the decreasing efficiency of the hole transfer to K/K′ from quasi-3R, misaligned to quasi-2H, could then explain the increasing manifestation of the coherent recombination.

The comparison of the SH transients at large pump−probe delays for both excitation energies in Figures 2(b) and 3(b) reveals a surprising change in the dynamics caused by the higher excitation energy. For 1.70 eV excitation, the recovery rates of the three heterostructure samples differ considerably as discussed above. In the case of 1.85 eV excitation, however, the lifetimes τ_{HS} become very similar for all samples (quasi-2H: 180 ± 9 ps, quasi-3R: 217 ± 8 ps, misaligned: 220 ± 5 ps). For 1.70 eV excitation, the quasi-2H configuration showed the fastest recovery time due to the larger wave function overlap between the layers. For 1.85 eV, however, the lack of interaction between the layers for the other two samples is compensated by the additional decay routes of the charge carriers generated in the MoS$_2$. The central difference between

the two excitation energies is that for 1.85 eV excitation the hole states around the Γ-point become energetically available. Photoluminescence from momentum-space indirect Γ-K interlayer excitons has been observed for all examined stacking configurations of MoS_2/WSe_2.[17] Therefore, we attribute our observed decay dynamics to the radiative recombination of Γ-K interlayer excitons. Due to the fact that the states around the Γ-point consist inherently of orbitals which are delocalized and therefore spread out over both layers, the overlap of the wave functions of electron and hole is enhanced, and thus, radiative recombination is facilitated. This overall enhancement of the recombination compensates the reduced overlap for the quasi-3R and the misaligned sample equalizing the lifetimes of the excitation independent of the stacking configuration.

CONCLUSION

In conclusion, we have employed time- and polarization-resolved second-harmonic imaging microscopy to study the ultrafast charge-carrier dynamics across the MoS_2/WSe_2 heterostructure interface for different stacking configurations. For lower excitation energies of 1.70 eV, electron transfer from WSe_2 to MoS_2 is found to depend considerably on the stacking angle and the transfer time is reduced by a factor of 7 when going from a larger rotational mismatch toward 2H-stacking. At higher excitation energies, ultrafast hole transfer from MoS_2 to hybridized states at the Γ-point and to the K-points of WSe_2 has to be considered. The respective decay dynamics, however, does not show a significant dependence on the stacking angle indicating that radiative recombination of indirect Γ-K excitons becomes the dominant decay route for all samples.

METHODS

The experiments were performed under ambient conditions using a Yb:KGW-based ultrashort pulse laser system (Light Conversion Carbide) feeding two optical parametric amplifiers (Orpheus-F Twin, Orpheus-N) providing photon energies in the range from 1.3 to 1.9 eV at a repetition rate of 200 kHz. The photon energy of the probe pulse was chosen to be 1.55 eV well below the bandgap of both materials in order to exclude optical excitation by the probe beam. Our temporal resolution is only limited by the laser system and can be estimated from the measured autocorrelations and cross-correlations of the used laser pulses as discussed in more detail in the Supporting Information. The pulse widths of the individual pulses correspond to 50, 38, and 34 fs (fwhm) for 1.55, 1.70, and 1.85 eV, respectively. Due to the nonlinear SHG detection, the relevant pulse width of the probe pulse is reduced to $50 \text{ fs}/\sqrt{2} = 35$ fs. The minimal time resolution is then estimated to be 1/5th of the respective cross-correlation of pump and probe pulse and corresponds to 11 and 10 fs for 1.70 and 1.85 eV pump-photon energy. The almost collinear pump and probe beams are only slightly focused onto the sample under angles of 16° and 18°, respectively. The resulting 1/e-widths of pump and probe beam on the sample are >350 μm and, thus, much larger than the typical size of the evaluated sample areas of 5×5 μm^2 which minimizes parasitic effect due to beam variation or laser drift. After passing a 400 nm dielectric filter, the specular reflected SH response of the probe beam is imaged optically magnified by a camera lens on an electron-multiplied CCD chip (Princeton Instruments ProEM-HS). Typical exposure times are 10 s. The applied magnification is $M \approx 38$. Thus, the visible sample region on the CCD is about 350×350 μm^2 and no scanning of the laser or the sample is required. The overall spatial resolution of our imaging microscopy setup is better than 2 μm as discussed in the Supporting Information. The time-delay between pump and probe beam is varied by a motorized delay stage. The polarization of pump and probe beam can be varied by means of $\lambda/2$-plates. The typically detected p-polarization of the second-harmonic

light is separated by an analyzer. The applied pump fluence was fixed to 45 μJ/cm^2 for 1.85 eV and 38 μJ/cm^2 for 1.70 eV on the sample (spot diameter 1/e). The applied probe fluence was fixed to 250 μJ/cm^2. These fluences lead to an initial exciton density of $3.65 \cdot 10^{12}$/cm^2 (WSe_2) for 1.70 eV and $9.3 \cdot 10^{11}$/cm^2 (WSe_2) as well as $5.3 \cdot 10^{12}$/cm^2 (MoS_2) for 1.85 eV pump energy (calculated with data from[37] with the tmm package[41]). These excitation densities are below the calculated Mott-density[42] ensuring that we are measuring exciton and not plasma dynamics. Long-term measurements with these fluences applied did not exhibit any multishot damage. A more detailed description of the setup can be found elsewhere.[35] Sample preparation and characterization is described in detail in ref 17.

ASSOCIATED CONTENT

Ⓢ Supporting Information

The Supporting Information is available free of charge at https://pubs.acs.org/doi/10.1021/acsnano.1c04549.

Details about spatial and temporal resolution of our experimental setup (PDF)

AUTHOR INFORMATION

Corresponding Author

Gerson Mette − Fachbereich Physik und Zentrum für Materialwissenschaften, Philipps-Universität, 35032 Marburg, Germany; ⓞ orcid.org/0000-0001-7561-3264; Email: gerson.mette@physik.uni-marburg.de

Authors

Jonas E. Zimmermann − Fachbereich Physik und Zentrum für Materialwissenschaften, Philipps-Universität, 35032 Marburg, Germany

Marleen Axt − Fachbereich Physik und Zentrum für Materialwissenschaften, Philipps-Universität, 35032 Marburg, Germany

Fabian Mooshammer − Institut für Experimentelle und Angewandte Physik, Universität Regensburg, 93053 Regensburg, Germany; ⓞ orcid.org/0000-0002-9744-2694

Philipp Nagler − Institut für Experimentelle und Angewandte Physik, Universität Regensburg, 93053 Regensburg, Germany

Christian Schüller − Institut für Experimentelle und Angewandte Physik, Universität Regensburg, 93053 Regensburg, Germany

Tobias Korn − Institut für Physik, Universität Rostock, 18059 Rostock, Germany; ⓞ orcid.org/0000-0003-4808-391X

Ulrich Höfer − Fachbereich Physik und Zentrum für Materialwissenschaften, Philipps-Universität, 35032 Marburg, Germany

Complete contact information is available at: https://pubs.acs.org/10.1021/acsnano.1c04549

Notes

The authors declare no competing financial interest.

REFERENCES

(1) Geim, A. K.; Grigorieva, I. V. Van der Waals Heterostructures. *Nature* 2013, *499*, 419−25.

(2) Lim, H.; Yoon, S. I.; Kim, G.; Jang, A. R.; Shin, H. S. Stacking of Two-Dimensional Materials in Lateral and Vertical Directions. *Chem. Mater.* 2014, *26*, 4891−903.

(3) Mak, K. F.; Shan, J. Photonics and Optoelectronics of 2D Semiconductor Transition Metal Dichalcogenides. *Nat. Photonics* 2016, *10*, 216−26.

(4) Xu, X. D.; Yao, W.; Xiao, D.; Heinz, T. F. Spin and Pseudospins in Layered Transition Metal Dichalcogenides. *Nat. Phys.* 2014, *10*, 343−50.

(5) Özcelik, V. O.; Azadani, J. G.; Yang, C.; Koester, S. J.; Low, T. Band Alignment of Two-Dimensional Semiconductors for Designing Heterostructures with Momentum Space Matching. *Phys. Rev. B: Condens. Matter Mater. Phys.* 2016, *94*, 035125.

(6) Wang, Z.; Altmann, P.; Gadermaier, C.; Yang, Y.; Li, W.; Ghirardini, L.; Trovatello, C.; Finazzi, M.; Duò, L.; Celebrano, M.; Long, R.; Akinwande, D.; Prezhdo, O. V.; Cerullo, G.; Dal, C. S. Phonon-Mediated Interlayer Charge Separation and Recombination in a MoSe$_2$/WSe$_2$ Heterostructure. *Nano Lett.* 2021, *21*, 2165−2173.

(7) Zheng, S.-W.; Wang, H.-Y.; Wang, L.; Wang, H.; Sun, H.-B. Layer-Dependent Electron Transfer and Recombination Processes in MoS$_2$/WSe$_2$ Multilayer Heterostructures. *J. Phys. Chem. Lett.* 2020, *11*, 9649−9655.

(8) Zimmermann, J. E.; Kim, Y. D.; Hone, J. C.; Höfer, U.; Mette, G. Directional Ultrafast Charge Transfer in a WSe$_2$/MoSe$_2$ Heterostructure Selectively Probed by Time-Resolved SHG Imaging Microscopy. *Nanoscale Horiz* 2020, *5*, 1603−1609.

(9) Calman, E. V.; Fowler-Gerace, L. H.; Choksy, D. J.; Butov, L. V.; Nikonov, D. E.; Young, I. A.; Hu, S.; Mishchenko, A.; Geim, A. K. Indirect Excitons and Trions in MoSe$_2$/WSe$_2$ van der Waals Heterostructures. *Nano Lett.* 2020, *20*, 1869−75.

(10) Ovesen, S.; Brem, S.; Linderälv, C.; Kuisma, M.; Korn, T.; Erhart, P.; Selig, M.; Malic, E. Interlayer Exciton Dynamics in van der Waals Heterostructures. *Commun. Phys.* 2019, *2*, 23.

(11) Rivera, P.; Yu, H.; Seyler, K. L.; Wilson, N. P.; Yao, W.; Xu, X. Interlayer Valley Excitons in Heterobilayers of Transition Metal Dichalcogenides. *Nat. Nanotechnol.* 2018, *13*, 1004.

(12) Miller, B.; Steinhoff, A.; Pano, B.; Klein, J.; Jahnke, F.; Holleitner, A.; Wurstbauer, U. Long-Lived Direct and Indirect Interlayer Excitons in van der Waals Heterostructures. *Nano Lett.* 2017, *17*, 5229−37.

(13) Schaibley, J. R.; Rivera, P.; Yu, H. Y.; Seyler, K. L.; Yan, J. Q.; Mandrus, D. G.; Taniguchi, T.; Watanabe, K.; Yao, W.; Xu, X. D. Directional Interlayer Spin-Valley Transfer in Two-Dimensional Heterostructures. *Nat. Commun.* 2016, *7*, 13747.

(14) Rivera, P.; Schaibley, J. R.; Jones, A. M.; Ross, J. S.; Wu, S. F.; Aivazian, G.; Klement, P.; Seyler, K.; Clark, G.; Ghimire, N. J.; Yan, J. Q.; Mandrus, D. G.; Yao, W.; Xu, X. D. Observation of Long-Lived Interlayer Excitons in Monolayer MoSe$_2$-WSe$_2$ Heterostructures. *Nat. Commun.* 2015, *6*, 6242.

(15) Fang, H.; Battaglia, C.; Carraro, C.; Nemsak, S.; Ozdol, B.; Kang, J. S.; Bechtel, H. A.; Desai, S. B.; Kronast, F.; Unal, A. A.; Conti, G.; Conlon, C.; Palsson, G. K.; Martin, M. C.; Minor, A. M.; Fadley, C. S.; Yablonovitch, E.; Maboudian, R.; Javey, A. Strong Interlayer Coupling in van der Waals Heterostructures Built from Single-Layer Chalcogenides. *Proc. Natl. Acad. Sci. U. S. A.* 2014, *111*, 6198−202.

(16) Hong, X. P.; Kim, J.; Shi, S. F.; Zhang, Y.; Jin, C. H.; Sun, Y. H.; Tongay, S.; Wu, J. Q.; Zhang, Y. F.; Wang, F. Ultrafast Charge Transfer in Atomically Thin MoS$_2$/WS$_2$ Heterostructures. *Nat. Nanotechnol.* 2014, *9*, 682−86.

(17) Kunstmann, J.; Mooshammer, F.; Nagler, P.; Chaves, A.; Stein, F.; Paradiso, N.; Plechinger, G.; Strunk, C.; Schüller, C.; Seifert, G.; Reichman, D. R.; Korn, T. Momentum-Space Indirect Interlayer Excitons in Transition-Metal Dichalcogenide van der Waals Heterostructures. *Nat. Phys.* 2018, *14*, 801−805.

(18) Brotons-Gisbert, M.; Baek, H.; Molina-Sánchez, A.; Campbell, A.; Scerri, E.; White, D.; Watanabe, K.; Taniguchi, T.; Bonato, C.; Gerardot, B. D. Spin−Layer Locking of Interlayer Excitons Trapped in Moiré Potentials. *Nat. Mater.* 2020, *19*, 630−636.

(19) Merkl, P.; Mooshammer, F.; Brem, S.; Girnghuber, A.; Lin, K.-Q.; Weigl, L.; Liebich, M.; Yong, C.-K.; Gillen, R.; Maultzsch, J.; Lupton, J. M.; Malic, E.; Huber, R. Twist-Tailoring Coulomb Correlations in van der Waals Homobilayers. *Nat. Commun.* 2020, *11*, 2167.

(20) Gogoi, P. K.; Lin, Y. C.; Senga, R.; Komsa, H. P.; Wong, S. L.; Chi, D. Z.; Krasheninnikov, A. V.; Li, L. J.; Breese, M. B. H.; Pennycook, S. J.; Wee, A. T. S.; Suenaga, K. Layer Rotation-Angle-Dependent Excitonic Absorption in van der Waals Heterostructures Revealed by Electron Energy Loss Spectroscopy. *ACS Nano* 2019, *13*, 9541−50.

(21) Hsu, W.-T.; Lu, L.-S.; Wu, P.-H.; Lee, M.-H.; Chen, P.-J.; Wu, P.-Y.; Chou, Y.-C.; Jeng, H.-T.; Li, L.-J.; Chu, M.-W.; Chang, W.-H. Negative Circular Polarization Emissions from WSe$_2$/MoSe$_2$ Commensurate Heterobilayers. *Nat. Commun.* 2018, *9*, 1356.

(22) Yeh, P. C.; Jin, W.; Zaki, N.; Kunstmann, J.; Chenet, D.; Arefe, G.; Sadowski, J. T.; Dadap, J. I.; Sutter, P.; Hone, J.; Osgood, R. M. Direct Measurement of the Tunable Electronic Structure of Bilayer MoS$_2$ by Interlayer Twist. *Nano Lett.* 2016, *16*, 953−59.

(23) Zheng, S. J.; Sun, L. F.; Zhou, X. H.; Liu, F. C.; Liu, Z.; Shen, Z. X.; Fan, H. J. Coupling and Interlayer Exciton in Twist-Stacked WS$_2$ Bilayers. *Adv. Opt. Mater.* 2015, *3*, 1600−05.

(24) Liu, K. H.; Zhang, L. M.; Cao, T.; Jin, C. H.; Qiu, D. A.; Zhou, Q.; Zettl, A.; Yang, P. D.; Louie, S. G.; Wang, F. Evolution of Interlayer Coupling in Twisted Molybdenum Disulfide Bilayers. *Nat. Commun.* 2014, *5*, 4966.

(25) Karni, O.; Barré, E.; Lau, S. C.; Gillen, R.; Ma, E. Y.; Kim, B.; Watanabe, K.; Taniguchi, T.; Maultzsch, J.; Barmak, K.; Page, R. H.; Heinz, T. F. Infrared Interlayer Exciton Emission in MoS$_2$/WSe$_2$ Heterostructures. *Phys. Rev. Lett.* 2019, *123*, 247402.

(26) Zhu, H. M.; Wang, J.; Gong, Z. Z.; Kim, Y. D.; Hone, J.; Zhu, X. Y. Interfacial Charge Transfer Circumventing Momentum Mismatch at Two-Dimensional van der Waals Heterojunctions. *Nano Lett.* 2017, *17*, 3591−98.

(27) Merkl, P.; Mooshammer, F.; Steinleitner, P.; Girnghuber, A.; Lin, K. Q.; Nagler, P.; Holler, J.; Schüller, C.; Lupton, J. M.; Korn, T.; Ovesen, S.; Brem, S.; Malic, E.; Huber, R. Ultrafast Transition between Exciton Phases in van der Waals Heterostructures. *Nat. Mater.* 2019, *18*, 691−696.

(28) Zhou, H. Z.; Zhao, Y. D.; Tao, W. J.; Li, Y. J.; Zhou, Q. H.; Zhu, H. M. Controlling Exciton and Valley Dynamics in Two-Dimensional Heterostructures with Atomically Precise Interlayer Proximity. *ACS Nano* 2020, *14*, 4618−25.

(29) Yu, Y.; Wang, Z. Y.; Wei, J. L.; Zhao, W. Y.; Lin, X.; Jin, Z. M.; Liu, W. M.; Ma, G. H. Ultrafast Formation and Dynamics of Interlayer Exciton in a Large-Area CVD-Grown WS$_2$/WSe$_2$ Heterostructure. *J. Phys.: Condens. Matter* 2018, *30*, 495701.

(30) Peng, B.; Yu, G. N.; Liu, X. F.; Liu, B.; Liang, X.; Bi, L.; Deng, L. J.; Sum, T. C.; Loh, K. P. Ultrafast Charge Transfer in MoS$_2$/WSe$_2$ P-N Heterojunction. *2D Mater.* 2016, *3*, 025020.

(31) Ceballos, F.; Bellus, M. Z.; Chiu, H. Y.; Zhao, H. Ultrafast Charge Separation and Indirect Exciton Formation in a MoS$_2$-MoSe$_2$ van der Waals Heterostructure. *ACS Nano* 2014, *8*, 12717−24.

(32) Shi, J.; Li, Y. Z.; Zhang, Z. P.; Feng, W. Q.; Wang, Q.; Ren, S. L.; Zhang, J.; Du, W. N.; Wu, X. X.; Sui, X. Y.; Mi, Y.; Wang, R.; Sun, Y. H.; Zhang, L. J.; Qiu, X. H.; Lu, J.; Shen, C.; Zhang, Y. F.; Zhang, Q.; Liu, X. F. Twisted-Angle-Dependent Optical Behaviors of Intralayer Excitons and Trions in WS$_2$/WSe$_2$ Heterostructure. *ACS Photonics* 2019, *6*, 3082−91.

(33) Zeng, H.; Liu, X.; Zhang, H.; Cheng, X. New Theoretical Insights into the Photoinduced Carrier Transfer Dynamics in WS$_2$/WSe$_2$ van der Waals Heterostructures. *Phys. Chem. Chem. Phys.* 2021, *23*, 694−701.

(34) Wang, H.; Bang, J.; Sun, Y.; Liang, L.; West, D.; Meunier, V.; Zhang, S. The Role of Collective Motion in the Ultrafast Charge Transfer in van der Waals Heterostructures. *Nat. Commun.* 2016, *7*, 11504.

(35) Zimmermann, J. E.; Li, B.; Hone, J. C.; Höfer, U.; Mette, G. Second-Harmonic Imaging Microscopy for Time-Resolved Investigations of Transition Metal Dichalcogenides. *J. Phys.: Condens. Matter* **2020**, *32*, 485901.

(36) Kozawa, D.; Kumar, R.; Carvalho, A.; Amara, K. K.; Zhao, W. J.; Wang, S. F.; Toh, M. L.; Ribeiro, R. M.; Neto, A. H. C.; Matsuda, K.; Eda, G. Photocarrier Relaxation Pathway in Two-Dimensional Semiconducting Transition Metal Dichalcogenides. *Nat. Commun.* **2014**, *5*, 4543.

(37) Li, Y. L.; Chernikov, A.; Zhang, X.; Rigosi, A.; Hill, H. M.; van der Zande, A. M.; Chenet, D. A.; Shih, E. M.; Hone, J.; Heinz, T. F. Measurement of the Optical Dielectric Function of Monolayer Transition-Metal Dichalcogenides: MoS_2, $MoSe_2$, WS_2, and WSe_2. *Phys. Rev. B: Condens. Matter Mater. Phys.* **2014**, *90*, 205422.

(38) Selig, M.; Berghäuser, G.; Richter, M.; Bratschitsch, R.; Knorr, A.; Malic, E. Dark and Bright Exciton Formation, Thermalization, and Photoluminescence in Monolayer Transition Metal Dichalcogenides. *2D Mater.* **2018**, *5*, 035017.

(39) Poellmann, C.; Steinleitner, P.; Leierseder, U.; Nagler, P.; Plechinger, G.; Porer, M.; Bratschitsch, R.; Schüller, C.; Korn, T.; Huber, R. Resonant Internal Quantum Transitions and Femtosecond Radiative Decay of Excitons in Monolayer WSe_2. *Nat. Mater.* **2015**, *14*, 889−893.

(40) Raja, A.; Chaves, A.; Yu, J.; Arefe, G.; Hill, H. M.; Rigosi, A. F.; Berkelbach, T. C.; Nagler, P.; Schüller, C.; Korn, T.; Nuckolls, C.; Hone, J.; Brus, L. E.; Heinz, T. F.; Reichman, D. R.; Chernikov, A. Coulomb Engineering of the Bandgap and Excitons in Two-Dimensional Materials. *Nat. Commun.* **2017**, *8*, 15251.

(41) Byrnes, S. J. Multilayer Optical Calculations. **2020**, *arXiv:1603.02720*. https://arxiv.org/abs/1603.02720 (accessed 2021-08-29).

(42) Meckbach, L.; Stroucken, T.; Koch, S. W. Giant Excitation Induced Bandgap Renormalization in TMDC Monolayers. *Appl. Phys. Lett.* **2018**, *112*, 061104.

G

Supporting Information

Ultrafast Charge-Transfer Dynamics in Twisted MoS$_2$/WSe$_2$ Heterostructures

J. E. Zimmermann[1], M. Axt[1], F. Mooshammer[2], P. Nagler[2], C. Schüller[2],

T. Korn[3] U. Höfer[1], and G. Mette[1,*]

[1]Fachbereich Physik und Zentrum für Materialwissenschaften, Philipps-Universität,
35032 Marburg, Germany

[2]Institut für Experimentelle und Angewandte Physik, Universität Regensburg,
93053 Regensburg, Germany

[3]Institut für Physik, Universität Rostock, 18059 Rostock, Germany

* corresponding author: gerson.mette@physik.uni-marburg.de

1

1 Spatial Resolution

The spatial resolution of our SHG imaging microscopy setup has been determined by usage of a resolution target with four-fold nested checkerboard pattern consisting of $1 \times 1\,\mu\text{m}^2$ small gold squares on a silicon substrate. As shown in Fig. S1(a), the Au squares are forming $10 \times 10\,\mu\text{m}^2$ small checkerboards which in turn are subunits of larger $100 \times 100\,\mu\text{m}^2$ checkerboards. Under illumination with 400-nm light, the resolution of our setup is determined to be better than $2\,\mu\text{m}$ as the horizontal interstice between the $10 \times 10\,\mu\text{m}^2$ checkerboard units ($\delta = \sqrt{2}\,\mu\text{m}$) is clearly resolvable.
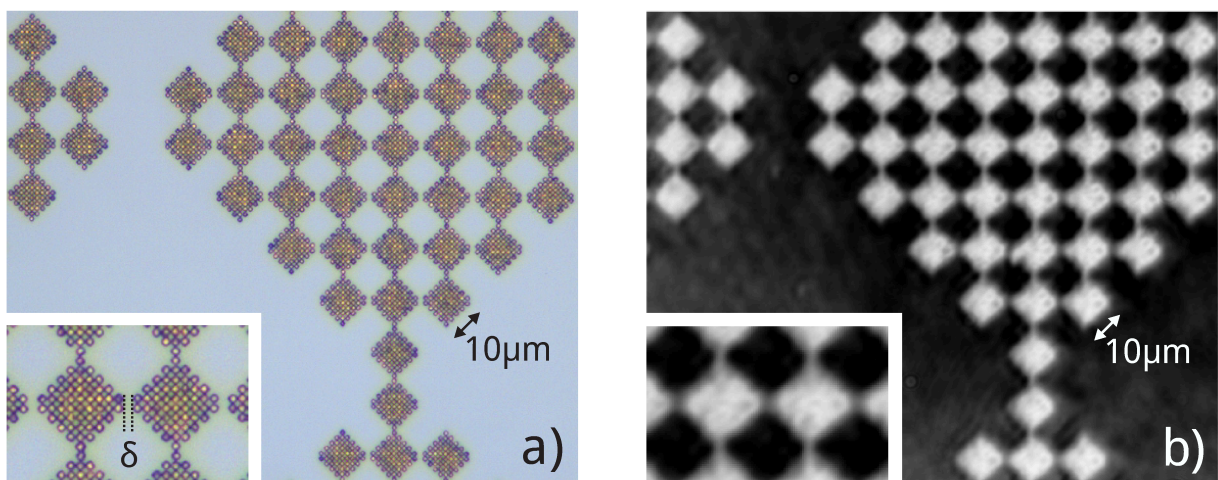

Figure S1: (a) Optical microscopy image of the resolution target. (b) Corresponding intensity-inverted image obtained by SHG imaging microscopy under illumination with 400-nm light. Whereas the $1 \times 1\,\mu\text{m}^2$ small Au squares cannot be differentiated individually, the horizontal interstice $\delta = \sqrt{2}\,\mu\text{m}$ between the $10 \times 10\,\mu\text{m}^2$ checkerboard units can be resolved clearly as shown in the insets.

2

2 Temporal Resolution

The temporal resolution of our setup is basically limited by the used laser system, since dispersive optical elements in front of the sample are avoided. The time resolution can be estimated from the measured auto-correlations and cross-correlations (CCR). The pulse widths of the individual pulses have been determined to be 50 fs, 38 fs and 34 fs (FWHM) for 1.55 eV, 1.70 eV and 1.85 eV, respectively. An experimental cross-correlation of the 1.70-eV pump and the 1.55-eV probe pulse measured directly on one of heterostructure samples by detecting the sum-frequency (SF) signal is shown by black data points in Fig. S2(a). Its temporal width corresponds to 66 fs (FWHM) as expected for a convolution of the two individual pulses. Due to the nonlinear SHG detection, the relevant pulse width of the probe pulse is reduced to $50\,\mathrm{fs}\,/\sqrt{2} = 35\,\mathrm{fs}$. Thus, a more realistic *simulated* cross-correlation of the 1.70-eV pump and the generated SH pulse is calculated to be 55 fs as shown by the orange line in Fig. S2(a). The time resolution is then estimated to be 1/5th of the respective simulated cross-correlation and corresponds to 11 fs and 10 fs for 1.70 eV and 1.85 eV pump-photon energy.

Fig. S2(b) shows the SH transients of the quasi-2H and quasi-3R sample upon 1.70 eV optical excitation like in Fig. 2 of the main text. An additional normalization on the pump-induced effect allows for an easier comparison of the data. Solid lines show the respective rate equation fits which yield the charge-transfer times for the different twist angles. The dashed orange line represents the instrumental response function (IRF) of the simulated cross-correlation. The measured SH transients both show a clear delay with respect to the IRF due to direct excitation of WSe$_2$ intralayer excitons and subsequent electron transfer into the MoS$_2$. The data indicate that also processes slightly faster than 10 fs might be resolvable, in particular if one allows for more averaging and smaller steps of the delay stage.
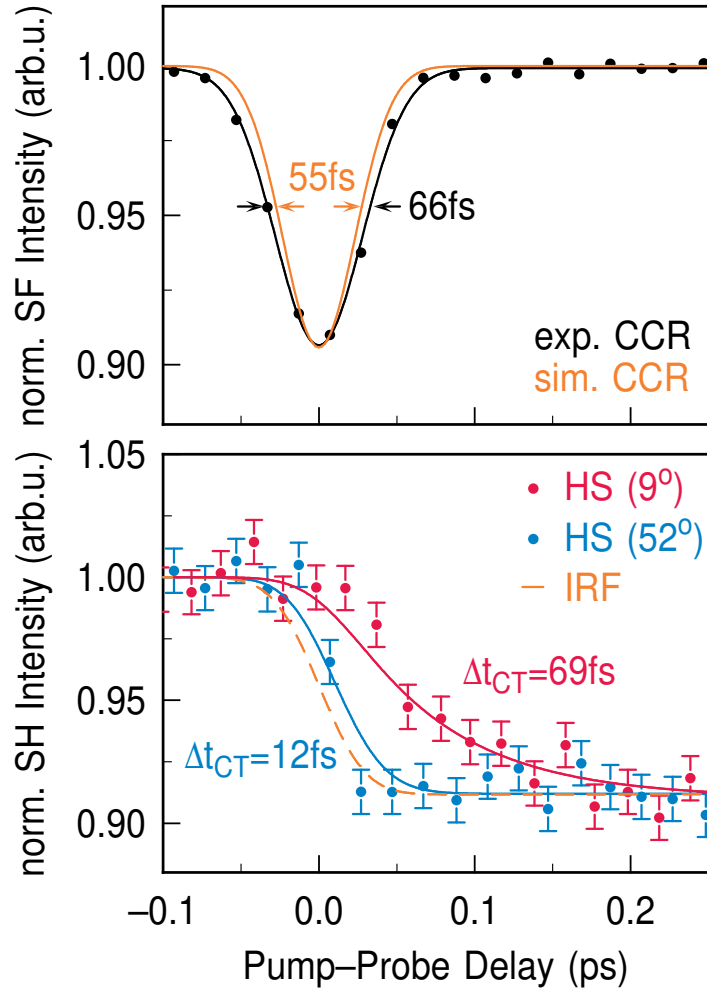
3

Figure S2: (a) Experimental cross-correlation of pump and probe pulse in comparison to a more realistic *simulated* cross-correlation of the pump and the generated SH pulse. (b) Two-fold normalized SH transients of the quasi-2H and quasi-3R sample and corresponding rate-equation fits in comparison to the instrumental response function (IRF) of the simulated cross-correlation.

Article IV

Band Gap-Tunable, Chiral Hybrid Metal Halides Displaying Second-Harmonic Generation

N. Dehnhardt, M. Axt, <u>J.E. Zimmermann</u>, M. Yang, G. Mette and J. Heine;
Chem. Mater. **32**, 11, 4801-4807 (2020)

Article

Band Gap-Tunable, Chiral Hybrid Metal Halides Displaying Second-Harmonic Generation

Natalie Dehnhardt, Marleen Axt, Jonas Zimmermann, Meng Yang, Gerson Mette,* and Johanna Heine*

Read Online

ACCESS | Metrics & More | Article Recommendations | Supporting Information

ABSTRACT: The introduction of chirality in lead halide perovskites and related metal halide materials allows for an expansion of their unique and useful properties toward nonlinear optics. However, when synthesizing materials based on less toxic metals antimony and bismuth, the large variability in the crystal structures of their metalates and their tendency to form molecular or chain-like anion motifs can be a challenge when creating tunable materials. Here, we show that using a chiral amine template, we can synthesize an isomorphous family of compounds $[(R)\text{-}1\text{-}(4\text{-}F)PEA]_4[E_2X_{10}]$ ($(R)\text{-}1\text{-}(4\text{-}F)PEA = (R)\text{-}1\text{-}(4\text{-fluoro})$-phenylethylammonium; E = Sb and Bi; X = Cl, Br, and I) that combines multiple aspects: the compounds are not only chiral but also feature a trilayered arrangement of cations and anions that allows for facile cleavage and exfoliation. The different combinations of E and X allow for a variation of the onset of absorption between 3.35 and 2.09 eV. Using femtosecond laser spectroscopy, we show that our materials allow for efficient second-harmonic generation. Together with a simple synthesis and good stability, this makes these materials promising candidates for linear and nonlinear optical devices.
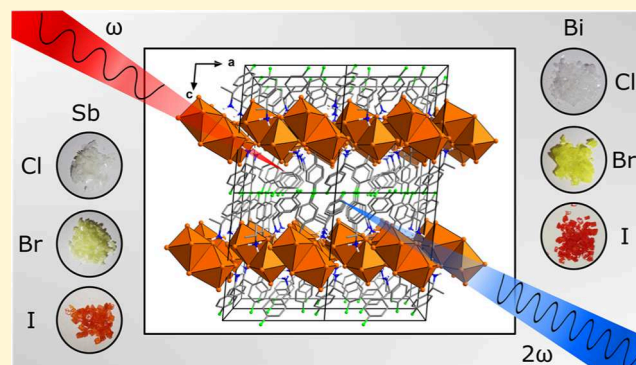
■ INTRODUCTION

The recent surge in interest in metal halide perovskites AMX_3 (A = Cs and CH_3NH_3; M = Sn and Pb; X = Cl, Br, and I)[1] and their successful use in photovoltaics[2] has sparked additional research into a number of related materials. Among these are layered main group halogenido metalates: inspired by works on perovskite-derived layered transition metal halides,[3] the first in-depth studies of these materials were performed in the 1980s and 1990s.[4−7] Compounds such as $(C_6H_5CH_2CH_2NH_3)_2SnI_4$ showed interesting optoelectronic properties and controllable, "natural quantum-well"[8] structures tested in LEDs[9] and FETs.[10]

Currently, investigations of such layered perovskite materials have been greatly expanded[11,12] and also include multinary compounds such as double perovskites.[13,14] A number of examples show that these materials can possess luminescence properties that vary from sharp lines to broad white light emission.[15] They can also be used in applications such as solar cells[16] and lasers[17] and show greater stability against moisture than their AMX_3 parent compounds.[18] Additionally, they provide great opportunities for material design, as new functionalities can be introduced via the organic cations[19−21] without rigid size requirements governing AMX_3 perovskites.[22,23] Their anisotropic nature also allows for integration with 2D materials such as graphene or MoS_2 monolayers.[24] One possible functionality of 2D perovskites that has recently come into focus is chirality: by using chiral amines, it is

possible to create chiral materials by design.[25,26] These can be used for the detection[27] and generation of circularly polarized light,[28] as ferroelectrics[29] and in spintronics.[30]

We are interested in halogenido metalates of antimony and bismuth, as these compounds avoid the toxicity[31] and instability[32] issues associated with lead-based and tin-based metalates, respectively.[33] Because of an increase in the charge of metals from 2+ to 3+, halogenido antimonates and bismuthates show a related, yet distinctly different structural chemistry compared to group 14 metalates.[34−36] In consequence, halogenido pentelates rarely form layered anions, especially when larger organic cations are used.[37−44]

In this work, we demonstrate a new approach toward halogenido metalates with similar properties as layered perovskite materials: we use organic cations that template a layered arrangement of the molecular halogenido pentelate anions. This way, we create an isomorphous family of compounds $[(R)\text{-}1\text{-}(4\text{-}F)PEA]_4[E_2X_{10}]$ ($(R)\text{-}1\text{-}(4\text{-}F)PEA = (R)\text{-}1\text{-}(4\text{-fluoro})$phenylethylammonium; E = Sb and Bi; X =

4801

Cl, Br, and I). This allows us to tune the onset of absorption from 400 to 600 nm and, by using an enantiopure amine, enforce a noncentrosymmetric crystal structure showing very efficient optical second-harmonic generation (SHG) under femtosecond laser excitation.

■ METHODS

General. All reagents were used as received from commercial sources. (*R*)-1-(4-Fluoro)phenylethylamine with 98% ee was obtained from Alfa Aesar. CHN analysis was carried out on an Elementar CHN-analyzer. Powder patterns were recorded on a STADI MP (STOE Darmstadt) powder diffractometer, with Cu Kα_1 radiation with $\lambda = 1.54056$ Å at room temperature in transmission mode (see Figures S7−S12). IR spectra were measured on a Bruker Tensor 37 FT-IR spectrometer equipped with an ATR-Platinum measuring unit (see Figures S13−18). Thermal analysis was carried out by simultaneous DTA/TG on a NETZSCH STA 409 C/CD in the temperature range of 25−1000 °C at a heating rate of 10 °C min^{-1} in a constant flow of 80 mL min^{-1} Ar (see Figures S19−S24). Optical absorption spectra were recorded on a Varian Cary 5000 UV/vis/NIR spectrometer in the range of 300−800 nm in diffuse reflectance mode employing a Praying Mantis accessory (Harrick). For the ease of viewing, raw data were transformed from % reflectance R to absorbance A according to $A = \log(1/R)$ which yields estimates comparable to the widely used Kubelka−Munk relation (see Figure S25).[45]

Synthesis. Sb$_2$O$_3$ or Bi$_2$O$_3$ was dissolved in the respective concentrated hydrohalic acid and an excess of (*R*)-1-(4-fluoro)-phenylethylamine was added directly. The solution was stirred and heated to reflux for 30 min, then left undisturbed to cool to room temperature. After 24 h, a crystalline product formed and was isolated by filtration. The product was washed with pentane and dried under vacuum. See Table S1 for individual amounts. Yields are given with respect to E$_2$O$_3$ as the limiting reagent.

[(R)-1-(4-F)PEA]₄[Sb₂Cl₁₀] (1). Colorless crystals. Yield: 24%. CHN Data for **1**: Anal. Calcd for C$_{32}$H$_{44}$Sb$_2$Cl$_{10}$F$_4$N$_4$, (M = 1158.71 gmol^{-1}): C, 33.17; H, 3.83; N, 4.84%. Found: C, 33.47; H, 3.87; N, 4.91%.

[(R)-1-(4-F)PEA]₄[Sb₂Br₁₀] (2). Very light yellow crystals. Yield: 23%. CHN data for **2**: Anal. Calcd for C$_{32}$H$_{44}$Sb$_2$Br$_{10}$F$_4$N$_4$, (M = 1603.31 g mol^{-1}): C, 23.97; H, 2.77; N, 3.49%. Found: C, 24.15; H, 2.72; N, 3.54%.

[(R)-1-(4-F)PEA]₄[Sb₂I₁₀] (3). Orange crystals. Yield: 28%. CHN data for **3**: Anal. Calcd for C$_{32}$H$_{44}$Sb$_2$I$_{10}$F$_4$N$_4$, (M = 2073.21 g mol^{-1}): C, 18.54; H, 2.14; N, 2.70%. Found: C, 18.71; H, 2.18; N, 2.76%.

[(R)-1-(4-F)PEA]₄[Bi₂Cl₁₀] (4). Colorless crystals. Yield: 40%. CHN data for **4**: Anal. Calcd for C$_{32}$H$_{44}$Bi$_2$Cl$_{10}$F$_4$N$_4$, (M = 1333.17 g mol^{-1}): C, 28.83; H, 3.33; N, 4.20%. Found: C, 29.00; H, 3.45; N, 4.19%.

[(R)-1-(4-F)PEA]₄[Bi₂Br₁₀] (5). Yellow crystals. Yield: 58%. CHN data for **5**: Anal. Calcd for C$_{32}$H$_{44}$Bi$_2$Br$_{10}$F$_4$N$_4$, (M = 1777.77g mol^{-1}): C, 21.62; H, 2.49; N, 3.15%. Found: C, 21.80; H, 2.65; N, 3.17%.

[(R)-1-(4-F)PEA]₄[Bi₂I₁₀] (6). Red crystals. Yield: 12%. CHN data for **6**: Anal. Calcd for C$_{32}$H$_{44}$Bi$_2$I$_{10}$F$_4$N$_4$, (M = 2247.67g mol^{-1}): C, 17.10; H, 1.97; N, 2.49%. Found: C, 17.31; H, 1.97; N, 2.56%.

X-ray Crystallography. Single-crystal X-ray determination was performed at 100 K on a Bruker D8 Quest diffractometer with microfocus Mo Kα radiation and a Photon 100 (CMOS) detector. The structures were solved using direct methods, refined by full-matrix least-squares techniques, and expanded using Fourier techniques, using the SHELX software package[46−48] within the OLEX2 suite.[49] All nonhydrogen atoms were refined anisotropically unless otherwise indicated. Hydrogen atoms were assigned to idealized geometric positions and included in structure factor calculations. Pictures of the crystal structures were created using DIAMOND.[50] Additional details on individual refinements are reported in the Supporting Information, Tables S2−S7 and Figures

S1−S6. The data for compounds **1−6** are deposited as CCDC 1995570−1995575.

SHG Setup. The SHG measurements were performed under ambient conditions using 10 fs laser pulses generated by a Ti:Sapphire oscillator operating at 800 nm at a repetition rate of 82 MHz. The generated second-harmonic (SH) light at frequency 2ω was observed in transmission for different combinations of input and output polarizations. Further details on the optical setup can be found in the Supporting Information.

■ RESULTS AND DISCUSSION

Synthesis. Compounds **1−6** can be obtained via a simple solution-based method. Sb$_2$O$_3$ or Bi$_2$O$_3$ is dissolved in an aqueous HX solution. (*R*)-4-Fluoro-α-methylbenzylamine is added and the solution is heated to reflux for 30 min. As the hot solution cools down, crystals of **1−6** are deposited which can be isolated by filtration. Photographs of the isolated compounds are shown in Figure 1. In the case of compound **1**,
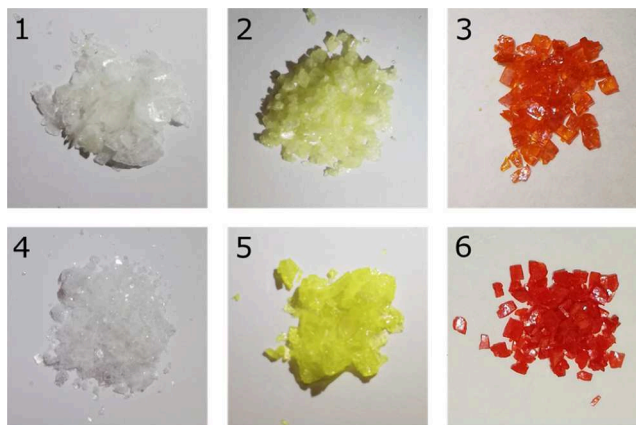

Figure 1. Crystalline samples of compounds **1−6**; the side length of photographs is about 1 cm.

the use of concentrated HCl solution is strictly necessary to suppress the formation of Sb$_4$Cl$_2$O$_5$,[51] underlining the fact that the tendency toward hydrolysis is greater in chlorides and antimonates.

X-ray Crystallography. Compounds **1−6** crystallize in the monoclinic Sohncke space group $P2_1$ with very low Flack parameters, as expected from the use of an enantiopure amine reagent. The specific crystal habit observed is dependent on the exact reaction conditions such as concentrations and cooling rates, allowing for the isolation of nontwinned blocks or planks. Typically, a fraction of the product crystallizes at the air−water interface as thin flakes, indicating that few-layered crystals may be available this way.[52] In block-like crystals, the (001) crystal face is easily identified, and it is possible to mechanically cleave the crystals perpendicular to (001) using Scotch Tape.

The compounds' crystal structure is composed of anionic [E$_2$X$_{10}$]$^{4-}$ building blocks and [(*R*)-1-(4-F)PEA]$^+$ ammonium units (Figure 2). [E$_2$X$_{10}$]$^{4-}$ anions are a well-known anion type in the chemistry of halogenido pentelates, and examples are known for each E−X combination discussed here.[53−56] The motif of an edge-sharing dinuclear anion appears to be especially prominent in compounds obtained from hydrohalic acid. Bond lengths are within expected ranges (see Table S7), with chlorides and antimonates showing a greater tendency toward more distorted octahedral environments around the
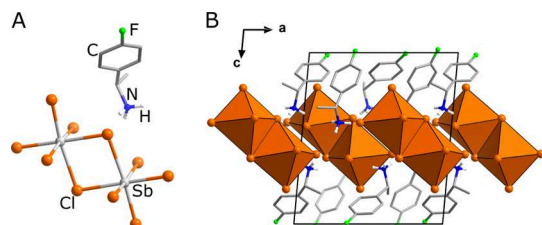
Figure 2. Excerpt of the crystal structure of **1** shown as an example for the whole isostructural series. All hydrogen atoms not belonging to the ammonium group are omitted for clarity. (A) The anion and the cation in **1**. (B) A unit cell with coordination polyhedra shown as closed octahedra.

metal atom and greater differences between the longer bridging and shorter terminal E−X bond lengths.

A comparison of the cell parameters along the isomorphous series shows the expected trends (see Table S7). The parameters *a* and *b* as well as cell volumes increase going from Cl → Br → I. The difference between antimonates and bismuthates is less clear-cut because of the larger range of the Sb−X bond length. Interestingly, the parameter *c* in **1** is the largest across the series, likely because of small differences in the arrangement of ammonium cations.

The significant feature of compounds **1**−**6** is their crystal packing (Figure 3). The $[E_2X_{10}]^{4-}$ anions are arranged in a layer in the *a*−*b* plane and the NH_3 groups of the organic ammonium cations are oriented toward this plane. This results in an overall charge-neutral trilayer, with only van der Waals
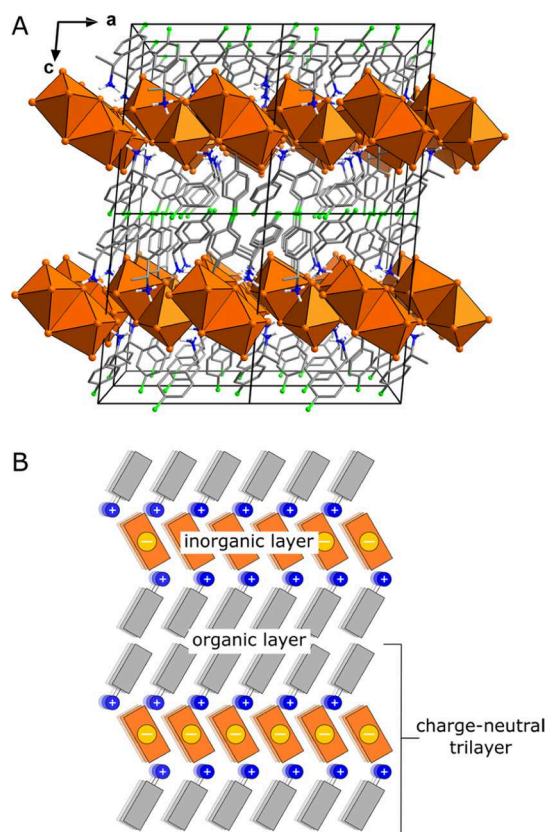

Figure 3. (A) Excerpt of the crystal structure of **1** in central projection with $Sb_2Cl_{10}^{4-}$ anions shown as closed polyhedra. (B) Conceptual sketch of the quantum-well-like nature of **1**−**6**, with separate organic and inorganic layers and cleavable, charge-neutral trilayers.

forces between the opposite 4-fluorophenyl groups. This pseudo-layered type of arrangement is unusual for halogenido pentelates featuring molecular anions. Typically, when using ammonium cations that enable layered arrangements in halogenido tetrelates such as *n*-butylammonium[57] or 1,6-diammoniohexane,[58] the supramolecular interactions are not strong enough to overcome the tendency toward a more even charge distribution in the pentelates,[59−61] where the additional driving force for the formation of a layered anion is missing.

A number of secondary interactions can be considered in **1**−**6**. The ionic interactions between the anions and cations are accompanied by N−H⋯X interactions[62] that provide more directionality to the overall arrangement and link the individual anions into a layer (see Figure S7). X⋯X interactions below the sum of the van der Waals radii provide further interconnection between anions within the *ab* plane (see Figure S8).[63] Overall, it appears that it is the sum of small interactions that enables this particular packing motif, not just the presence of a benzylammonium (BzA)-derived building block, as illustrated by the examples $[BzA]_2[SbBr_5]$ and $[BzA]_3[Sb_2I_9]$, where an overall nonplanar packing is observed.[64] Ok and group has recently shown that $[(R/S)$-$PEA]_4[Bi_2Br_{10}]$ (PEA = phenylethylammonium), a compound that is very similar to those presented here, can be obtained,[65] but their investigations were limited to single E−X combinations.

The use of chiral amines to produce chiral halogenido metalates of group 14 and 15 has remained rare despite the great interest in these materials and the ready availability of the starting materials from chemical suppliers,[66−68] with a growing number of examples prepared in the last year.[69−72] Nonetheless, these examples as well as our family of compounds show that the introduction of chirality by this route and the design of specific material properties is quite straightforward. The additional feature of a pseudo-layered arrangement in **1**−**6** provides the possibility to exfoliate the compounds and more easily integrate them into device architectures in controlled orientation.

Optical Properties. Absorption spectra of **1**−**6**, measured in diffuse reflection mode, are shown in Figure 4. The onset of absorption follows expected trends with regard to the influence of the halide, displaying red-shifts going from Cl to Br and I.[56] For chlorides and bromides, no large difference is observed going from Sb to Bi, with the bismuthates showing a steeper
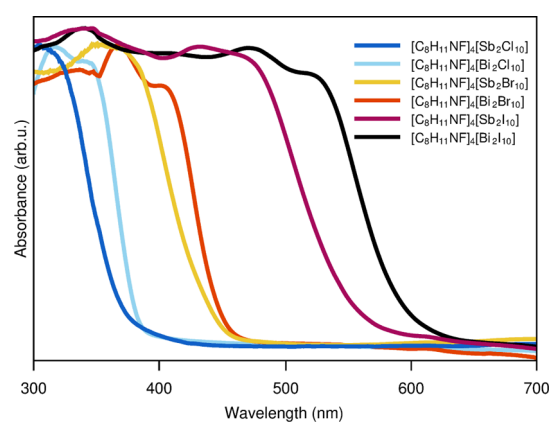

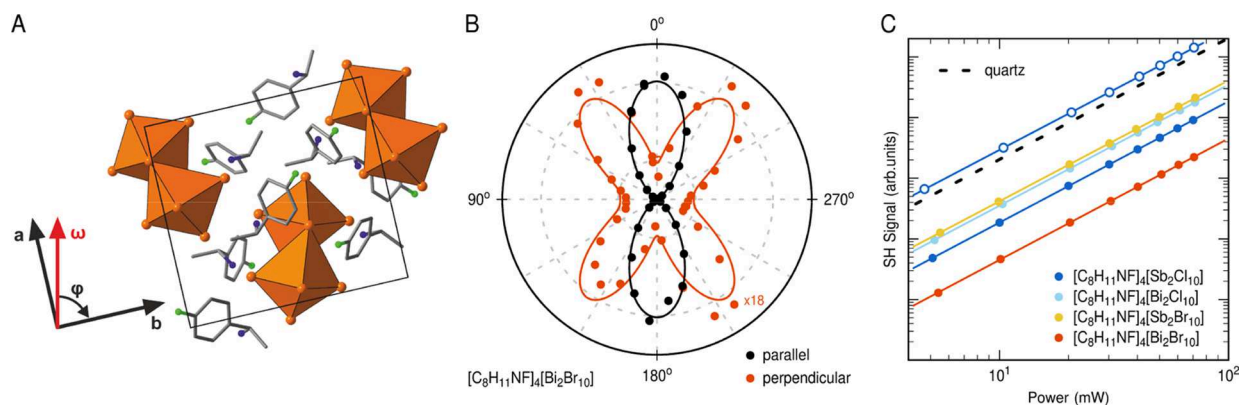**Figure 4.** UV−vis spectra of **1**−**6** measured in diffuse reflectance mode on ground single crystals.

Figure 5. (A) Top view of the crystal structure of **1** for the *ab*-plane perpendicular to the *c*-axis. The rotation angle $\varphi = 0°$ corresponds to an orientation where the vertical s-polarization of the 800 nm fundamental (ω, red arrow) is parallel to the *b*-direction. (B) Polar plot of the SH intensity of material **5** as a function of the crystal's azimuth angle φ. The SH radiation components parallel (black) and perpendicular (red) to the polarization of the fundamental field are shown. Symbols and solid lines represent the experimental data and the corresponding theoretical fits, respectively. (C) SH signal vs applied laser power for compounds **1**, **2**, **4**, and **5** in comparison to a quartz reference. Linear fits (lines) reveal the quadratic power dependence of the measured SH response from a set of thin samples of different materials (filled dots). A much thicker sample of compound **1** exhibits a significantly stronger SH signal (blue circles).

onset. In contrast, there is a more significant red-shift going from Sb to Bi for the iodido metalates **3** and **6** in line with a large difference in band gaps of the parent halides SbI_3 (2.2 eV)[73] and BiI_3 (1.7 eV).[74] Overall, this series provides the first data on the absorption properties of an isomorphous family of halogenido antimonates and bismuthates that do not feature a counterion with large influence on absorption, similar to the recently reported series of tropylium compounds.[75] While the trends we observe here may not be so surprising, we want to highlight that despite the great recent interest in iodido bismuthates like $(CH_3NH_3)_3[Bi_2I_9]$, data on optical properties of these materials remain conflicting,[40,76] and a series of compounds prepared and measured under the same conditions allow for an easy comparison and provide a solid reference point for future work. Overall, the onset of absorption in this family of compounds can be varied between 3.35 eV for **1** and 2.09 eV for **6** (see also Table S9) allowing for facile adaptation to potential applications.

Stability. All six compounds are stable against air and moisture. After several weeks in air, the crystals' surfaces change from clear and smooth to more brittle, indicating degradation on the surface level. They decompose completely over a two-step thermal degradation process, starting between 190 and 250 °C, with the bismuthates being more stable than the antimonates (see Figure S19−S24 for details). The lack of residual mass in TGA measurements suggests a concomitant sublimation of EX_3 and $[(R)$-1-(4-F)PEA$]X$ and the possibility to deposit the compounds, for example, via pulsed laser deposition in future experiments, similar to methods applied in 2D lead halide perovskite materials.[77] The compounds are also quite stable against laser damage, as we show below, with the exception of **6**, which displayed oscillating SHG signals under continuous laser irradiation, indicating at least some surface level damage.

Nonlinear Optical Properties. Second-order nonlinear processes such as SHG originate from a noncentrosymmetric crystal structure.[78] Because the compounds **1**–**6** share a monoclinic space group ($P2_1$), their nonlinear optical properties are investigated for 800 nm femtosecond laser excitation. All compounds **1**–**6** show efficient SHG with the expected quadratic dependence of the emitted 400 nm SH light on the

applied laser power. The rotational anisotropy of the SH intensity is measured by rotating the sample around the *c*-axis, as characterized by the azimuthal angle φ for selected input and output polarizations (cf. Figure 5A). As shown in Figure 5B, the strongest SH response is observed for s-polarized input and s-polarized output polarization ("parallel", black data points) at 0° azimuth angle. See Supporting Information for additional data and more details on the optical setup.

The polarization-dependent rotational anisotropy of compounds **1**, **2**, **4**, and **5** agree quite well with the expected anisotropies for $P2_1$ space group materials, as illustrated in Figure 5B for compound **5**. Materials **3** and **6**, however, deviate considerably from the expected anisotropies, probably because of inhomogeneity within these crystals or instability caused by laser damage, as observed for **6**. Therefore, it is not possible to determine the SH response of **3** and **6** at a defined azimuth angle for direct comparison of the SHG efficiency of different compounds. Figure 5C shows the SH signal of compounds **1**, **2**, **4**, and **5** relative to each other and with respect to the quartz (α-SiO_2) reference depending on the applied laser power. A set of samples with a respective crystal thickness of 125 ± 20 μm (filled colored dots) exhibits a 5−45 times smaller SH signal compared to the quartz reference with the strongest signal obtained from material **2** followed by materials **4**, **1**, and **5**. Because compound **2** shows a pronounced absorption peak around 400 nm in the UV−vis spectra, the SH response could be affected by resonant enhancement. Additionally, absorption of SH light in some of the crystals has to be considered (see Figure 4).

A much higher SH intensity is observed for a comparatively thick sample (700 ± 50 μm) of compound **1** (see the empty blue circles in Figure 5A). As it turns out, this sample yields a 15 times larger signal than the respective thin sample of compound **1**. This is in reasonable agreement with a quadratic dependence of the SH intensity on the crystal length for the case of perfect phase-matching in the undepleted-pump approximation.[78] Systematic measurements in dependence of the thickness of different crystals are necessary to explore this correlation in more detail. In addition, spectroscopic SHG measurements would be desirable, in particular, at longer excitation wavelengths, to investigate the possible effects of

resonant enhancement as well as absorption of SH light in different compounds. Overall, the nonlinear optical properties of the presented halogenido metalates are in the range of (and can even exceed) the nonlinear properties of crystalline quartz, which makes this material class with its large variability particularly interesting for application in nonlinear optical devices.

■ CONCLUSIONS

Using a suitable chiral amine template, it is possible to create an isomorphous family of organic−inorganic metal halide materials. The aspect of chirality in the materials is combined with a pseudo-layered arrangement allowing for well-defined crystal cleavage and exfoliation. Through the variation of metal and halides, a wide range of onsets of absorption can be achieved. The materials' SHG capabilities compare well with established materials like quartz. Overall, the ease of synthesis, high stability, and high variability will allow a facile integration of linear and nonlinear optical devices in future work.

■ ASSOCIATED CONTENT

Ⓢ Supporting Information

The Supporting Information is available free of charge at https://pubs.acs.org/doi/10.1021/acs.chemmater.0c01605.

Powder patterns, FTIR spectra, thermal analysis data, UV−vis spectra, details on the SHG setup and SHG data (PDF)
Single crystal data of compound **1** (CIF)
Single crystal data of compound **2** (CIF)
Single crystal data of compound **3** (CIF)
Single crystal data of compound **4** (CIF)
Single crystal data of compound **5** (CIF)
Single crystal data of compound **6** (CIF)

Accession Codes

CCDC 1995570−1995575 contain the supplementary crystallographic data for this paper. These data can be obtained free of charge via www.ccdc.cam.ac.uk/data_request/cif, or by emailing data_request@ccdc.cam.ac.uk, or by contacting The Cambridge Crystallographic Data Centre, 12 Union Road, Cambridge CB2 1EZ, UK; fax: +44 1223 336033.

■ AUTHOR INFORMATION

Corresponding Authors

Johanna Heine − *Department of Chemistry and Material Sciences Center, Philipps-Universität Marburg, 35043 Marburg, Germany;* ⓞ orcid.org/0000-0002-6795-5288; Email: johanna.heine@chemie.uni-marburg.de

Gerson Mette − *Department of Physics and Material Sciences Center, Philipps-Universität Marburg, 35032 Marburg, Germany;* ⓞ orcid.org/0000-0001-7561-3264; Email: gerson.mette@physik.uni-marburg.de

Authors

Natalie Dehnhardt − *Department of Chemistry and Material Sciences Center, Philipps-Universität Marburg, 35043 Marburg, Germany*

Marleen Axt − *Department of Physics and Material Sciences Center, Philipps-Universität Marburg, 35032 Marburg, Germany*

Jonas Zimmermann − *Department of Physics and Material Sciences Center, Philipps-Universität Marburg, 35032 Marburg, Germany*

Meng Yang − *Department of Chemistry and Material Sciences Center, Philipps-Universität Marburg, 35043 Marburg, Germany*

Complete contact information is available at:
https://pubs.acs.org/10.1021/acs.chemmater.0c01605

Author Contributions

The manuscript was written through contributions of all authors. All authors have given approval to the final version of the manuscript.

Notes

The authors declare no competing financial interest.

■ REFERENCES

(1) Stoumpos, C. C.; Kanatzidis, M. G. Halide Perovskites: Poor Man's High-Performance Semiconductors. *Adv. Mater.* **2016**, *28*, 5778−5793.

(2) Jena, A. K.; Kulkarni, A.; Miyasaka, T. Halide Perovskite Photovoltaics: Background, Status, and Future Prospects. *Chem. Rev.* **2019**, *119*, 3036−3103.

(3) Arend, H.; Huber, W.; Mischgofsky, F. H.; Richter-Van Leeuwen, G. K. Layer Perovskites of the $(C_nH_{2n+1}NH_3)_2MX_4$ and $NH_3(CH_2)_mNH_3MX_4$ Families with M = Cd, Cu, Fe, Mn or Pd and X = Cl or Br: Importance, Solubilities and Simple Growth Techniques. *J. Cryst. Growth* **1978**, *43*, 213−223.

(4) Nagapetyan, S. S.; Dolzhenko, Y. I.; Arakelova, E. R.; Koshkin, V. M.; Struchkov, Y. T.; Shklover, V. E. 33. Preparation, structure and properties of nonylammonium tetraiodoplumbate(II). *Zh. Neorg. Khim.* **1988**, *33*, 2806−2812.

(5) Calabrese, J.; Jones, N. L.; Harlow, R. L.; Herron, N.; Thorn, D. L.; Wang, Y. Preparation and Characterization of Layered Lead Halide Compounds. *J. Am. Chem. Soc.* **1991**, *113*, 2328−2330.

(6) Hong, X.; Ishihara, T.; Nurmikko, A. V. Dielectric Confinement Effect on Excitons in PbI_4-Based Layered Semiconductors. *Phys. Rev. B* **1992**, *45*, 6961−6964.

(7) Mitzi, D. B.; Feild, C. A.; Harrison, W. T. A.; Guloy, A. M. Conducting Tin Halides with a Layered Organic-Based Perovskite Structure. *Nature* **1994**, *369*, 467−469.

(8) Papavassiliou, G. C.; Koutselas, I. B.; Terzis, A.; Whangbo, M.-H. Structural and Electronic Properties of the Natural Quantum-Well System $(C_6H_5CH_2CH_2NH_3)_2SnI_4$. *Solid State Commun.* **1994**, *91*, 695−698.

(9) Era, M.; Morimoto, S.; Tsutsui, T.; Saito, S. Organicinorganic Heterostructure Electroluminescent Device Using a Layered Perovskite Semiconductor $(C_6H_5C_2H_4NH_3)_2PbI_4$. *Appl. Phys. Lett.* **1994**, *65*, 676−678.

(10) Kagan, C. R.; Mitzi, D. B.; Dimitrakopoulos, C. D. Organic-Inorganic Hybrid Materials as Semiconducting Channels in Thin-Film Field-Effect Transistors. *Science* **1999**, *286*, 945−947.

(11) Mao, L.; Stoumpos, C. C.; Kanatzidis, M. G. Two-Dimensional Hybrid Halide Perovskites: Principles and Promises. *J. Am. Chem. Soc.* **2019**, *141*, 1171−1190.

(12) Katan, C.; Mercier, N.; Even, J. Quantum and Dielectric Confinement Effects in Lower-Dimensional Hybrid Perovskite Semiconductors. *Chem. Rev.* **2019**, *119*, 3140−3192.

(13) Connor, B. A.; Leppert, L.; Smith, M. D.; Neaton, J. B.; Karunadasa, H. I. Layered Halide Double Perovskites: Dimensional Reduction of $Cs_2AgBiBr_6$. *J. Am. Chem. Soc.* **2018**, *140*, 5235−5240.

(14) Jana, M. K.; Janke, S. M.; Dirkes, D. J.; Dovletgeldi, S.; Liu, C.; Qin, X.; Gundogdu, K.; You, W.; Blum, V.; Mitzi, D. B. A Direct-Bandgap 2D Silver-Bismuth Iodide Double Perovskite: The Structure-Directing Influence of an Oligothiophene Spacer Cation. *J. Am. Chem. Soc.* **2019**, *141*, 7955−7964.

(15) Smith, M. D.; Karunadasa, H. I. White-Light Emission from Layered Halide Perovskites. *Acc. Chem. Res.* **2018**, *51*, 619−627.

(16) Cohen, B.-E.; Li, Y.; Meng, Q.; Etgar, L. Dion−Jacobson Two-Dimensional Perovskite Solar Cells Based on Benzene Dimethanam-monium Cation. *Nano Lett.* **2019**, *19*, 2588−2597.

(17) Raghavan, C. M.; Chen, T.-P.; Li, S.-S.; Chen, W.-L.; Lo, C.-Y.; Liao, Y.-M.; Haider, G.; Lin, C.-C.; Chen, C.-C.; Sankar, R.; Chang, Y.-M.; Chou, F.-C.; Chen, C.-W. Low-Threshold Lasing from 2D Homologous Organic−Inorganic Hybrid Ruddlesden−Popper Perov-skite Single Crystals. *Nano Lett.* **2018**, *18*, 3221−3228.

(18) Spanopoulos, I.; Hadar, I.; Ke, W.; Tu, Q.; Chen, M.; Tsai, H.; He, Y.; Shekhawat, G.; Dravid, V. P.; Wasielewski, M. R.; Mohite, A. D.; Stoumpos, C. C.; Kanatzidis, M. G. Uniaxial Expansion of the 2D Ruddlesden−Popper Perovskite Family for Improved Environmental Stability. *J. Am. Chem. Soc.* **2019**, *141*, 5518−5534.

(19) Smith, I. C.; Smith, M. D.; Jaffe, A.; Lin, Y.; Karunadasa, H. I. Between the Sheets: Postsynthetic Transformations in Hybrid Perovskites. *Chem. Mater.* **2017**, *29*, 1868−1884.

(20) Yang, S.; Wu, D.; Gong, W.; Huang, Q.; Zhen, H.; Ling, Q.; Lin, Z. Highly Efficient Room-Temperature Phosphorescence and Afterglow Luminescence from Common Organic fluorophores in 2D Hybrid Perovskites. *Chem. Sci.* **2018**, *9*, 8975−8981.

(21) Li, T.; Dunlap-Shohl, W. A.; Reinheimer, E. W.; Le Magueres, P.; Mitzi, D. B. Melting Temperature Suppression of Layered Hybrid Lead Halide Perovskites via Organic Ammonium Cation Branching. *Chem. Sci.* **2019**, *10*, 1168−1175.

(22) Goldschmidt, V. M. Die Gesetze der Krystallochemie. *Naturwissenschaften* **1926**, *14*, 477−485.

(23) Kieslich, G.; Sun, S.; Cheetham, A. K. Solid-state principles applied to organic−inorganic perovskites: new tricks for an old dog. *Chem. Sci.* **2014**, *5*, 4712−4715.

(24) Shi, E.; Gao, Y.; Finkenauer, B. P.; Akriti, A.; Coffey, A. H.; Dou, L. Two-dimensional halide perovskite nanomaterials and heterostructures. *Chem. Soc. Rev.* **2018**, *47*, 6046−6072.

(25) Dong, Y.; Zhang, Y.; Li, X.; Feng, Y.; Zhang, H.; Xu, J. Chiral Perovskites: Promising Materials toward Next-Generation Optoelec-tronics. *Small* **2019**, *15*, 1902237.

(26) Long, G.; Sabatini, R.; Saidaminov, M. I.; Lakhwani, G.; Rasmita, A.; Liu, X.; Sargent, E. H.; Gao, W. Chiral-perovskite optoelectronics. *Nat. Rev. Mater.* **2020**, DOI: 10.1038/s41578-020-0181-5.

(27) Chen, C.; Gao, L.; Gao, W.; Ge, C.; Du, X.; Li, Z.; Yang, Y.; Niu, G.; Tang, J. Circularly polarized light detection using chiral hybrid perovskite. *Nat. Commun.* **2019**, *10*, 1927.

(28) Ma, J.; Fang, C.; Chen, C.; Jin, L.; Wang, J.; Wang, S.; Tang, J.; Li, D. Chiral 2D Perovskites with a High Degree of Circularly Polarized Photoluminescence. *ACS Nano* **2019**, *13*, 3659−3665.

(29) Yang, C. K.; Chen, W. N.; Ding, Y. T.; Wang, J.; Rao, Y.; Liao, W. Q.; Tang, Y. Y.; Li, P. F.; Wang, Z. X.; Xiong, R. G. The First 2D Homochiral Lead Iodide Perovskite Ferroelectrics: [R- and S-1-(4-Chlorophenyl)ethylammonium]₂PbI₄. *Adv. Mater.* **2019**, *31*, 1808088.

(30) Long, G.; Jiang, C.; Sabatini, R.; Yang, Z.; Wei, M.; Quan, L. N.; Liang, Q.; Rasmita, A.; Askerka, M.; Walters, G.; Gong, X.; Xing, J.; Wen, X.; Quintero-Bermudez, R.; Yuan, H.; Xing, G.; Wang, X. R.; Song, D.; Voznyy, O.; Zhang, M.; Hoogland, S.; Gao, W.; Xiong, Q.; Sargent, E. H. Spin control in reduced-dimensional chiral perovskites. *Nat. Photon.* **2018**, *12*, 528−533.

(31) Babayigit, A.; Boyen, H.-G.; Conings, B. Environment versus sustainable energy: The case of lead halide perovskite-based solar cells. *MRS Energy Sustain.* **2018**, *5*, E1.

(32) Noel, N. K.; Stranks, S. D.; Abate, A.; Wehrenfennig, C.; Guarnera, S.; Haghighirad, A.-A.; Sadhanala, A.; Eperon, G. E.; Pathak, S. K.; Johnston, M. B.; Petrozza, A.; Herz, L. M.; Snaith, H. J.

(33) Yang, N.; Sun, H. Biocoordination chemistry of bismuth: Recent advances. *Coord. Chem. Rev.* **2007**, *251*, 2354−2366.

(34) Mercier, N.; Louvain, N.; Bi, W. Structural Diversity and Retro-Crystal Engineering Analysis of Iodometalate Hybrids. *CrystEngComm* **2009**, *11*, 720−734.

(35) Wu, L.-M.; Wu, X.-T.; Chen, L. Structural Overview and Structure−Property Relationships of Iodoplumbate and Iodobismu-thate. *Coord. Chem. Rev.* **2009**, *253*, 2787−2804.

(36) Adonin, S. A.; Sokolov, M. N.; Fedin, V. P. Polynuclear Halide Complexes of Bi(III): From Structural Diversity to the New Properties. *Coord. Chem. Rev.* **2016**, *312*, 1−21.

(37) Mitzi, D. B. Organic-Inorganic Perovskites Containing Trivalent Metal Halide Layers: The Templating Influence of the Organic Cation Layer. *Inorg. Chem.* **2000**, *39*, 6107−6113.

(38) Lehner, A. J.; Fabini, D. H.; Evans, H. A.; Hébert, C.-A.; Smock, S. R.; Hu, J.; Wang, H.; Zwanziger, J. W.; Chabinyc, M. L.; Seshadri, R. Crystal and Electronic Structures of Complex Bismuth Iodides A₃Bi₂I₉ (A = K, Rb, Cs) Related to Perovskite: Aiding the Rational Design of Photovoltaics. *Chem. Mater.* **2015**, *27*, 7137−7148.

(39) Chang, J.-H.; Doert, T.; Ruck, M. Structural Variety of Defect Perovskite Variants M₃E₂X₉ (M = Rb, Tl, E = Bi, Sb, X = Br, I). *Z. Anorg. Allg. Chem.* **2016**, *642*, 736−748.

(40) McCall, K. M.; Stoumpos, C. C.; Kostina, S. S.; Kanatzidis, M. G.; Wessels, B. W. Strong Electron−Phonon Coupling and Self-Trapped Excitons in the Defect Halide Perovskites A₃M₂I₉ (A = Cs, Rb; M = Bi, Sb). *Chem. Mater.* **2017**, *29*, 4129−4145.

(41) Wojciechowska, M.; Gągor, A.; Piecha-Bisiorek, A.; Jakubas, R.; Ciżman, A.; Zaręba, J. K.; Nyk, M.; Zieliński, P.; Medycki, W.; Bil, A. Ferroelectricity and Ferroelasticity in Organic Inorganic Hybrid (Pyrrolidinium)₃[Sb₂Cl₉]. *Chem. Mater.* **2018**, *30*, 4597−4608.

(42) Leng, M.; Chen, Z.; Yang, Y.; Li, Z.; Zeng, K.; Li, K.; Niu, G.; He, Y.; Zhou, Q.; Tang, J. Lead-Free, Blue Emitting Bismuth Halide Perovskite Quantum Dots. *Angew. Chem., Int. Ed.* **2016**, *55*, 15012−15016.

(43) Li, M.-Q.; Hu, Y.-Q.; Bi, L.-Y.; Zhang, H.-L.; Wang, Y.; Zheng, Y.-Z. Structure Tunable Organic−Inorganic Bismuth Halides for an Enhanced Two-Dimensional Lead-Free Light-Harvesting Material. *Chem. Mater.* **2017**, *29*, 5463−5467.

(44) Dehnhardt, N.; Luy, J.-N.; Szabo, M.; Wende, M.; Tonner, R.; Heine, J. Synthesis of a two-dimensional organic−inorganic bismuth iodide metalate through in situ formation of iminium cations. *Chem. Commun.* **2019**, *55*, 14725−14728.

(45) Boldish, S. I.; White, W. B. Optical band gaps of selected ternary sulfide minerals. *Am. Mineral.* **1998**, *83*, 865−871.

(46) Sheldrick, G. M. Short History of SHELX. *Acta Crystallogr., Sect. A: Found. Crystallogr.* **2008**, *64*, 112−122.

(47) Sheldrick, G. M. SHELXT − Integrated Space-Group and Crystal-Structure Determination. *Acta Crystallogr., Sect. A: Found. Adv.* **2015**, *71*, 3−8.

(48) Sheldrick, G. M. Crystal Structure Refinement with SHELXL. *Acta Crystallogr., Sect. C: Struct. Chem.* **2015**, *71*, 3−8.

(49) Dolomanov, O. V.; Bourhis, L. J.; Gildea, R. J.; Howard, J. A. K.; Puschmann, H. OLEX2: A Complete Structure Solution, Refinement and Analysis Program. *J. Appl. Crystallogr.* **2009**, *42*, 339−341.

(50) Brandenburg, K. *Diamond*; Crystal Impact GbR: Bonn, Germany, 2005.

(51) Särnstrand, C. The Crystal Structure of Antimony(III) Chloride Oxide Sb₄O₅Cl₂. *Acta Crystallogr., Sect. B: Struct. Crystallogr. Cryst. Chem.* **1978**, *34*, 2402−2407.

(52) Wang, K.; Wu, C.; Yang, D.; Jiang, Y.; Priya, S. Quasi-Two-Dimensional Halide Perovskite Single Crystal Photodetector. *ACS Nano* **2018**, *12*, 4919−4929.

(53) Zarychta, B.; Bujak, M.; Zaleski, J. Distortions of [Sb₂Cl₁₀]⁴⁻ Bioctahedra and Phase Transitions in the Chloroantimonate(III) (C₃H₅NH₃)₂[SbCl₅] · (C₃H₅NH₃)Cl. *Z. Naturforsch., B: Chem. Sci.* **2007**, *62*, 44−50.

Lead-Free Organic−Inorganic Tin Halide Perovskites for Photo-voltaic Applications. *Energy Environ. Sci.* **2014**, *7*, 3061−3068.

(54) Terao, H.; Ninomiya, S.; Hashimoto, M.; Eda, K. [81]Br NQR and crystal structure of 4-bromopyridinium pentabromoantimonate-(III); 3c−4e bonding and NQR trans influence. *J. Mol. Struct.* **2010**, *965*, 68−73.

(55) Bukvetskii, B. V.; Storozhuk, T. V.; Mirochnik, A. G.; Petrochenkova, N. V.; Karasev, V. E. Synthesis, Crystal Structure, and Luminescent Properties of Antimony(III) Halide Complexes with 6-Methylquinoline. *Russ. J. Inorg. Chem.* **2004**, *49*, 43−50.

(56) García-Fernández, A.; Marcos-Cives, I.; Platas-Iglesias, C.; Castro-García, S.; Vázquez-García, D.; Fernández, A.; Sánchez-Andújar, M. Diimidazolium Halobismuthates $[Dim]_2[Bi_2X_{10}]$ (X = Cl⁻, Br⁻, or I⁻): A New Class of Thermochromic and Photoluminescent Materials. *Inorg. Chem.* **2018**, *57*, 7655−7664.

(57) Mitzi, D. B. Synthesis, Crystal Structure, and Optical and Thermal Properties of $(C_4H_9NH_3)_2MI_4$ (M = Ge, Sn, Pb). *Chem. Mater.* **1996**, *8*, 791−800.

(58) Mousdis, G. A.; Papavassiliou, G. C.; Raptopoulou, C. P.; Terzis, A. Preparation and characterization of $[H_3N(CH_2)_6NH_3]PbI_4$ and similar compounds with a layered perovskite structure. *J. Mater. Chem.* **2000**, *10*, 515−518.

(59) Zarychta, B.; Zaleski, J. Phase Transitions Mechanism and Distortion of $SbCl_6^{3-}$ Octahedra in Bis(n-butylammonium) Pentachloroantimonate(III) $(C_4H_9NH_3)_2[SbCl_5]$. *Z. Naturforsch., B: Chem. Sci.* **2006**, *61*, 1101−1109.

(60) Jha, N. K.; Rizvi, S. S. A. Some studies on bromoantimonate-(III) complexes. *J. Inorg. Nucl. Chem.* **1974**, *36*, 1479−1489.

(61) Mousdis, G. A.; Papavassiliou, G. C.; Terzis, A.; Raptopoulou, C. P. Preparation, Structures and Optical Properties of $[H_3N-(CH_2)_6NH_3]BiX_5$ (X=I, Cl) and $[H_3N(CH_2)_6NH_3]SbX_5$ (X=I, Br). *Z. Naturforsch., B: Chem. Sci.* **1998**, *53*, 927−932.

(62) Steiner, T. Hydrogen-Bond Distances to Halide Ions in Organic and Organometallic Crystal Structures: Up-to-date Database Study. *Acta Crystallogr., Sect. B: Struct. Sci.* **1998**, *54*, 456−463.

(63) Alvarez, S. A cartography of the van der Waals territories. *Dalton Trans.* **2013**, *42*, 8617−8636.

(64) Anyfantis, G. C.; Ganotopoulos, N.-M.; Savvidou, A.; Raptopoulou, C. P.; Psycharis, V.; Mousdis, G. A. Synthesis and characterization of new organic−inorganic hybrid compounds based on Sb, with a perovskite like structure. *Polyhedron* **2018**, *151*, 299−305.

(65) Moon, T. H.; Oh, S.-J.; Ok, K. M. $[((R)-C_8H_{12}N)_4][Bi_2Br_{10}]$ and $[((S)-C_8H_{12}N)_4][Bi_2Br_{10}]$: Chiral Hybrid Bismuth Bromides Templated by Chiral Organic Cations. *ACS Omega* **2018**, *3*, 17895−17903.

(66) Billing, D. G.; Lemmerer, A. Synthesis and crystal structures of inorganic−organic hybrids incorporating an aromatic amine with a chiral functional group. *CrystEngComm* **2006**, *8*, 686−695.

(67) Mercier, N.; Barres, A.-L.; Giffard, M.; Rau, I.; Kajzar, F.; Sahraoui, B. Conglomerate- to- true- racemate reversible solid- state transition in crystals of an organic disulfide- based iodoplumbate. *Angew. Chem., Int. Ed.* **2006**, *45*, 2100−2103.

(68) Bi, W.; Mercier, N. Reversible dynamic isomerism change in the solid state, from Bi_4I_{16} clusters to BiI_4 1D chains in L-cystine based hybrids: templating effect of cations in iodobismuthate network formation. *Chem. Commun.* **2008**, 5743−5745.

(69) Peng, Y.; Yao, Y.; Li, L.; Wu, Z.; Wang, S.; Luo, J. White-light emission in a chiral one-dimensional organic−inorganic hybrid perovskite. *J. Mater. Chem. C* **2018**, *6*, 6033−6037.

(70) Zhu, L.-L.; Huang, Y.-E.; Lin, Y.-P.; Huang, X.-Y.; Liu, H.-Q.; Mitzi, D. B.; Du, K.-Z. Stereochemically active lead chloride enantiomers mediated by homochiral organic cation. *Polyhedron* **2019**, *158*, 445−448.

(71) Salah, M. B. H.; Mercier, N.; Allain, M.; Zouari, N.; Botta, C. Dual phosphorescence from the organic andinorganic moieties of 1D hybrid perovskites of the $Pb_{n'}Br_{4n'+2}$ series (n'=2,3,4,5). *J. Mater. Chem. C* **2019**, *7*, 4424−4433.

(72) Wang, L.; Xue, Y.; Cui, M.; Huang, Y.; Xu, H.; Qin, C.; Yang, J.; Dai, H.; Yuan, M. A Chiral Reduced-Dimension Perovskite for an Efficient Flexible Circularly Polarized Light Photodetector. *Angew. Chem., Int. Ed.* **2020**, *59*, 6442−6450.

(73) Mady, K. A.; Eid, A. H.; Soliman, W. Z. Optical Properties and Interband Transitions in the Layered Compounds SbI3. *Czech J. Phys.* **1979**, *29*, 907−912.

(74) Podraza, N. J.; Qiu, W.; Hinojosa, B. B.; Motyka, M. A.; Phillpot, S. R.; Baciak, J. E.; Trolier-McKinstry, S.; Nino, J. C.; Nino, J. C. Band gap and structure of single crystal BiI3: Resolving discrepancies in literature. *J. Appl. Phys.* **2013**, *114*, 033110.

(75) Oswald, I. W. H.; Mozur, E. M.; Moseley, I. P.; Ahn, H.; Neilson, J. R. Hybrid Charge-Transfer Semiconductors: $(C_7H_7)SbI_4$, $(C_7H_7)BiI_4$, and Their Halide Congeners. *Inorg. Chem.* **2019**, *58*, 5818−5826.

(76) Abulikemu, M.; Ould-Chikh, S.; Miao, X.; Alarousu, E.; Murali, B.; Ngongang Ndjawa, G. O.; Barbé, J.; El Labban, A.; Amassian, A.; Del Gobbo, S. Optoelectronic and photovoltaic properties of the air-stable organohalide semiconductor $(CH_3NH_3)_3Bi_2I_9$. *J. Mater. Chem. A* **2016**, *4*, 12504−12515.

(77) Dunlap-Shohl, W. A.; Zhou, Y.; Padture, N. P.; Mitzi, D. B. Synthetic Approaches for Halide Perovskite Thin Films. *Chem. Rev.* **2019**, *119*, 3193−3295.

(78) Shen, Y. R. *The Principles of Nonlinear Optics*; Wiley & Sons: New Jersey, 2003.